STUDY OF RADIO-FREQUENCY PLASMA DEPOSITION OF AMORPHOUS SILICON FOR THE IMPROVEMENT OF SOLAR CELL PRODUCTION

THÈSE N^O 2900 (2003)

PRÉSENTÉE À LA FACULTÉ SCIENCES DE BASE

CRPP Association Euratom

SECTION DE PHYSIQUE

ÉCOLE POLYTECHNIQUE FÉDÉRALE DE LAUSANNE

POUR L'OBTENTION DU GRADE DE DOCTEUR ÈS SCIENCES

PAR

Juliette BALLUTAUD

DEA d'électronique, Université Paris VI, France
et de nationalité française

acceptée sur proposition du jury:

Dr A. Howling, directeur de thèse
M. A. Buechel, rapporteur
Dr J. Perrin, rapporteur
Prof. A. Shah, rapporteur

Lausanne, EPFL
2004

Abstract

Plasma enhanced chemical vapour deposition (PECVD) of thin films such as amorphous silicon has widespread applications especially in the field of photovoltaic solar cells and thin-film transistors for flat screen production. Industrial applications require high depositions rates over large areas with a good uniformity in layer thickness. In this thesis, some aspects of PECVD in large surface, industrial type, capacitive radio frequency reactor are investigated. The aim of this work is to study the plasma process conditions to increase the deposition rate of uniform, good quality, a-Si:H layer for solar cell application in a single chamber reactor.

The studies realized during this thesis have necessitated the development and the comprehension of diagnostics such as deposition rate measurement by in-situ interferometry, plasma power measurement and layer density measurement by ellipsometry. During the thesis, we have also elaborated a matching-box circuit for using process frequencies of 27.12 MHz and 40.68 MHz.

Deposition of a-Si:H in small electrode gap reactor has been studied. At present industrial reactors have a standard electrode gap of 2.4 cm. We modified a reactor to reach a small gap of 1.7 cm. It appears that we have obtained faster deposition rate in the small gap reactor but non-uniformity problems increase due to edge focusing and powder effects. One solution, based on a teflon jigsaw to keep the plasma away from the edge confined spaces, is proposed to suppress focusing effect but the operation parameter space is still reduced by the powder effect.

Systematic measurements of a-Si:H layer density was also done by ellipsometry. It is shown that the layer density decreases when the deposition rate increases, independently of pressure, gas flow and frequency (27.12 MHz/40.68 MHz) of the plasma. At high deposition rate, 6 Å/s, only an increase of the process temperature from 200°C to 230°C can significantly improve the layer density. We have noted also a slight improvement of layer density for layers deposited in the small gap reactor. Nevertheless industrial constraints impose a process temperature of 200°C and a standard gap reactor. By optimising the process parameters, keeping the temperature process at 200°C, good quality, uniform, a-Si:H layer were deposited at 3 Å/s on 37 cm × 47 cm glass substrates at 40.68 MHz.

A particular source of non-uniformity in large area reactor has been examined. In large area reactors, a perturbation in RF plasma potential, due to the electrode edge asymmetry, propagates towards the plasma center with a characteristic damping length λ. The variation of RF plasma potential at the edge implies a variation of the deposition rate across the reactor area and then a non-uniformity of the deposited layer. A theoretical study was done to understand of this phenomenon and experimental results confirmed the model.

Finally, for solar cell applications, a study of the boron cross-contamination during solar cell deposition in a single chamber process has been done. During the deposition of the intrinsic layer, for a p-i-n cell, i-layer is contaminated by the residual boron radicals present in the reactor after the deposition of the boron-doped layer. This contamination decreases cell performance. Several reactor treatments have been tested to solve this contamination problem. The effectiveness of these treatments was evaluated by secondary ion mass microscopy (SIMS) measurements. It appears that an ammonia flush or a water vapour flush of a few minutes, between the deposition of the p-layer and i-layer, reduces the boron contamination at the p-i interface. The performance of cells made with these treatments, in a single chamber process, are comparable to performance of cells done in a multi-chamber process.

Version abrégée

Le dépôt assisté par plasma (PECVD) de films minces comme le silicium amorphe est utilisée pour de nombreuses applications, en particulier dans le domaine des cellules solaires photovoltaïques et des transistors en couches minces pour les écrans plats. Les procédés industriels nécessitent des vitesses de dépôt élevées sur de grandes surfaces, avec une bonne uniformité de l'épaisseur des couches. Dans le cadre de cette thèse, certains aspects du dépôt assisté par plasma ont été étudiés dans un réacteur industriel radiofréquence de grande surface.

Les études réalisées durant cette thèse ont nécessité la mise au point et la compréhension de diagnostics comme la mesure in-situ de la vitesse de dépôt, la mesure de la puissance du plasma et la mesure de la densité des couches par ellipsométrie. Nous avons également construit une boîte d'accord radio-fréquence afin de pouvoir travailler à 27.12 MHz et 40.68 MHz.

Le dépôt de silicium amorphe dans un réacteur de petite distance inter-électrode a été étudié. Actuellement, les réacteurs industriels possèdent une distance inter-électrode de 2.4 cm. Nous avons modifié notre reacteur pour atteindre une distance de 1.7 cm. Des vitesses de dépôt plus rapides ont été obtenues dans ce réacteur modifié ; mais les problèmes de non-uniformité sont plus importants à cause des effets de concentration du plasma au bord du réacteur, et de la formation de poudre. Nous proposons une solution, utilisant un puzzle de téflon, afin de tenir le plasma éloigné des espaces confinés au bord du réacteur. Néanmoins, l'espace des paramètres opérationnels est limité par la formation de poudre et de ses effets sur l'uniformité des couches.

Une mesure sytématique de la densité des couches de silicium amorphe a été faite par ellipsométrie. Il apparaît que la densité des couches diminue lorsque la vitesse de dépôt augmente, indépendamment de la pression, du flux des gaz, et de la fréquence (27.12 MHz/40.68 MHz) du plasma. Pour une grande vitesse de dépôt, 6 Å/s, seule une augmentation de la temperature du procédé de 200°C à 230°C améliore de façon significative la densité des couches. Nous avons aussi noté une petite amélioration de la densité des couches déposées dans le réacteur de petite distance inter-électrode. Cependant, des contraintes industrielles imposent une température de procédé à 200°C et un reacteur de distance inter-électrode standard. En optimisant les paramètres de procédé, en gardant une température à 200°C et une fréquence de 40.68MHz, nous avons déposé une couche uniforme de silicium amorphe de bonne qualité sur un substrat de verre 37 cm × 47 cm à 3 Å/s.

Une source particulière de non-uniformité dans un réacteur de grande surface a été étudiée. Dans un réacteur de grande surface, une perturbation dans le potentiel plasma RF, due à une assymétrie au bord du réacteur, se propage vers le centre du plasma avec une longueur d'atténuation caractéristique λ. La variation du potentiel plasma RF implique

une variation de la vitesse de dépôt à travers la surface du réacteur et donc une mauvaise uniformité de la couche déposée. Une étude théorique a été menée pour comprendre ce phénomène et les résultats expérimentaux confirment le modèle.

Finalement, en vue d'une application dans le domaine des cellules solaires, nous avons étudié la contamination du réacteur par le bore au cours du dépôt de cellules solaires dans un réacteur unique. Durant le dépôt de la couche intrinsèque, pour une cellule de type p-i-n, la couche i est contaminée par les radicaux de bore résiduels, présents dans le réacteur après le dépôt de la couche p dopée bore. Cette contamination altère les performances de la cellule. Plusieurs traitements du réacteur ont été testés afin de résoudre ce probléme. L'efficacité de ces traitements a été évaluée avec un analyseur ionique (SIMS). Il apparaît qu' un flux d'ammoniac ou de vapeur d'eau, effectué entre le dépôt de la couche p et de la couche i, réduit la contamination bore à l'interface p-i. Les performances des cellules déposées dans un réacteur unique, et qui ont subi un de ces deux traitements, ont des performances comparables à celles des cellules déposées au cours d'un procédé utilisant plusieurs réacteur.

Contents

Chapter 1

Introduction

1.1 Industrial applications of plasmas

Plasma is referred to as the fourth state of matter, the three other ones being the solid state, the liquid state and the gas state. Plasma is a quasi-neutral gas containing charged particles (electrons and ions) governed by electromagnetic forces. Most of the universe, stars and stellar clouds, is made up of plasma. On earth, flame, aurora and neon signs are typical examples of plasmas.

The plasma medium is described by its temperature and its electronic density. These two parameters determine in a large part the plasma properties. We can see on figure 1.1 the large variety of plasma, from aurora with a low temperature and density, to fusion plasma with a temperature of 10^4 eV and a density of 10^{17} cm^{-3} [1,2]. The plasma studied in this thesis is a low pressure plasma, a glow discharge plasma, with a temperature of few eV and a electronic density around 10^9 cm^{-3}.

Nowadays, plasmas are commonly used in a large variety of industrial processes : materials cutting, layer coating, etching, surface treatments (cf. figure 1.2). Plasma processing of materials affects several of the largest manufacturing industries like defense, automobiles, biomedicine, telecommunications. At present the most important plasma application is the production of large-scale microelectronic circuits [3]. With plasma processing, materials and surface structures of chips can be fabricated that are not feasible with other processes. For example, electronic component size scale is less than 0.5 μm and this resolution can't be reached by etching techniques with liquid acid. Plasma etching process must be used.

With the development of the plasma process in industry, it has become important to study plasma phenomena in detail, which is not always possible in the industrial environment. Nowadays, many laboratories work on the subject of plasma physics, doing experiments or computer models.

1.2 Radio-frequency plasmas

Electrical discharges are commonly used to produce a plasma from a gas. These plasmas can be divided in two categories : equilibrium and non-equilibrium plasmas. The glow discharge plasma is a non-equilibrium plasma in which the electrons are hotter than the ions. They can be produced by an electric field (DC or alternating) which delivers energy to the gas to ignite the plasma and maintain it.
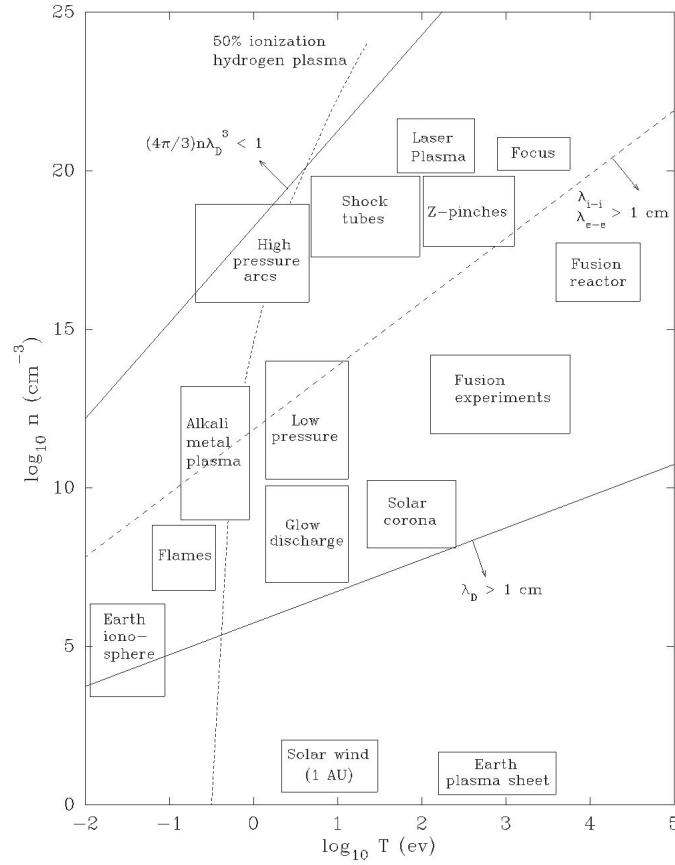
Figure 1.1: *Plasmas classification in function of their temperature and their electronic density [1].*

One of the most used configurations is the radio-frequency (RF) discharge between two plane electrodes. In this configuration, the plasma is capacitively coupled and the power supply interacts with the plasma almost exclusively by displacement current [3]. The advantage is that we can use the plasma even with electrodes covered by an insulating material.

The frequency range is from a few kHz to 200 MHz but the usual frequency used for RF discharge plasma is 13.56 MHz. This frequency was initially chosen by the international telecommunications authorities as a free frequency which was not used by civilians or the military. This is now a standard frequency for which we can easily find commercial generators and matching box. More and more industry is interested by higher process frequencies like 27.13 MHz, 40.68 MHz (2nd and 3rd harmonics of 13.56 MHz). At these higher frequencies, the layer quality seems better (cf. chapter 6).

As mentioned above, the RF plasma is a non-equilibrium plasma with hot electrons (T_e around a few eV) but the other plasma species, ions and neutral species, are at the gas temperature. At megahertz frequencies only electrons follow the electric field oscillations,
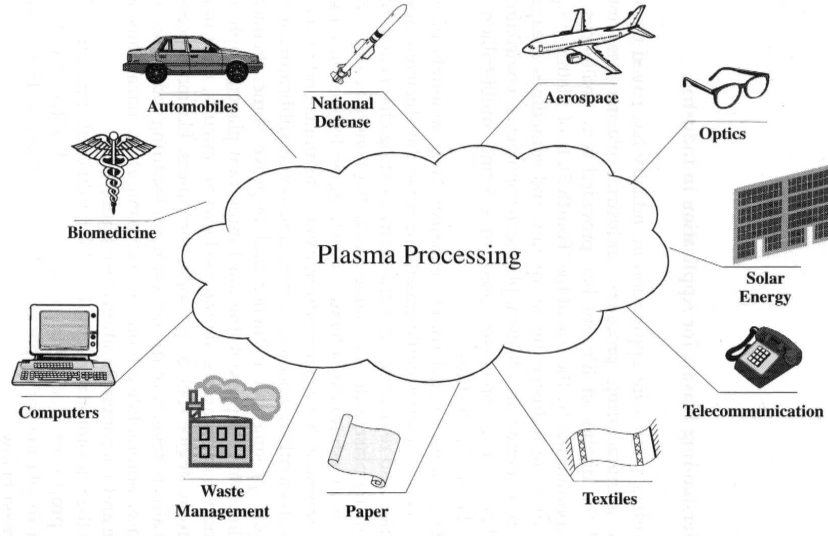
Figure 1.2: *Plasma processing in industry [3].*
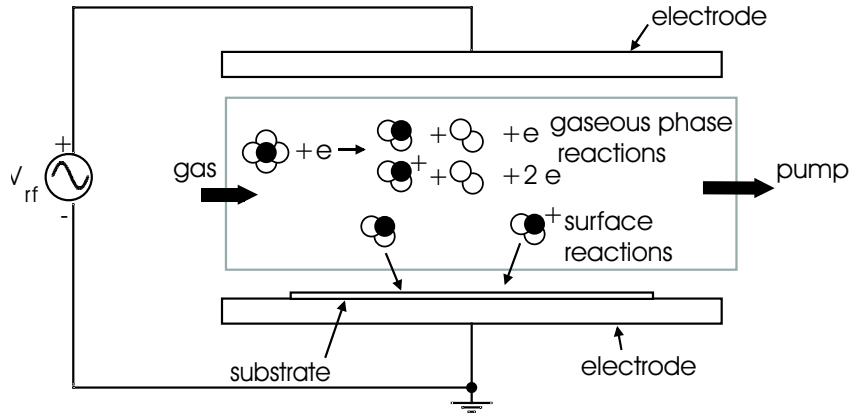
Figure 1.3: *Radio-frequency, capacitively coupled plasma reactor, principle.*

the electronic and ionic plasma frequencies are :

$$\omega_{\mathrm{pi,e}} = (e^2 n_{\mathrm{i,e}}/\varepsilon_0 m_{\mathrm{i,e}})^2 \tag{1.1}$$

$$\omega_{\mathrm{pi}} < \omega = 2\pi f < \omega_{\mathrm{pe}} \quad \text{where } f \text{ is the RF plasma frequency.}$$

As we can see in figure 1.3, a non-reactive gas is introduced into the discharge, in the inter-electrode space. Atoms or molecules are dissociated and (or) ionized by the electronic collisions to form ions or radicals. These ions and radicals can stay in the plasma and react with other species. Or they can diffuse to the reactor walls and to the substrate. The radicals and the ions react with the substrate (and walls) surface and modify it. Volatile components can be created that will leave the surface. The result is an etching of the surfaces exposed to the plasma. Non volatile components will stay on the surfaces and lead to a layer growth on the surfaces exposed to the plasma (deposition).

Many external parameters, that can be controlled, are involved in the plasma process: pressure, gas flow, gas recipe, reactor design, reactor temperature, power, frequency, etc. Layer deposition processes are characterized by the layer properties, the deposition rate, its uniformity, etc. The difficulty is to link these external plasma parameters with the layer properties. Empirical studies were commonly done but the comprehension of the

interactions between plasma parameters and layer properties is important for a better process optimization.

1.3   Amorphous silicon

In 1975, W.E. Spear and P.G. LeComber achieved the initial success of p-n doping control in hydrogenated amorphous silicon (a-Si:H) using the glow discharge technique. The following year, the RCA group (D. E. Carlson and C. R. Wronski) announced the first a-Si:H solar cells [4]. Since then, a-Si:H has a large variety of applications in electronic devices, for example, thin film transistors, flat panel displays, thin film solar cells [5]. Compared to mono-crystalline silicon, a-Si:H properties, as a semi-conductor, are less good but the interest in a-Si:H is it can be deposited on large surfaces at a lower price and at a lower energy cost.

Hydrogenated amorphous silicon has been prepared by a variety of deposition techniques such as plasma CVD (chemical vapor deposition), reactive sputtering, homogeneous CVD and photo-induced CVD. The Plasma Enhanced Chemical Vapor Deposition method (PECVD), including deposition by RF plasmas, is one of the most used methods, since it is technologically mature and adapted to mass production. Amorphous silicon is generally obtained with silane gas (SiH_4) which is dissociated in the plasma into active radicals (SiH_x with x = 0, 1, 2 or 3). The hydrogen is very important because its incorporation into amorphous silicon reduces the number of electronically active defects states in the pseudo energy gap and enables p- or n- type doping. Generally, a-Si:H layer is composed of 5 to 15% of hydrogen.

The properties of the a-Si:H layer, deposition rate, density, electronic mobility, depend strongly on the plasma parameters (gases recipe, pressure, power, electrode spacing, etc). For photovoltaic applications, the a-Si:H layer should have a small defect density, a good absorption of the solar spectrum, a high material density and good uniformity. The optimization of a-Si:H layer properties and process needs a good comprehension of the plasma and deposition phenomena.

1.4   Purpose and organization of the work

1.4.1   Industrial issues

This thesis work was done within the scope of the Swiss Commission for Technology and Innovation (CTI) under Research Grants #4559.1 and 5994.2. The goal of this co-operation between CRPP, the Institute of Microtechnology of Neuchâtel (IMT) and Unaxis Displays is the development of a new PECVD production system for thin film silicon solar cells. The main scientific and technical issues for the project were the development and optimization of a large area and high throughput plasma assisted coating system for the production of silicon thin films and solar cells. It has be noted that at present in production lines deposition rates of around only 1-2 Å/s are obtained, resulting in deposition times of at least one hour for 0.4 μm thick a-Si:H solar cell. Therefore an increase in deposition rate on the industrial scale is highly desirable, but it has not been reached before.

The task of CRPP was to optimize the plasma process on the KAI-S reactor. This included investigations of the effect of the electrode gap distance on the deposition and

of the influence of higher excitation frequency of 27.12/40.68 MHz instead of the usual 13.56 MHz. The aim of these investigations was to optimize the process and to increase the deposition rate up to a maximum value while respecting layer uniformity and quality as demanded for solar cell production in a large area reactor. CRPP's work was also to control the critical issue of the boron cross-contamination in a single chamber process for solar cell deposition. Cost reduction would be possible if single chamber can be used in place of multichamber. This is the key point for the success of this KAI reactor in solar cells applications.

IMT was asked to optimize solar cell deposited in a KAI-S reactor, starting with the a-Si:H CRPP optimized recipe. Solar cell performance had to reach the following industrial specifications: after degradation during 1000 hours at 50°C at least 850 mV of V_{oc} and 60% fill factor (FF).

1.4.2 Organization of the thesis work

The research work presents several objectives concerning plasma assisted deposition in a large area reactor. The first main objective was to study the influence of plasma parameters and reactor design on layer deposition rate and properties, particularly layer density. A large part of the work was done regarding the small gap reactor and plasma non-uniformity due to reactor design. An important work of comprehension was also done about a-Si:H layer optical characterization. The second main objective was to suppress the boron cross-contamination during the deposition of the intrinsic layer after the deposition of the boron doped p -layer. During the research work, the increase of the excitation frequency leads us to study matching circuit theory and manufacturing.

This report is organized in eight chapters. Chapter 2 is a detailed description of the reactor and diagnostics used. Chapter 3 presents the studies about the RF matching circuit for 27.12 MHz. Chapter 4 presents in detail the optical layer diagnostics (ellipsometry and interferometry). This chapter is particular because it is not directly linked to the plasma field but an important comprehension work was necessary to be certain of the scientific validity of the measurements. The chapter 5 presents the results concerning a-Si:H deposition in a small gap reactor. Chapter 6 presents the results of the study about the influence of the deposition rate on a-Si:H layer density. Chapter 7 presents the study about the plasma non-uniformity in a large area reactor. This not only concerns a-Si:H deposition but is a crucial issue for all plasma assisted processes in large area reactors. Chapter 8 presents the optimization of the treatment to prevent boron cross contamination. Finally chapter 9 groups the general conclusions of the thesis work.

Chapter 2

Reactor and diagnostics

2.1 The reactor

In the laboratory, we use a modified version of the industrial reactor type KAI-S. The KAI-S reactor was developed by Unaxis Displays for the plasma assisted deposition of thin layers on large areas. Section 2.1.1 will present the main concepts of the KAI-S reactor and section 2.1.2 will present the laboratory version of the KAI-S reactor.

2.1.1 The reactor, industrial version

The KAI reactor was developed for thin film transistor manufacturing used by flat liquid crystal displays. It allows deposition of amorphous silicon layers, doped or intrinsic, silicon nitride layers and silicon oxide layers. In new generations of KAI reactors, larger than 1 m^2 glass substrates are used. In the KAI-S reactor, the substrate size is $37\,\mathrm{cm} \times 47\,\mathrm{cm}$.

The KAI reactor concept is based on the Plasma Box$^{\mathrm{TM}}$ principle. In a conventional
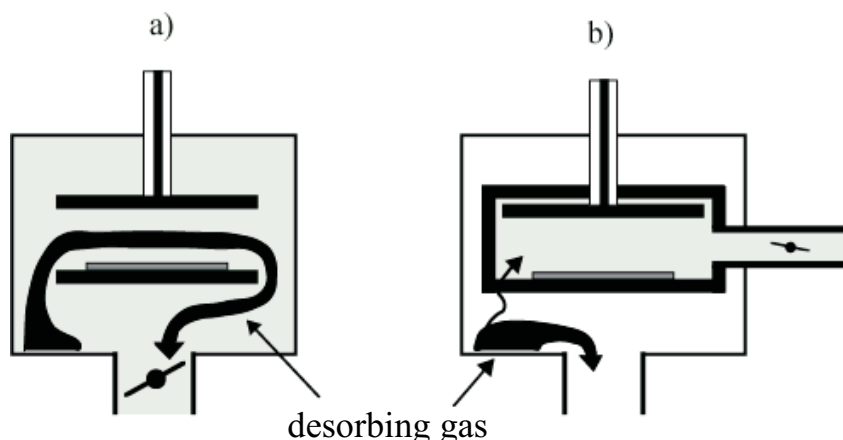
Figure 2.1: *Comparison of the impurity flow dynamic in a conventional reactor (a) and in a Plasma Box^{TM} (b). The arrows represent impurities flow.*

reactor, electrodes are just put inside a vacuum chamber (cf. figure 2.1 (a)), and the layer can be contaminated by the impurities from the walls. In the Plasma Box$^{\mathrm{TM}}$ principle, process gases are introduced in a leaktight box put inside a vacuum chamber. A differential

pumping system prevents any cross-contamination from the outgassing walls of the main chamber (cf. figure 2.1(b)) [6, 7].

This reactor is made of a special aluminium alloy and is chemically resistant to fluorine. The etch-cleaning process in the hot Plasma Box^{TM} after deposition, using a gas mixture of SF_6, O_2 and He, assures maintenance-free self-cleaning. A loadlock, an annex chamber, allows to load the substrate without breaking the vacuum or decreasing the reactor temperature.

The deposited layer quality depends on the substrate temperature. The Plasma Box^{TM} can be uniformly heated up to 330° C. High process temperature improves layer quality (cf. chapter 6). Moreover, a uniform heating avoids thermophoresis effects which could perturb the plasma uniformity [8].

To increase the productivity, 10 to 20 reactors are vertically stacked in a vacuum chamber, sharing one process system (vacuum pumps, cooling system, process gas installation). This is a gain of equipment, space and time.

2.1.2   The reactor, laboratory version

Figure 2.2(a) represents the front view of the reactor and figure 2.2(b) the top view of the reactor and vacuum chamber. The reactor is an aluminium box of interior size 66.4 cm × 47 cm × 3.7 cm. The RF electrode (56.2 cm × 46.2 cm × 0.4 cm) is suspended 2.4 cm above the ground electrode in the standard reactor. A second version of the reactor with a variable gap between the RF electrode and the ground electrode from 1.7 cm to 3 cm was used. At the end of the doctoral work, this second version of the reactor was modified to install arrays of Langmuir probes in the ground electrode (cf. chapter 7).

The space between the RF electrode and the top of the reactor is 6 mm. To avoid parasitic plasma ignition in this space, a floating aluminium plate is positioned in the middle space between the RF electrode and the top of the reactor. This floating plate acts as a capacitive divider. Process gases are uniformly introduced in the reactor through the RF electrode which acts as a shower. They are pumped from the reactor through a grid placed 57 cm back from the reactor door. This grid confines the plasma which has an area of 57 cm × 47 cm ; the inter-electrode gap depends on the version of the reactor we used. A manual loading and glass lift (pins lift) system, thanks to the loadlock, allows us to be as close as possible to industrial conditions.

Electrical supply

Our laboratory version has an RF connection and ground connection at the top of the RF electrode in the center. With RF and ground connections in the center of the RF electrode, the plasma uniformity is improved [2].

We work at different frequencies : 13.56 MHz, 27.12 MHz and 40.68 MHz (2nd and 3rd harmonics of 13.56 MHz). For 13.56 MHz we used a Dressler (type MPG1307) generator or RFFP (RF series) generator which has a pulsing mode. This 13.56 MHz generator is connected to a commercial matching box (Dressler, type variomatch 1310). For the frequencies 27.12 MHz and 40.68 MHz, we use a Dressler (WLPG 1005 400VAC Wideband 5-100 MHz) generator connected to a homemade matching box (cf. chapter 3). Passband filters at 13.56 MHz, 27.12 MHz and 40.68 MHz were used at the generator output to avoid false measurements of forward and reflected power due to strong harmonics at the generator output. Input power and reflected power between generator and matching box is measured by a wattmeter (Bird model 43). Moreover, a voltage/current/phase probe

(E.N.I), installed in the homemade matching box, allows us to measured forward power, reflected power, voltage, current and phase between the matching box and the reactor.
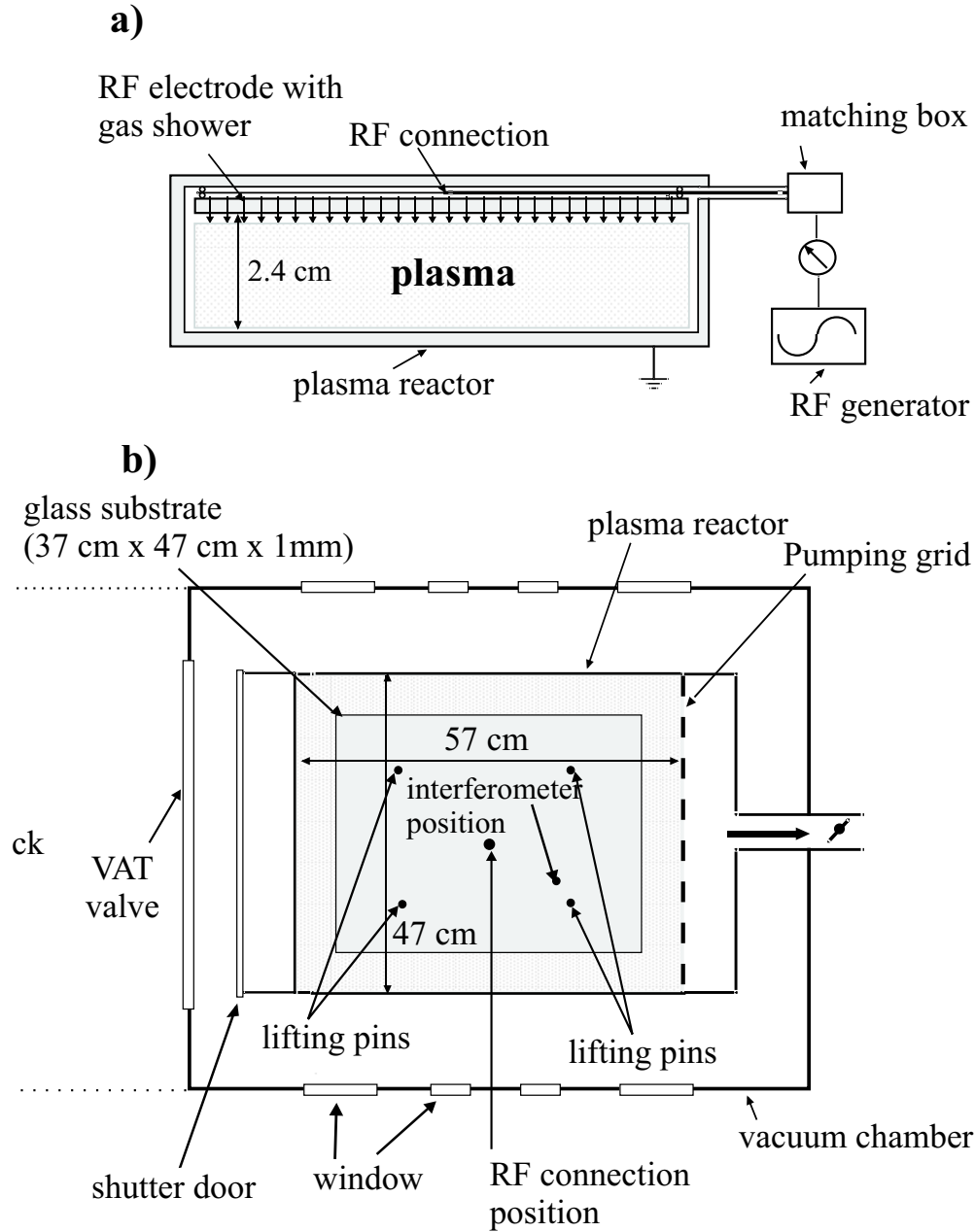
Figure 2.2: *(a) Front view of the reactor, (b) top view of the reactor and the vacuum chamber.*

Gas distribution and pumping system

Figure 2.3 represents the diagram of the gas distribution and the pumping system. Two pumping groups, which can be isolated by pneumatic valves, generate the chamber 1) vacuum and the reactor 2) vacuum. In standby mode, chamber and reactor are pumped by the dry pump 3). In process mode, the reactor is isolated from the chamber and is pumped by the second group 5) composed of a Roots pump and a primary dry pump. The throttle valve 7) allows us to control the pressure in the reactor. The throttle valve

is driven by a feed back system connected to a Baratron 8) (capacitive pressure gauge) placed in the reactor pumping line.
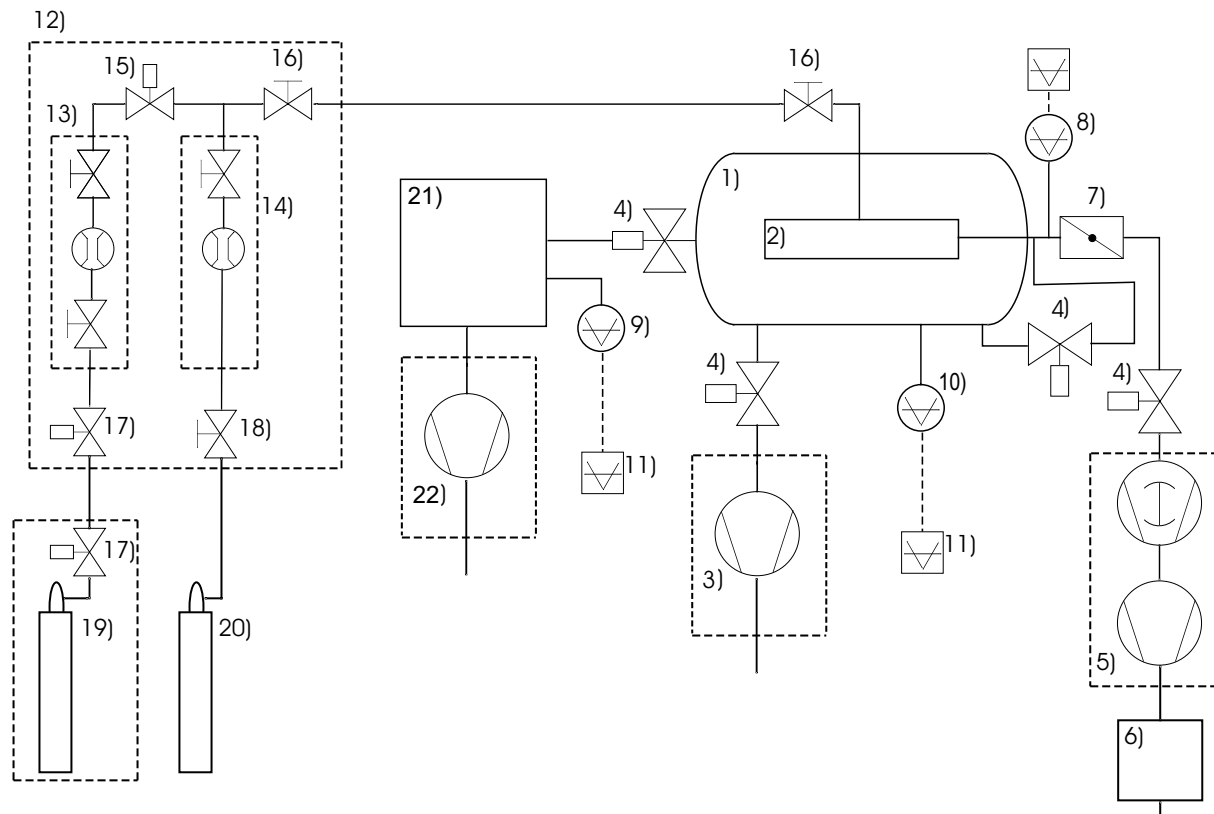
Figure 2.3: *Diagram of the pumping system and the gas distribution : 1) vacuum chamber, 2) reactor, 3) chamber pumping group (dry pump Edwards $48\,m^3/h$), 4) pneumatic control gate valve, 5) reactor pumping group (Roots pump $500\,m^3/h$ and primary dry pump Edwards $48\,m^3/h$), 6) toxic gas reactive column, 7) throttle valve, 8) Baratron gauge, 9) Pyrani gauge, 10) cold cathode gauge, 11) gauge control box, 12) gas distribution cabinet, 13) toxic gas distribution (composed of two manual valves and one flowmeter), 14) non toxic valve distribution, 15) and 17) pneumatic valves, 16) and 18) manual valves, 19) toxic gas bottles cabinet, 20) non toxic gas bottle, 21) loadlock, 22) rotary pump $16\,m^3/h$.*

This installation allows us to keep a pressure difference between the reactor and the chamber, according to the Plasma Box$^{\text{TM}}$ principle. The exit of the reactor pumping group 5) is connected to a gas reactive column 6) (GRC) which neutralizes used toxic gas. A Pyrani gauge 9) measures the pressure in the loadlock 21) and a cold cathode gauge measures the pressure in the vacuum chamber 1). The loadlock can be pumped down by a rotary pump and a security system assures that the pneumatic gate valve, between loadlock and reactor, cannot be opened when the loadlock is at atmospheric pressure.

The gas distribution cabinet 12) is placed 5 m from the reactor and includes the flowmeters. Manual valves 16), at the cabinet exit and at the reactor entrance, allow us to isolate the gas line. For non-toxic gas, bottles 20) are placed in the laboratory near the gas cabinet. Bottles are connected to experiments through the flowmeters 14) and the manual valves. Toxic gas bottles 19) are installed in an external room. They are placed in cabinets which include a purge system for bottle handling. Toxic gas bottles are connected to experiments through flowmeters and manual valves 13) and the part of the line used for toxic gas is isolated from the rest of the line with a pneumatic valve 15). Opening

of valve 15) is controlled by the security system.

Non toxic gases are Argon (500 sccm maximum), Helium (500sccm), Oxygen (100sccm) and SF_6 (300sccm). Toxic or hazardous gases used are Hydrogen (500sccm), Silane (180 sccm), Ammonia (73 sccm), and Trimethylboron diluted to 10% in hydrogen (TMB 100 sccm).

Calibration of baratron, reactor volumes and flowmeters

A regular calibration of the flowmeters is important to ensure the reproducibility of the process. We use a system of two volumes, V_1 and V_2, separated by a manual valve (cf. figure 2.4) to calibrate the baratron and to calculate the total volume of the chamber 1). The knowledge of the chamber volume allows us to calibrate the flowmeters.
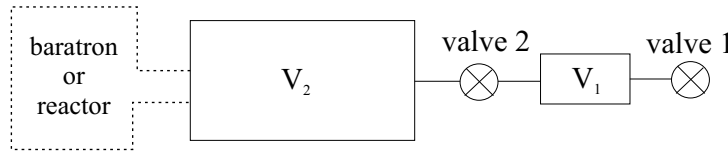

Figure 2.4: *Volume calibration* : $V_1 = 13.7\,cm^3$ *and* $V_2 = 1354\,cm^3$.

For the baratron calibration, the baratron is connected to V_2 as can be seen in figure 2.4 and the total volume V_1 plus V_2 is pumped down. Once the baratron is correctly zeroed, we open then close valve 1 to fill V_1 with atmosphere (valve V_2 closed) and then we open the valve 2. The baratron pressure is P_B. According to the Boyle's law :

$$P_{atm}.V_1 = P'_B.(V_1 + V_2) \tag{2.1}$$

Since $P_{atm} = 1\,bar$, we expect P'_B to be 10^{-2} mbar. We compare P_B and P'_B to calibrate the baratron.

To calculate the chamber volume, we connected the calibration volume and the calibrated baratron to the chamber. We fill the entire volume V_1 plus V_2 with atmosphere and exhaust it into the chamber (all gas line valves and pumping valves are closed). According the measured pressure, 4.8 mbar, and the equation 2.1, we estimate the chamber volume to about 287 l.

Once we know the chamber volume, we can calibrate the flowmeters. The chamber must be at room temperature. We set up a constant flow $F_{nominal}$, usually the maximum flow. We note the initial pressure P_{ini} in the chamber due to the flow with pumping on, using the calibrated baratron (valve 4) open between reactor and chamber). Then, we close the throttle valve 7) (pumping off) (cf. figure 2.3) and measure the time to reach a final higher pressure P_{final}. The measured flow is :

$$F_{measured}[sccm] = \frac{\Delta P[mbar]}{\Delta t[min]}.V_{reactor}[l] \tag{2.2}$$

We compare $F_{nominal}$ and $F_{measured}$ for the calibration check.

Experiment security

There are several experiments in the laboratory using toxic gases, which implies a global security for the whole laboratory and a local security for each experiment.

At the experiment level, the security system verifies the GRC operation 6) and that the
pumping system used is the reactor pumping system 5) (cf. figure 2.3). It also checks
that the pressure in the reactor is low enough and that the gas detector doesn't detect
any toxic gas. If all securities are confirmed, the opening of the toxic valve 15) is allowed.
The toxic gas line is connected to the experiment line and a signal goes to the global
security system to allow the toxic gas liberation.

At the global, laboratory, level the security system controls the gas detectors in the
laboratory gas distribution cabinet and in the toxic gas room. It checks also cabinet
ventilation, fire alarms and signals from all experiments.

If any one security, at the local level or global level, is violated, the toxic gas distribution
is closed for all experiments in the laboratory.

2.2   Diagnostics

2.2.1   Measurement of the inter-electrode voltage and of the plasma power

The voltage at the RF electrode Vpl is a very important parameter for the plasma
characterization. For given process parameters (pressure, power, frequency, gas mixing),
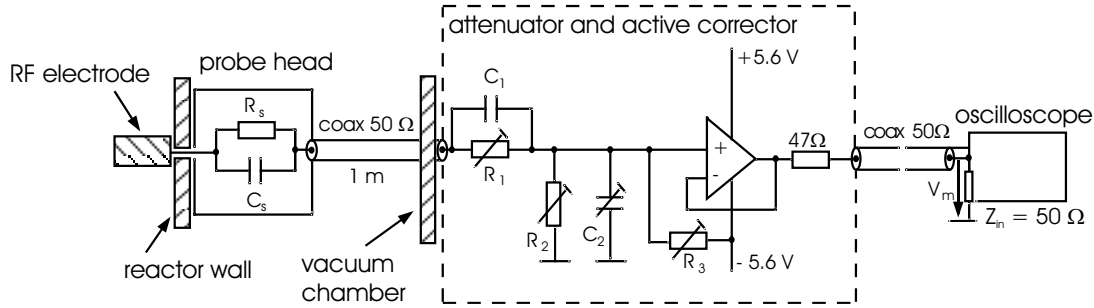plasma voltage measurement allows us to check process reproducibility.

Figure 2.5: *Diagram of the voltage probe.* $R_s = 1\ M\Omega$, $C_s = 1pF$, $R_1 = 100\Omega$, $C_1 = 8.2\ pF$,
$R_2 = 6\ k\Omega$, $C_2 = 300\ pF$ *and* $R_3 = 1M\Omega$.

For a capacitively coupled plasma, the inter-electrode voltage has an oscillating compo-
nent V_{pp} (peak to peak voltage) and a DC component V_{DC} (self-bias voltage due to the
difference between the RF and ground areas [9] [10]). In our case, the probe must have a
large bandwidth from DC to 100 MHz. Commercial passive probes exist but they are not
adapted to high temperatures, vacuum environment and corrosive gas. Moreover, they
would not be suited to the Plasma Box^{TM} geometry. So a voltage probe, suitable for our
experiment, was built [2].

In figure 2.5, the diagram of the voltage probe is shown. It is a high impedance probe
and a voltage divider (1/500). The probe head is connected to the RF electrode and to
the ground wall. The head components were chosen to withstand the vacuum, corrosive
gas and high temperature (280° C). A coaxial cable links the probe head to probe body
placed outside the vacuum chamber. The components R_1, R_2 and C_2 in the probe body
are adjusted to have the voltage division 1/500 in the band DC to 100 MHz. The signal
is transmitted to a high impedance operational amplifier used as a voltage follower. The
resistance R_3 corrects the operational amplifier offset. The probe body is finally connected
to a floating oscilloscope with a coaxial cable of $50\ \Omega$ impedance.

Measurement of the plasma power

The effective power dissipated in the plasma (P_{pl}) could be directly calculated by the scalar product of RF current and RF voltage measured at the electrode. However, because the phase difference that would be measured, is very small (2°-3°), phase shifts between the measured voltage and current due to nonideal instrumental and cabling effects can render the measurement meaningless. Moreover, in the high frequency field (13.56 MHz to 100 MHz), calibration of the probe phase would be difficult as, for example, a 4 cm length of coaxial cable has a phase shift of about 1° [1]. So this method is complicated and has only low accuracy in our case.

The most common method is the subtractive method [1, 11–13]. The plasma power P_{pl} is the difference between the delivered power with plasma and the delivered power without plasma when the voltage at the RF electrode is kept constant (assuming a loss less network). The delivered power is $P_{in} = [P_{fwd} - P_{ref}]$ where P_{fwd} is the incident power measured at the matching box entry, and P_{ref} is the reflected power measured at the matching box entry. The RF electrode voltage is kept constant by adjusting the level of the RF generator power and the matching conditions. Perrin *et al* [11] have shown that the measurement of the power dissipated in the plasma by the subtractive method is consistent to ±10% with the current-voltage method.
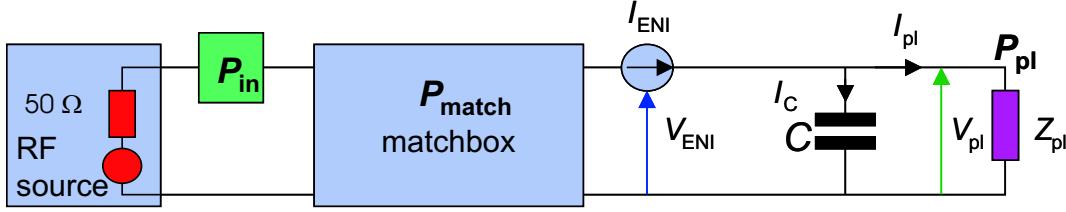

Figure 2.6: *Equivalent circuit of a RF reactor with a small electrode area. The ENI probe allows us to measure current and voltage after the matching box. Stripline and reactor are modelled by the capacitance C. The plasma impedance is represented by Z_{pl}*

In the CRPP we use a modified subtractive method more suitable for a large area reactor. In a small area reactor, the stripline and the reactor can be modelled by a capacitance C (cf. figure 2.6). This capacitance C is very large so I_C is very large compare to I_{pl}. So when the RF electrode voltage V_{RF} (or current I_{ENI}) is the same with and without plasma, the same current I_C passes through the reactor circuit (represented by C):

$$V_{RF}^{VAC} = V_{RF}^{plasma} \quad \Rightarrow \quad I_C^{VAC} = I_C^{plasma} \tag{2.3}$$

Hence the same power is lost in the reactor circuit with and without the plasma. Therefore the power absorbed by the plasma is $P_{pl} = [P_{in}^{plasma} - P_{in}^{VAC}]$. But, in large area reactor, the stripline plus reactor is a complicated network and the plasma strongly changes the current distribution, impedance and power losses (cf. figure 2.7):

$$V_{RF}^{VAC} = V_{RF}^{plasma} \quad \Rightarrow \quad I_C^{VAC} \neq I_C^{plasma} \tag{2.4}$$

Nevertheless, if the capacitances of the vacuum RF passage and the stripline are small compared with the showerhead, walls and reactor capacitances, as expected for large area reactors, then the current flow in them can be neglected. The diagram of the figure 2.8(a)

represents the simplified model of the large area reactor without plasma. With a plasma of impedance Z_{pl}, $C_{shower+walls+reactor}$ is combined with Z_{pl} into C_{eff} and R_{eff} (cf. figure 2.8(b)), assuming that there are no losses in the reactor itself.

Finally we use the ENI probe and the current I_{ENI} :

$$P_{IN}^{VAC} = I_{ENI}^2 R_{line} \Rightarrow P_{IN}^{plasma} = I_{ENI}^2 (R_{line} + R_{eff}) \tag{2.5}$$

$$P_{pl} = I_{ENI}^2 R_{eff} = [P_{IN}^{plasma} - P_{IN}^{VAC}] \quad \text{for same} \quad I_{ENI}^2 R_{line} \tag{2.6}$$

It is important to keep $I_{ENI}^2 R_{line}$ constant because R_{line} varies with the square of the frequency (skin depth effect) : $R_{line} \propto \sqrt{frequency}$. R_{line} can be estimated from gradient of P_{pl} vs. I_{ENI}^2 measurements in vacuum for the relevant frequencies.
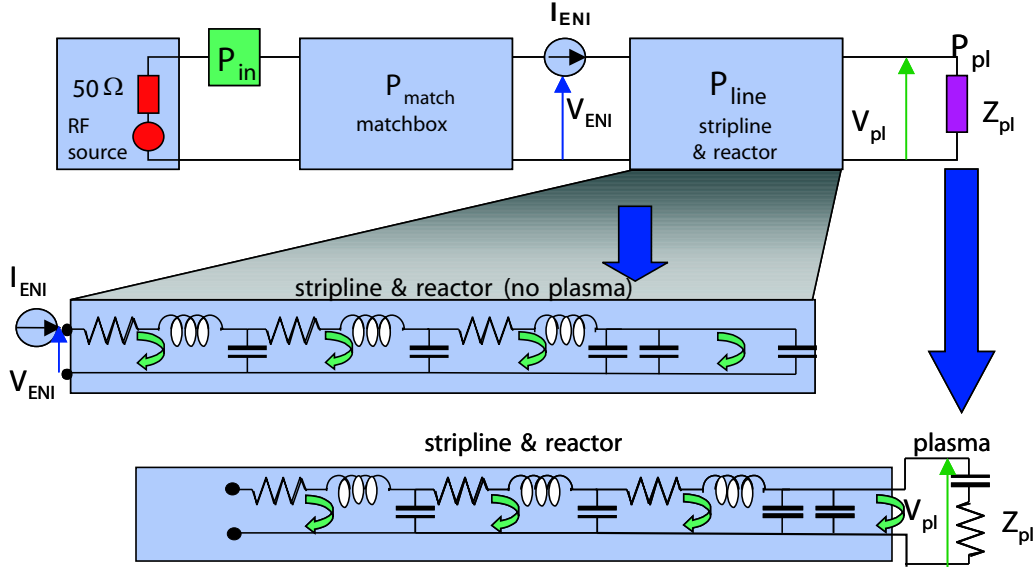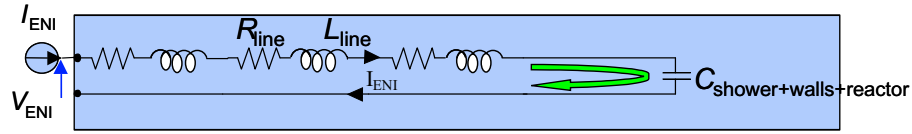

Figure 2.7: *Equivalent circuit of a RF reactor with a large electrode area.*

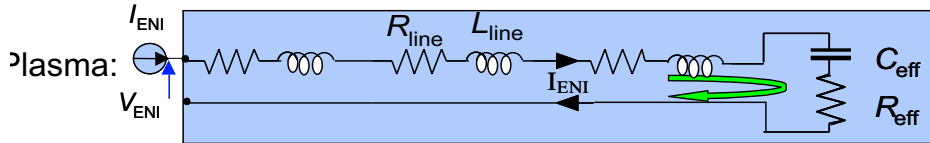

Figure 2.8: *Equivalent circuit approximation of a RF reactor with a large electrode area : without plasma a) and with plasma b).* $C_{eff} \simeq C_{shower+walls}+C_{sheaths}$ *and* $R_{eff} = \frac{R_{pl}}{(1+C_{shower+walls}/C_{sheaths})^2}$.

2.2.2 Plasma intensity, deposition rate, layer characteristics

A system with two optic fibers allows us to measure the plasma intensity, the layer deposition rate and the layer characteristics. Two optical fibers are fixed under the plasma box (cf. figure 2.2(b)). We can see on figure 2.9 the fibers connection in the ground electrode.
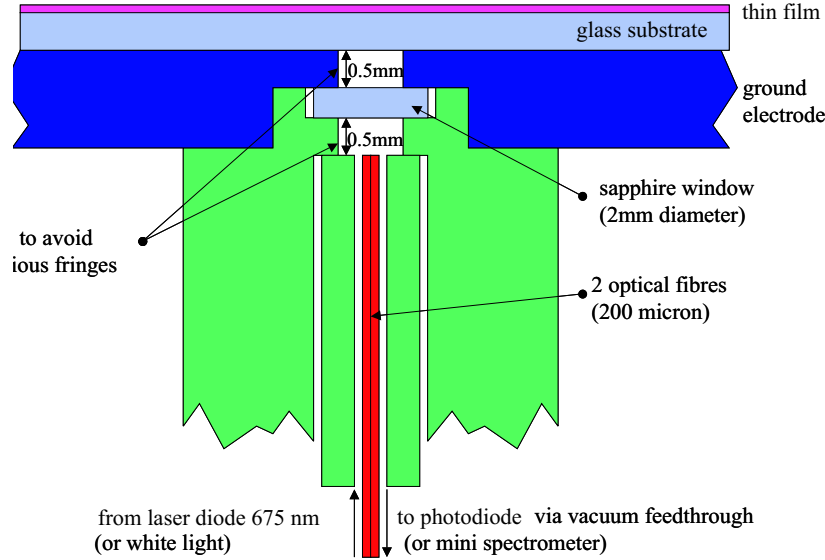
Figure 2.9: *In situ interferometer.*

We can use one fiber to measure the plasma intensity (only for non-depositing plasma) by connecting it to a photo-multiplier. With the two fibers, one connected to a laser diode and the other collecting the reflected light, we can measure the layer deposition rate *in situ*. The intensity, reflected or transmitted, by a thin dielectric layer depends on the interferences between the multiple reflections on layer surfaces. If absorption is neglected, the transmitted intensity I_t for a normal incident light is :

$$I_t = \frac{I_0 T^2}{(1 - R^2)} \frac{1}{1 + \frac{4R}{1-R^2} sin^2(2\pi dn/\lambda)} \tag{2.7}$$

where n is the refractive index of the dielectric, d its thickness, λ the light wave length, T and R are the transmission and reflection coefficients. Reflective intensity is :

$$I_r = I_0 - I_t \tag{2.8}$$

The variation of layer thickness induces the alternation of minima and maxima of the transmitted (or reflected) light. One period corresponds to a thickness variation Δd :

$$\Delta d = \lambda/2n \tag{2.9}$$

We use a laser diode (640 nm) as light source. The reflected light intensity is detected and converted into current by a photodiode. Then the signal is transmitted, via a current-voltage convertor and an amplifier, to a multi-meter and acquired by a computer. For amorphous silicon, the refractive index is $n \simeq 4$ (this value can vary between 3.7 and 4.1, depending on the material quality and the hydrogen content in the layer [14]). Finally,

a)

070301 Amorphous silicon on clean glass

Start 7.6 Å/s
End 6.1 Å/s
12.5 fringes, 1 micron

Intensity [arbitrary units] (y-axis, 0 to 1.2)

Time [seconds] (x-axis, 0 to 1600)

b)

310801 Structure p-doped/intrinsic/p-doped/intrinsic

p-layer
1.6 Å/s

3.2 Å/s
i-layer

1.6 Å/s
p-layer

4.1 Å/s
i-layer

Intensity [arbitrary units] (y-axis, 0,4 to 1,1)

Time [seconds] (x-axis, 0 to 10000)
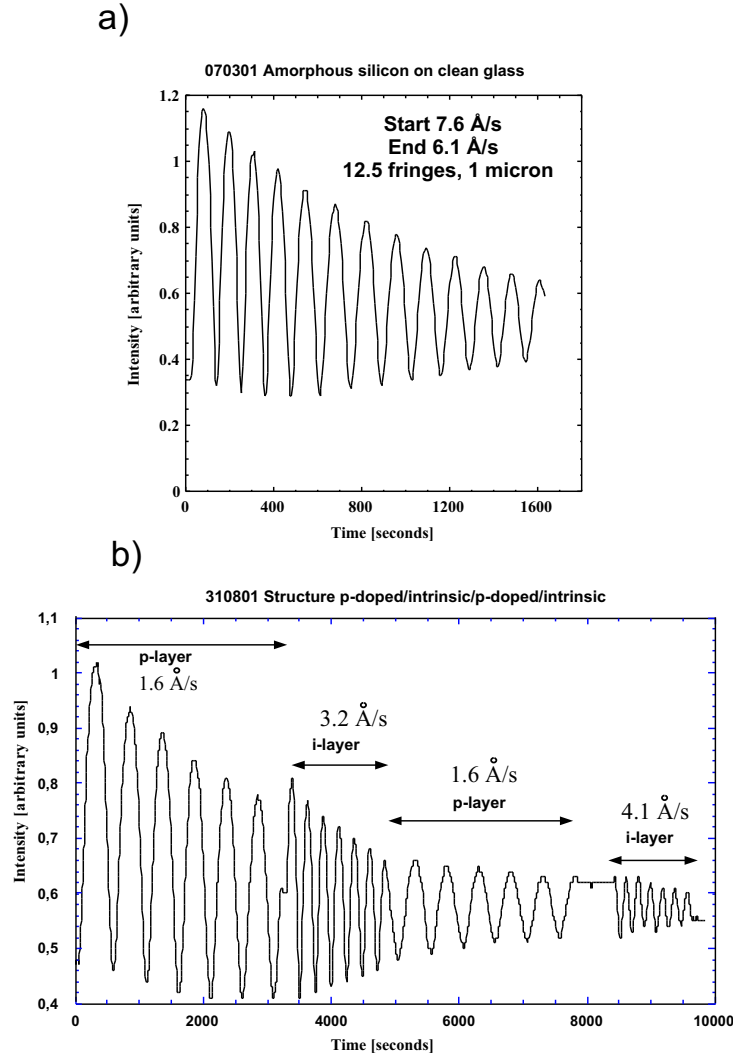
Figure 2.10: *Interference fringes : a) monitoring of aSi:H layer deposition ; and b) p-doped/intrinsic/p-doped/intrinsic sandwich structure for the study of boron contamination (cf. chapter 8).*

we find $\Delta d \simeq 80$ nm per fringe. We calculate the deposition rate R_d by dividing Δd by the period time. At the wavelength of the laser diode, 640 nm, the amorphous silicon is partially absorbant so the fringe amplitude decreases as the layer thickness increases. Thickness limit at 640 nm for the in-situ interferometer is around 35 fringes $\times$ 80 nm = 2800 nm. We can see on figure 2.10(a) the monitoring of an aSi:H layer deposition. The *in situ* interferometer allows us to deposit successively different layers with a good thickness precision (cf. figure 2.10(b)).

Instead of the laser diode, we can use a white light source and analyse the reflected light with a spectrometer. The interpretation of the fringes with a dispersion model allows us to obtain some characteristic layer data such as the energy gap and the refractive index. This interpretation is explained in the chapter 4.

2.2.3 *Ex situ* layer diagnostics

Layer parameters other than deposition rate are important to determine whether a layer is interesting for industrial applications; for example: layer uniformity, layer density

and defect density. Moreover, it is important to get these values in order to study the links between plasma properties and deposited layer properties.

Layer uniformity

The aSi:H layer is deposited on glass substrates (37 cm × 47 cm × 1 mm). The layer uniformity is measured *ex situ* with a global interferometry method [15, 16]. On figure 2.11 we can see the experimental device used for this measurement. The substrate and the layer are illuminated by a white light source from the back. A paper sheet, placed between the substrate and the source, is used to diffuse the light, to have a better uniformity of the light intensity. The transmitted light through the substrate and the layer is collected by a CCD camera via a 707 nm interference filter. Similarly to laser interferometry (cf section 2.2.2), we can observe interference fringes due to the variation of the layer thickness. At 707 nm, the thickness variation between a constructive interference (bright area) and a destructive interference (dark area) is $\Delta d \approx 45$ nm for a-Si:H.
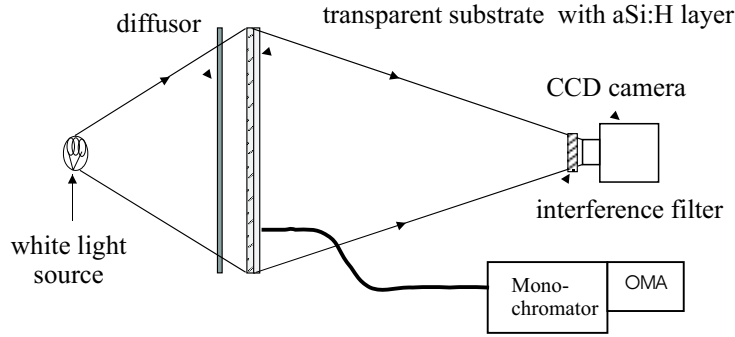

Figure 2.11: *Diagram of the installation used to measure the layer uniformity.*

However, with this method alone, it is not possible to determine if the layer thickness increases or decreases between two interferences [16]. To resolve this ambiguity, we use a spectral interferometric method. As previously, the substrate and the layer are illuminated by a white light source. The transmitted light is collected by a optic fiber at one point of the layer and transmitted to a monochromator. The spectrum of the transmitted light intensity is then recorded by a multi-channel optic analyser (OMA).

According to the equation 2.7, for a fixed thickness layer, the transmitted intensity has minima and maxima, depending on the light wavelength. For an extrema, the value of (nd/λ) stays constant. If we move the optic fiber along a non-uniform area, the maxima (or minima) will move towards higher wavelengths if the layer thickness increases, or towards smaller wavelengths if the layer thickness decreases.

The uniformity of the layer thickness, Δ_e, can be quantified by :

$$\Delta_\mathrm{e} = \pm\frac{\mathrm{h_{max}} - \mathrm{h_{min}}}{\mathrm{h_{max}} + \mathrm{h_{min}}} \tag{2.10}$$

where $\mathrm{h_{max}}$ is the maximal thickness and $\mathrm{h_{min}}$ is the minimal thickness over the substrate area. The global interferometry method allows us to measure Δ_e around $\pm 4\%$ for films of 500 nm thickness. This precision is sufficient for most applications considered here.

Ellipsometry

Ellipsometry is a non-destructive, optical technique which allows to study the optical properties of materials or the thickness of thin films. The main effect taking place is the reflection of linearly polarized light at a surface. By measuring the changes in the polarization state of the reflected light, we get information related to the physical properties of the layer. The relationship is nonlinear and, therefore, a numerical method is used to determine the optical properties and the thickness of the film from ellipsometric data [17].

In the CRPP, we have a UVISEL spectroscopic phase modulated (SPM) ellipsometer from Jobin-Yvon. The ellipsometer diagram is presented in figure 2.12.
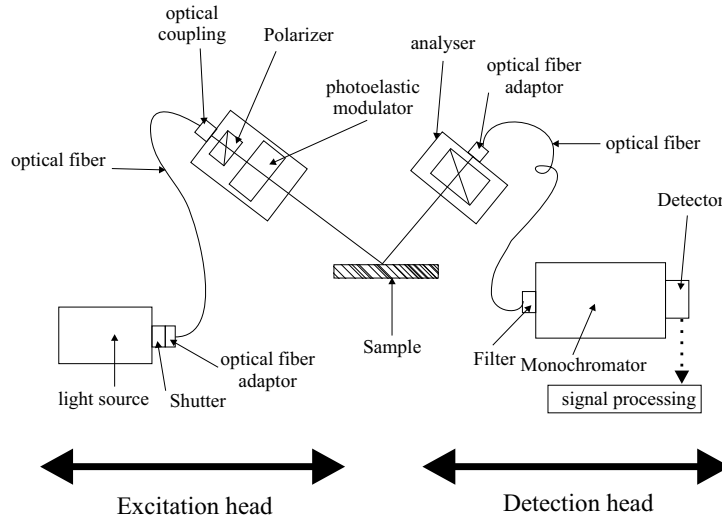

Figure 2.12: *Diagram of spectroscopic phase modulated ellipsometer.*

Ellipsometry allows us to estimate the density of aSi:H layer from the measurement of the dielectric constant and the effective medium approximation [17, 18]. The method will be presented in detail in chapter 4.

Fourier Transform Infrared (FTIR) absorption spectroscopy

Analysis of IR spectra of thin films such as aSi:H can give quantitative compositional information, particularly the hydrogen composition of the film and the layer density. The microstructure parameter R, which is a rough measurement of H-clusters and Si-H bonds on internal surfaces of voids [19], is linked to the layer density [20]. This microstructure parameter R is given by the integral of the absorption band at 2080 cm^{-1} divided by the sum of the integral of the absorption bands at 2000 cm^{-1} (Si-H stretch mode) and 2080 cm^{-1} (Si-H, Si-H$_2$ stretch mode in internal surfaces) [21]:

$$R = \frac{[2080]}{[2000] + [2080]} \tag{2.11}$$

which requires the deconvolution of the absorption bands of the stretch modes at 2000 cm^{-1} and 2080 cm^{-1}. We can see on figure 2.13 (a) the deconvolution of the absorption bands from a dense film (high temperature process) and on figure 2.13 (b) from a porous film (low temperature process). The stronger the 2080 cm^{-1} band, the higher is
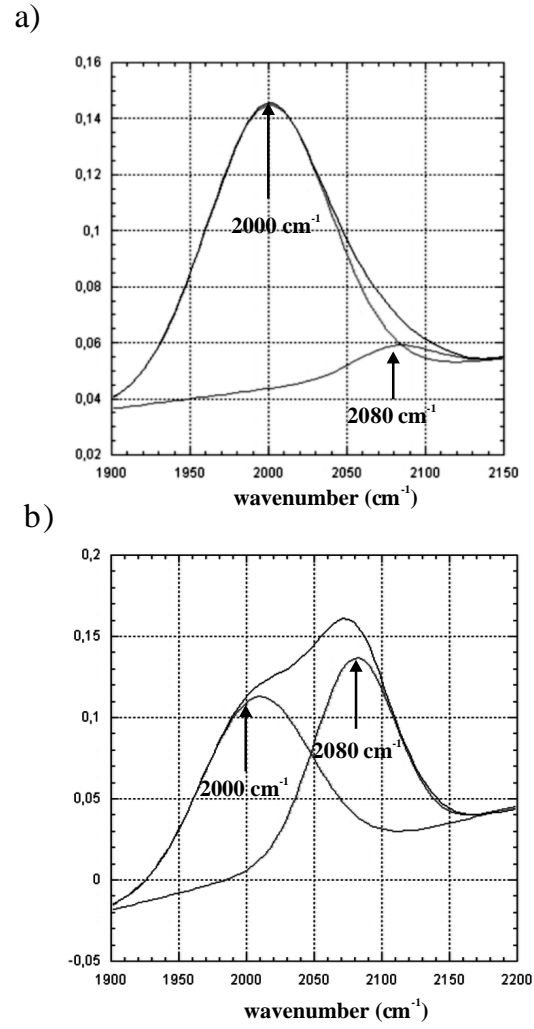
a)

b)

Figure 2.13: *FTIR absorption bands and peak deconvolutions at 2000* cm^{-1} *and 2080* cm^{-1} *of a) dense aSi:H layer R=0.06 and b) a porous aSi:H film R=0.44.*

the microstructure parameter R. This method used to estimate microvoids in a layer is compared to the ellipsometric measurement of layer density in section 4.4.

Chapter 3

RF matching design and power transfer efficiency

3.1   Principles of impedance matching

If the discharge is driven directly by an RF power source, then generally power is not tranferred efficiently from the source to the reactor [1]. To understand this, consider a reactor modeled as a load having impedance $Z_r = R_r + jX_r$, where R_r is the reactor resistance and X_r is the reactor reactance. The power source (RF generator) connected to the reactor (Z_r) is modeled by its Thevenin equivalent circuit, consisting of a rms voltage source $\tilde{V}_T$ in series with a source resistance (for most commercial generators, $R_T = 50\,\Omega$) (cf. figure 3.1).
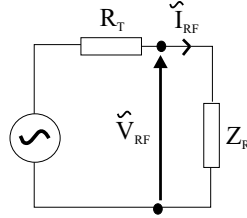
Figure 3.1: *Generator connected to a charge.*

The time averaged power which is dissipated into the reactor is :

$$\bar{P} = Re(\tilde{V}_{rf}\tilde{I}_{rf}^*) \tag{3.1}$$

where $\tilde{V}_{rf}$ and $\tilde{I}_{rf}$ are the complex rms voltage and current through Z_r. By solving for $\tilde{V}_{rf}$ and $\tilde{I}_{rf}$ for these series elements, we obtain :

$$\tilde{I}_{rf} = \frac{\tilde{V}_T}{R_T + R_r + jX_r} \tag{3.2}$$

$$\tilde{V}_{rf} = \tilde{I}_{rf}(R_r + jX_r) \tag{3.3}$$

By substituting 3.2 and 3.3 in equation 3.1, we obtain :

$$\bar{P} = |\tilde{V}_T|^2 \frac{R_r}{(R_T + R_r)^2 + X_r^2} \tag{3.4}$$

For the source parameters $\tilde{V}_T$ and R_T, maximum power transfer is obtained when $\partial \bar{P}/\partial X_r = 0$ and $\partial \bar{P}/\partial R_r = 0$, which gives $X_r = 0$ and $R_r = R_T$. The maximum power supplied by the source to the load is then :

$$\bar{P}_{max} = \frac{1}{4}\frac{|\tilde{V}_T|^2}{(R_T)} \tag{3.5}$$

If maximum power transfer is obtained, then we say that the source and load are conjugately matched. The ratio of the reflected power $\bar{P}_{ref}$ with the incident power $\bar{P}in$ is given by :

$$\frac{\bar{P}_{ref}}{\bar{P}in} = |\frac{Z_T - Z_r}{Z_T + Z_r}|^2 \tag{3.6}$$

For matching conditions, this ratio tends to zero. It means that the impedance matching between the generator and the reactor minimizes the reflected power towards the RF generator.
Generally, X_r is non-zero and $R_r \neq R_T$. So to match the generator with the reactor, a matching box circuit is mounted between the generator and the matching box.

3.2   Reactor model

The impedance of reactor components, Plasma Box$^{\text{TM}}$, stripline and vacuum passage (cf. figure 3.2) was measured with an impedance-meter Hewlett Packard, type 4193A, between 5 MHz and 110 MHz. The impedance was then modeled with an equivalent circuit using Matlab.
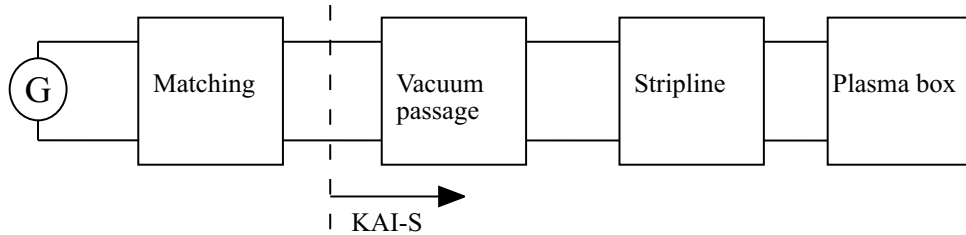

Figure 3.2: *Diagram of the KAI-S components.*

We will find the equivalent circuit for each component, working backwards from the plasma box.
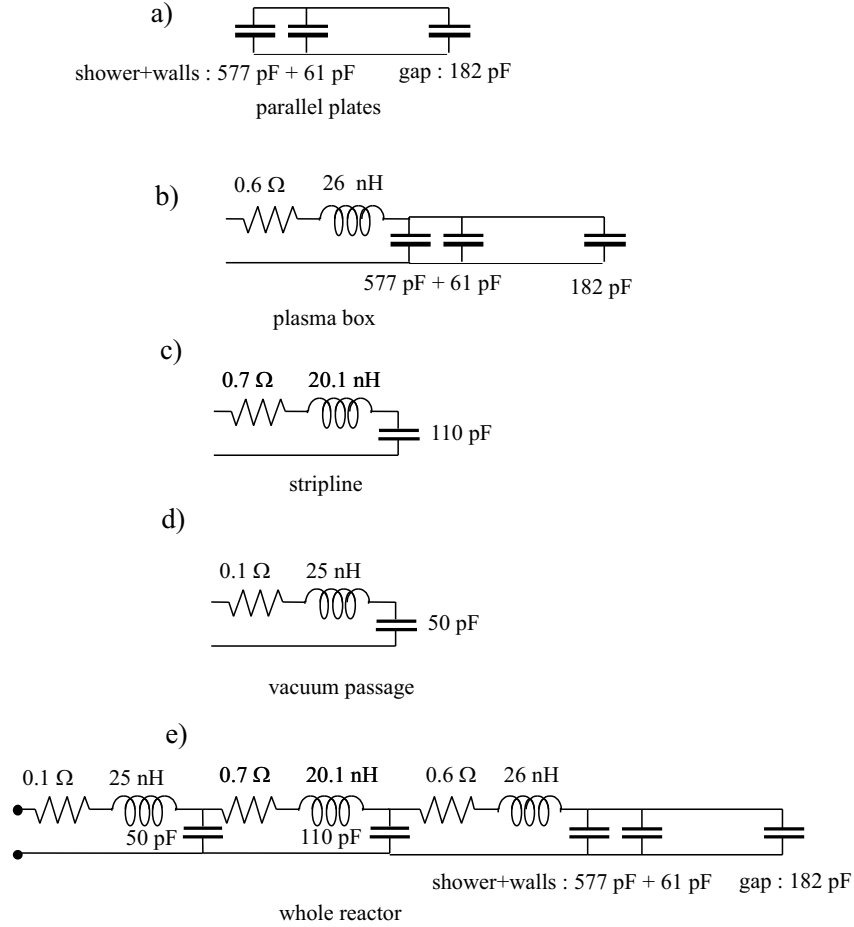
Figure 3.3: *Equivalent circuit of a) the parallel plates, b) the Plasma Box^{TM} electrodes, c) the stripline, d) the vacuum passage, and e) of the whole system.*

3.2.1 KAI-S equivalent circuit without plasma

The equivalent circuit of two parallel plates is a lumped L, C series circuit. We note that KAI-S plates are capacitive below 200 MHz. The equivalent circuit of the Plasma Box^{TM} electrodes is therefore purely capacitive at the frequencies used here ($\leq$ 40.68 MHz). Figure 3.3 (a) shows the equivalent circuit we used to model the reactor parallel plates, including shower and walls, and figure 3.3 (b) shows the equivalent circuit we used to model the whole Plasma Box^{TM}. The values of capacitances and inductances were chosen so that the modeled impedance fits with the measured impedance (measured on the central RF electrode screw, where the stripline is fixed). Figure 3.4 shows the superposition of the modeled and the measured magnitude and phase of the Plasma Box^{TM}. The equivalent circuit with plasma will be described in the next section.

Around a working frequency of 13.56 MHz, there are two ways to model an open stripline, using a transmission line (cf. figure 3.5) or a lumped L,C series circuit (cf. figure 3.3 (c)). In the transmission line model, the circuit impedance of an open stripline is $Z_{open} = -jZ_0.cot(2\pi/\lambda)$ where Z_0 is the characteristic impedance, $Z_0 = \sqrt{Z_{open} \times Z_{close}}$ [22, 23]. By fitting the transmission line model impedance with the measured open stripline impedance we obtain $Z_0^{model} = 21\,\Omega$. This value is coherent with the one we obtain when measuring the impedance of the open and closed stripline $Z_0^{measured} \approx \sqrt{40 \times 10} = 20\,\Omega$.
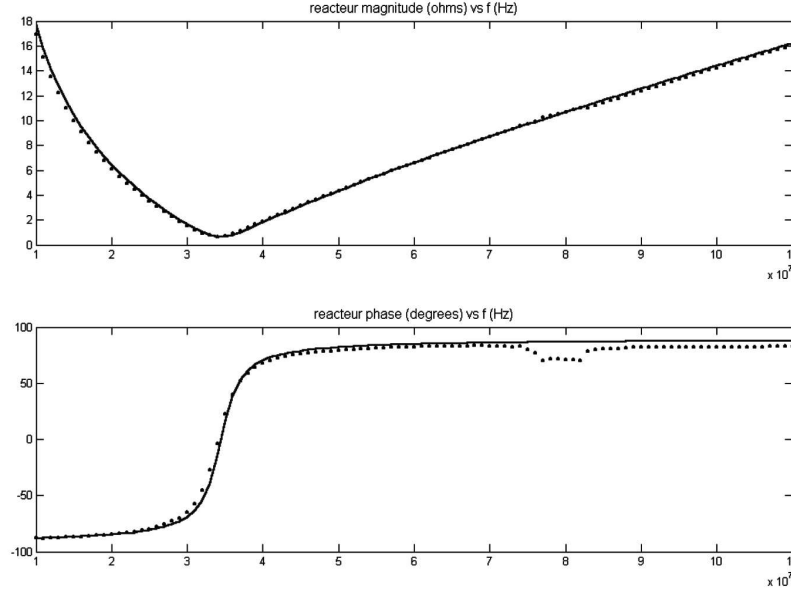
Figure 3.4: *Superposition of measured (dot curve) and simulated (solid curve) magnitude and phase of the Plasma* Box$^{\text{TM}}$. *The disturbance of the measured phase is due to a small movement of the impedance-meter probe during the measurement.*

stripline transmission line, length $l = 0.65$m
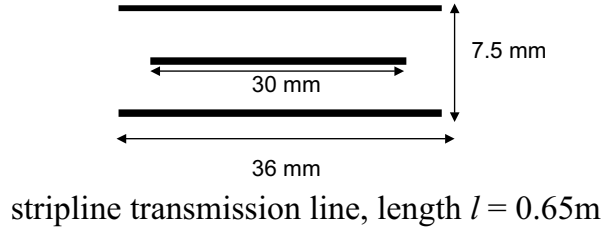
Figure 3.5: *Geometry of the stripline.*

We can see on figure 3.6 the good agreement between the measurement, the transmission line model and the simple lumped circuit model of the open stripline impedance. Note that from the transmission line theory, the stripline capacitance is $C_{stripline} = l/cZ_0^{model} = 111$ pF, where c is the speed of light. This value of $C_{stripline}$ has a good correspondence with the one (110 pF) chosen in the lumped series circuit for a good fit with the measurement.

Finally, the equivalent circuit of the vacuum passage is also a lumped L, C series circuit and the total equivalent circuit of the whole reactor is represented on figure 3.3 (e). On figure 3.7 we can check the good correspondence between the measured impedance and the equivalent circuit impedance. For low frequency, the reactor has a capacitive impedance (phase 90°C) due to the high value of the Plasma Box$^{\text{TM}}$ capacitance.

We observe a first series resonance (resonance between a inductance and a capacitance in series) at 18.8 Hz. Between 18.8 MHz and 80 MHz, the reactor is inductive (phase −90°C), and at 80 MHz , we find a parallel resonance.

Figure 3.6: *Superposition of measured (dot curve), transmission line model (dashed curve) and lumped circuit model (solid curve) impedance magnitude and phase of the stripline.*

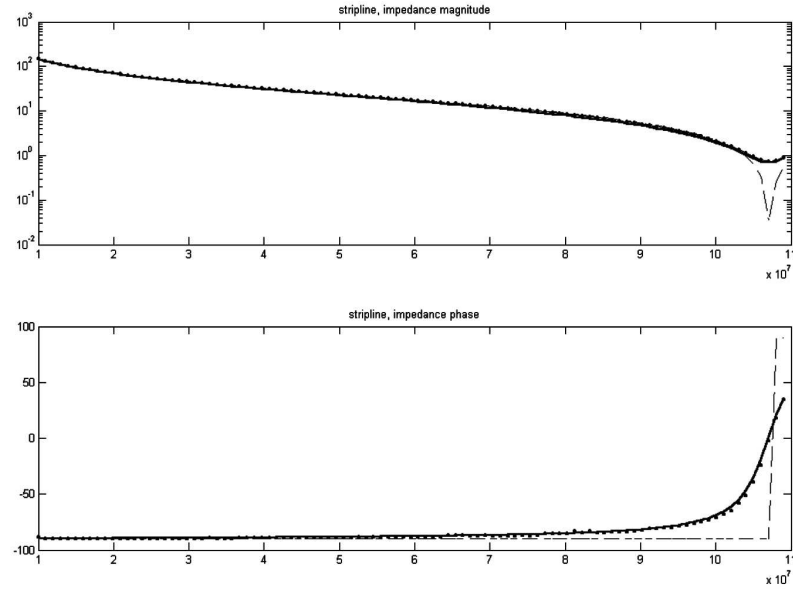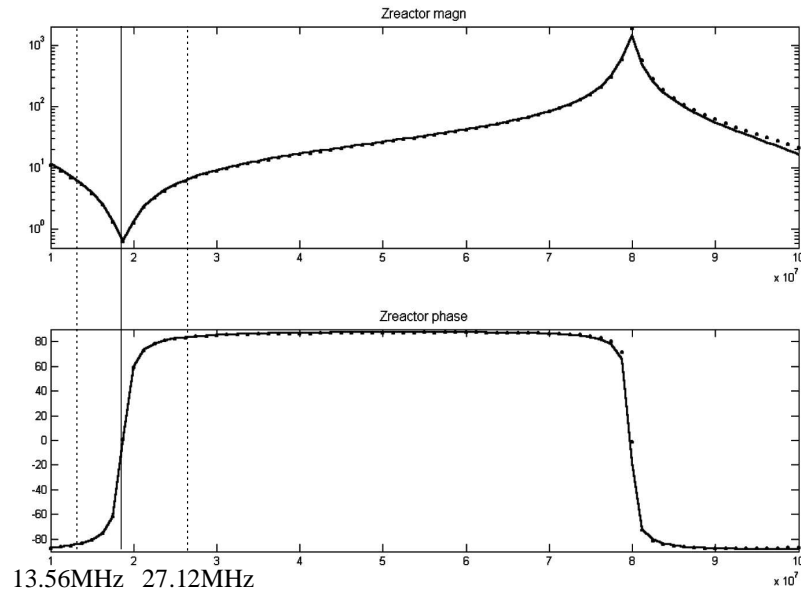Figure 3.7: *Superposition of measured (dot curve) and simulated (solid curve) impedance magnitude and phase of the reactor.*

3.2.2   KAI-S equivalent circuit with plasma

Since frequency-dependent impedance measurements cannot be done when a plasma is on, a model is only presented in this section. In presence of a plasma, the electrode gap capacitance is replaced by a sheath capacitance and a plasma resistance (cf. figure 3.8 (a)). On figure 3.8 (b) is represented the transformed equivalent circuit of the Plasma Box^{TM} with the plasma and, on figure 3.8 (c), the equivalent circuit of the whole reactor. The values of C_{eff} and R_{eff} are given by the formula :

$$C_{eff} = C_{shower+walls} + C_{sheaths} \tag{3.7}$$

$$R_{eff} = \frac{R_{plasma}}{(1 + C_{shower+walls}/C_{sheaths})^2} \tag{3.8}$$

assuming that the plasma resistance is small compared to the shower impedance. On figure 3.9 we can see that adding the plasma in the equivalent circuit model shifts the resonance to 17 MHz and increases slightly the reactor resistance from $0.73\,\Omega$ to $0.95\,\Omega$ at 27,12 MHz.

The reactor impedance is never $50\,\Omega$ real so it is necessary to use a matching box circuit between the generator and the reactor to maximize the transmitted power. At 13.56 MHz, in the capacitive part of the reactor impedance, we use a commercial (Dressler, type Variomatch 1310) L type matching circuit. For higher frequency, particularly 27.12 MHz, we built our own matching box circuit.
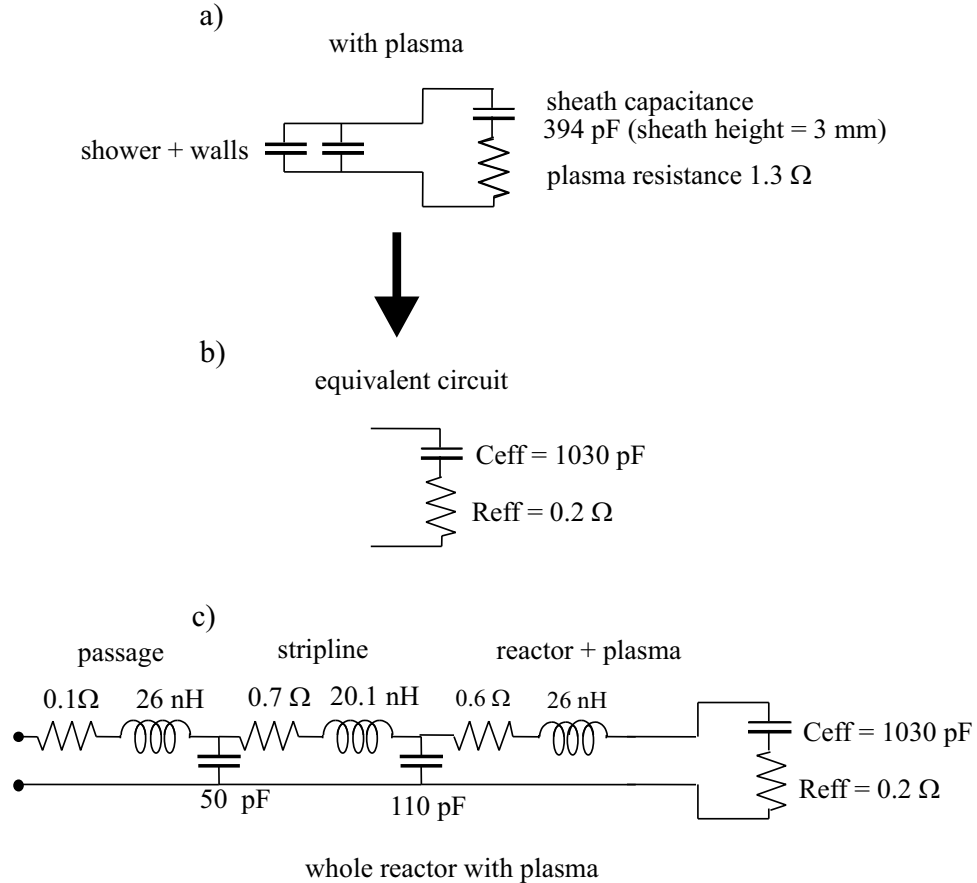

Figure 3.8: *Equivalent circuit with plasma of a) the Plasma Box^{TM}, b) transformed equivalent circuit of the Plasma Box^{TM}, c) the whole system.*
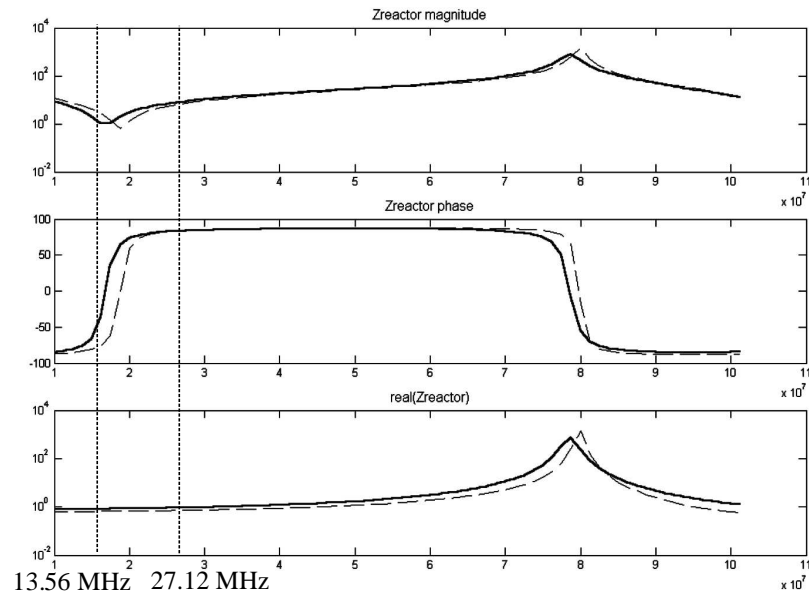
Figure 3.9: *Modelled impedance magnitude, phase and resistance of the reactor with plasma (solid curve) and without plasma (dashed curve).*

3.3   Matching box circuit design for 27.12 MHz

In this section we will examine the various ways to achieve the best matching circuit with the minimum power loss. The most common matching circuit types are the L, T and Π networks (cf. figure 3.10). Between the three networks, we will choose the one with the least power loss.
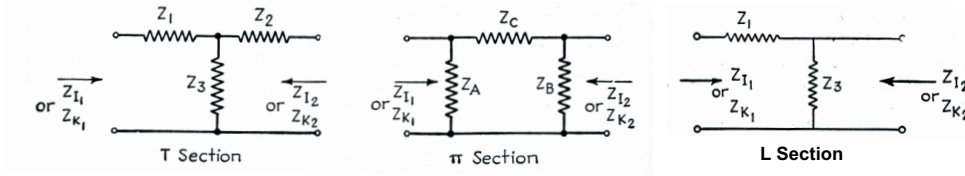
Figure 3.10: *General T, Π and L networks [24].*

3.3.1   Power dissipation in reactive networks

In practical networks, the capacitors have negligible loss, but the resistance of the inductances is not entirely negligible. On the assumption that the currents in the various network branches are not appreciably affected by the dissipation of the inductive elements and that the various inductance elements have a ratio of reactance to resistance $q_L = \omega L/R$ that is the same for all the inductances, we have :

$$\frac{Power\ lost}{Power\ delivered} = \frac{\delta}{q_L} \tag{3.9}$$

where δ is given on figure 3.11, according to the resistance transformation ratio (between load and source resistance) and the type of network [24]. For a L network, we have δ equal to Q the quality factor of the network (ratio between the reactive part and the resistance part of the network). Considering the impedance transformation ratio R_1/R_2 with $R_1 = Re(Z_{I2})$ and $R_2 = Re(Z_{I2})$ (cf. figure 3.10), and the phase shift θ, the loss increases with increasing transformation ratio, and depends on the phase shift of the network. From figure 3.11 the L network has the least loss of either the T or Π networks. In cases involving a very high transformation ratio, cascaded L networks can be used for a better efficiency. To conclude, we chose the L network for the design of our network circuit for reasons of power transfer efficiency.

Figure 3.11: *Values of δ applicable for T and Π networks, the locus for the L network being dotted on the curves. R_1/R_2 = resistance transformation ratio [24].*

3.3.2   L impedance matching network

The four versions of basic L impedance matching network [23] in figure 3.12 are bound by the relationship :
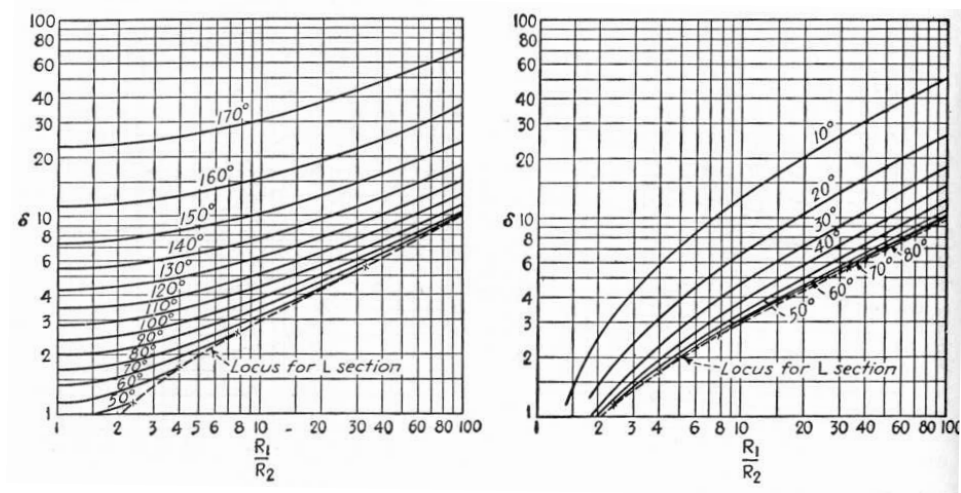
$$X_s/R_s = R_p/X_p = Q \quad \text{(quality factor of the network)} \tag{3.10}$$

where $X = \omega L$ for inductances and $X = 1/\omega C$ for capacitances. Note that the Q of the L network is not arbitrary.
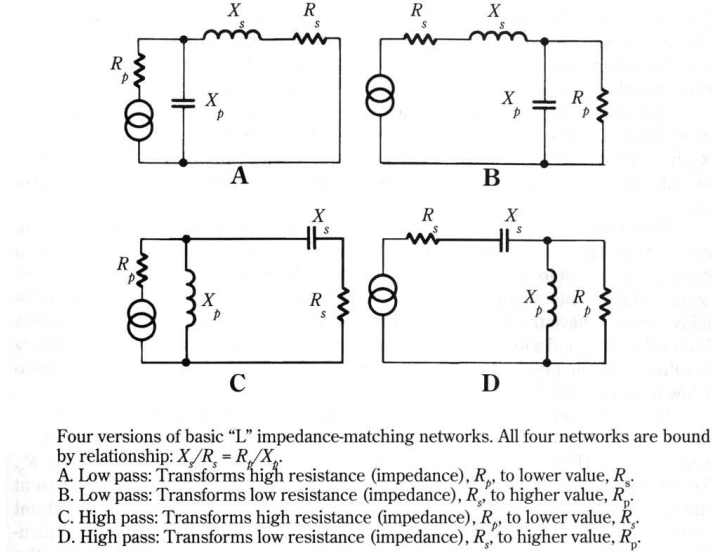

Four versions of basic "L" impedance-matching networks. All four networks are bound by relationship: $X_s/R_s = R_p/X_p$.
A. Low pass: Transforms high resistance (impedance), R_p, to lower value, R_s.
B. Low pass: Transforms low resistance (impedance), R_s, to higher value, R_p.
C. High pass: Transforms high resistance (impedance), R_p, to lower value, R_s.
D. High pass: Transforms low resistance (impedance), R_s, to higher value, R_p.

Figure 3.12: *Four versions of basic L impedance-matching networks [23].*

We have :

$$Q = \sqrt{\frac{R_p}{R_s} - 1} \tag{3.11}$$

Only Q and one of the four parameters (X_s, R_s, R_p, X_p) needs to be known to calculate the remaining three. Such a network has the ability of transforming a low resistance R_s to a higher resistance, R_p (or on the contrary a high resistance R_p, to a low resistance R_s). We can define the power loss fraction, according to equation 3.9 :

$$\frac{Power\ lost}{Power\ delivered} = \frac{Q}{q_L} \tag{3.12}$$

and the efficiency of the network :

$$\eta = \frac{Power\ delivered}{Power\ in} = \frac{1}{1 + \frac{Q}{q_L}} \tag{3.13}$$

We remark that for a better efficiency, we should use high q_L inductors.
In our case, we must transform a low impedance ($R_s = 0.95\,\Omega$ for 27.12 MHz) which is the reactor impedance to $R_p = 50\,\Omega$ (according to the model in section 3.2.2 and figure 3.9). The transformation ratio is 53, which determines the quality factor $Q= 7.2$ and the values of X_s and X_p for a matching condition at 27.12MHz. The ideal matching network circuit is represented on figure 3.13. In practice, the impedance R_s varies somewhat according to the plasma nature (gas, power, pressure). Even if a bandwidth $f_{resonance}/Q$ can be accommodated, variable elements are necessary. Moreover, parasitic inductances in the circuit disturb the ideal L network.
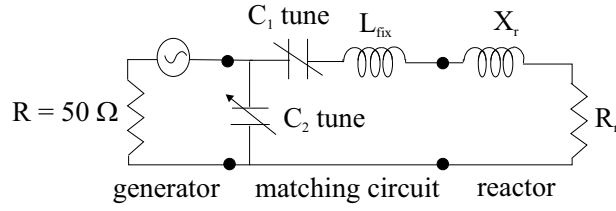
Figure 3.13: *Ideal L matching circuit.*

3.3.3 Real L circuit including parasitic inductance

We can see on figure 3.14 (a) the real matching network circuit, including the parasitic inductances $L_{parasitic}$, L_{stray} and L_{in}. We have two variable vacuum capacitances
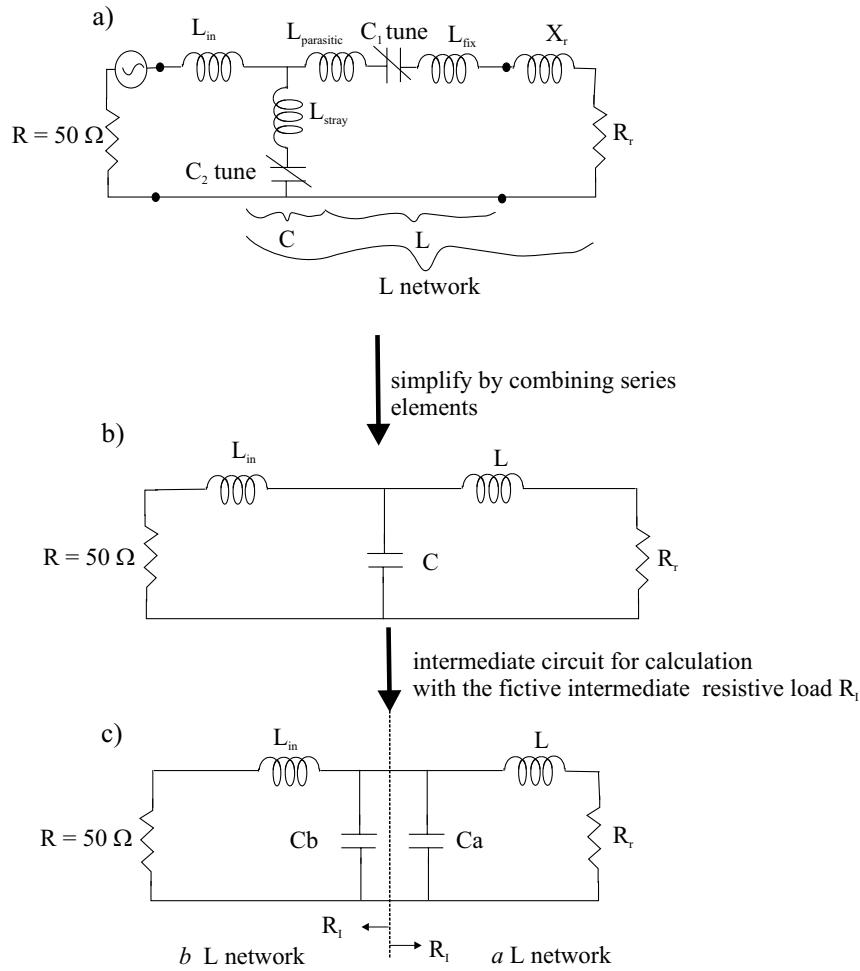
Figure 3.14: *a) Real L matching circuit, including the parasitic inductances, b) and c) the circuit can be simplified for calculation of the elements L_{fix}, C_1 and C_2*

(CV05C-1000W, COMET) which can be varied from 10 pF to 1000pF. The simplified circuit on figure 3.14 (c) allows us to calculate the values of the circuit elements C_1, C_2 and L_{fix}. For the *a*-L circuit, we have :

$$Q_a = \frac{\omega L}{R_r} \tag{3.14}$$

$$Q_a = R_I.\omega C_a \tag{3.15}$$

$$R_I = R_r(1 + Q_a^2) \tag{3.16}$$

For the b-L circuit, we have also:

$$Q_b = \frac{\omega L_{in}}{R} \tag{3.17}$$

$$Q_b = R_I.\omega C_b \tag{3.18}$$

So the value of Q_b is fully defined and R_I is :

$$R_I = R(1 + Q_b^2) \tag{3.19}$$

The resolution of the equations system fixes the value of Q_a :

$$Q_a = \sqrt{\frac{R}{R_r}(1 + \frac{\omega^2 L_{in}^2}{R^2}) - 1} \tag{3.20}$$

For a given frequency, knowing Q_a gives us the value of L, C_a and C_b

$$L = R_r.Q_a/\omega \tag{3.21}$$

$$C_a = Q_a/R_r(1 + Q_a^2)\omega \tag{3.22}$$

$$C_b = C_a.Q_b/Q_a \tag{3.23}$$

According to figures 3.14 (a) and 3.14 (b), we can write :

$$C = C_a + C_b \tag{3.24}$$

$$C_2 = \frac{C}{1 + \omega^2 L_{stray}C} \tag{3.25}$$

and

$$C_1 = \frac{1}{\omega(X_r + \omega(L_{fix} + L_{parasitic} - L))} \tag{3.26}$$

From the impedance measurements, we estimated $L_{in} = 73$ nH and $L_{stray} = 71.5$ nH. To see the matching conditions for C_1, C_2 and L on a frequency range of 10 MHz-100 MHz, we simulated the real L matching network with our conditions, meaning $R = 50\,\Omega$ and $R_r + jX_r = $ measured Z_r (cf. figure 3.15). First, according to the simulation, we see that matching conditions should be possible at 27.12 MHz in the range of the variable capacitances. Second, an inductance L_{fix}, so that $L_{fix} + L_{parasitic} = 120$ nH must be designed. The inductive arm of the L circuit already includes the reactor reactance X_r, which is inductive at 27.12 MHz. So a simple copper tube is enough to reach the matching value for the inductance L_{fix}.

Finally, we can see on figure 3.16 the schematic of our final matching circuit. For matching conditions at 27.12 MHz (no plasma), we compare on figure 3.17 the model of the real L circuit (including all parasitic inductances), connected to the reactor, with the impedance measurement of our built matching circuit connected to the reactor. As we see on figure 3.17, the matching between generator and reactor occurs in the neighbourhood of two close resonances (parallel and series). The series resonance just after the parallel resonance limits the increase of the impedance amplitude, so that its value is around $50\,\Omega$ when the impedance phase is 0°.

Experimentally, at 27.12 MHz (no plasma), we obtain matching conditions for $C_1 = 266$ pF and $C_2 = 324$ pF. When a plasma is on, the impedance of the reactor changes and we must adjust the variable capacitances for new matching conditions: $C_1 = 225$ pF and $C_2 = 250$ pF. Our custom built matching circuit allows us to work also at 40.68MHz, despite low limit values of the variable capacitances.
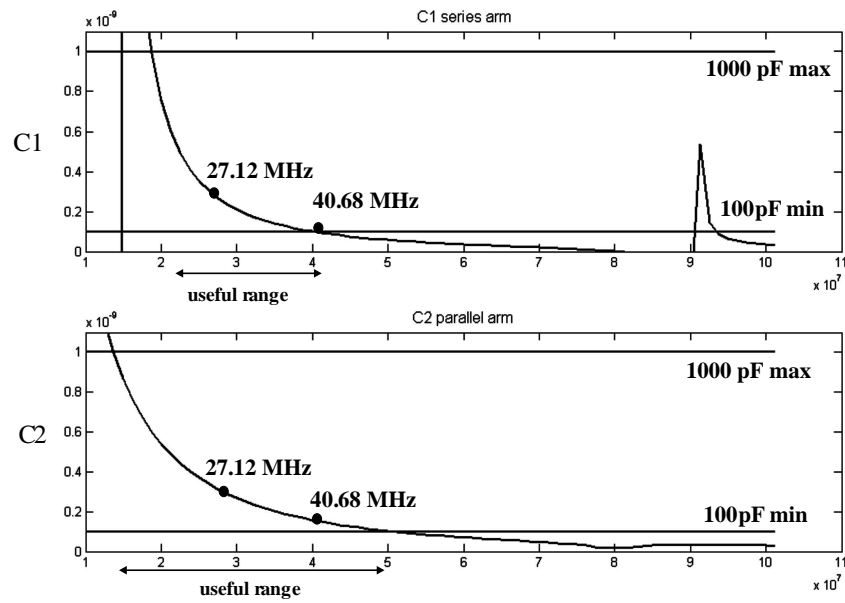
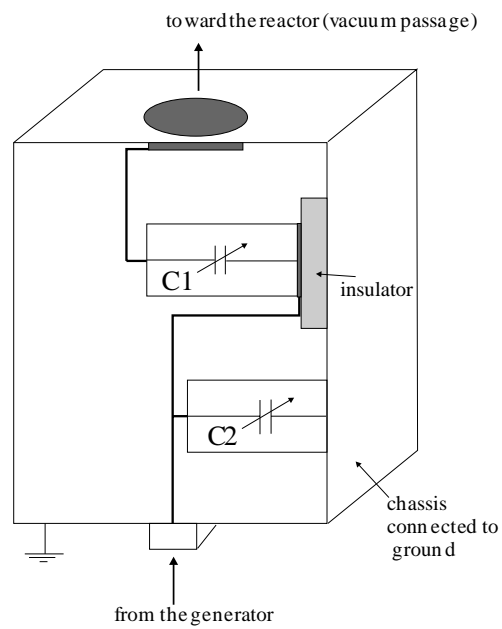Figure 3.15: *Matching values for C_1, C_2 considering the real L matching circuit.*

Figure 3.16: *Schematic of the final matching circuit installed between the generator and the reactor.*
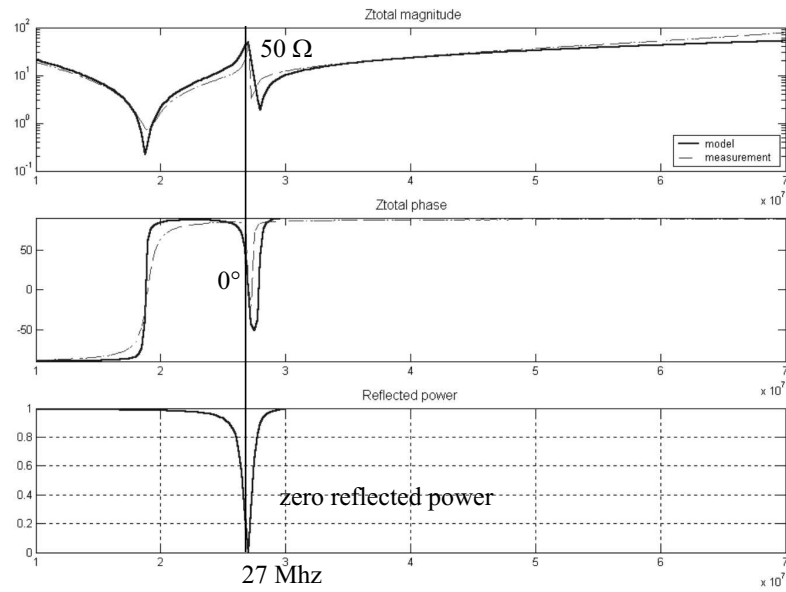
Figure 3.17: *Matching conditions at 27.12 MHz, matching circuit plus reactor : comparison between model and measurement.*

Chapter 4

Optical diagnostics, theory and interpretation

In this chapter, we will present the optical diagnostics used for layer characterization. These diagnostics were already introduced in chapter 2, section 2.2.2 for the in-situ interferometer and 2.2.3 for the ellipsometer, but we will explain here in more detail the theory and how we apply these diagnostics. First we will describe the white light interferometry used to measure the deposition rate and the optical properties of deposited layers. Second, we will apply the ellipsometric measurement to determine the layer density. In the third part we will explain the problems of measuring the density of rough layers by the ellipsometric method.

4.1 Thin film fringe interferometry, white light fringe spectrum

The installation of the in-situ interferometer is described in figure 2.2 (b) and figure 2.9. A laser diode (single wavelength) is used for the simplest measurement of deposition rate. Using a white light source, during the deposition, we can observe the evolution of the fringes spectrum on computer. We can save the spectrum at various times of the deposition (cf. figure 4.5). To eliminate the unknown source intensity and all terms which depend on sapphire we use a dark subtraction method which is described in the following.

4.1.1 Dark subtraction method

Figure 4.1: *Reflection on a single thick transparent layer.*

If we consider a single thick incoherent transparent substrate (glass for example) on figure 4.1, the infinite reflectance R_g^∞ is:

$$R_g^\infty = |r_{as}|^2 + \frac{|t_{as}t_{sa}r_{sb}|^2}{1 - |r_{sa}r_{sb}|^2} \tag{4.1}$$

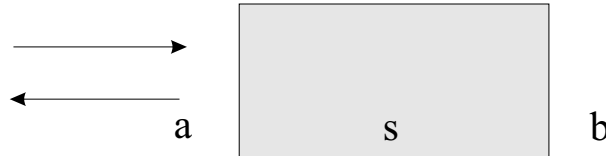Figure 4.2: *Reflection on a single thick transparent layer with an absorbing layer on the opposite side.*

for transparent glass index s surrounded by air (a = b = 1), the reflection coefficients are:

$$|r_{as}|^2 = |r_{sa}|^2 = |r_{sb}|^2 = (\frac{s-1}{s+1})^2 = R \tag{4.2}$$

and the transmission coefficients are:

$$|t_{as}|^2|t_{sa}|^2 = \frac{4}{(1+s)^2}\frac{4s^2}{(1+s)^2} = (1-R)^2 \tag{4.3}$$

Finally, for a single thick transparent substrate the reflectance is:

$$R_g^\infty = R + \frac{(1-R)^2 R}{1-R^2} = \frac{2R}{1+R} \tag{4.4}$$

For glass, s is 1.5 and $R_g^\infty = 7.7\%$. One important hypothesis here is that we consider the transparent thick layer to be 'incoherent'. It means that the instrumental resolution is not high enough to resolve the fringes. The expression of the transmittance R_g^∞ in equation 4.1 is an average over a fringe period [25].

Now we can add an absorbing layer on the opposite side (cf. figure 4.2) which is the configuration of a deposited film on glass that we have with our in-situ interferometer. Using the infinite reflection method or the matrix method [25], the expression of the reflection coefficient r_{sb} becomes :

$$|r_{sb}|^2 = |\frac{r_{sc} + r_{cb}\varphi^2}{1 - r_{cs}r_{cb}\varphi^2}|^2 = R_{gf} \tag{4.5}$$

where

$$r_{sb} = \frac{s-n_c}{s+n_c} = -r_{sb} \qquad r_{cb} = \frac{n_c - 1}{n_c + 1} \qquad \text{and} \qquad \varphi = \exp^{(j2\pi \, dn_c/\lambda)}$$

So, with an absorbing layer on the glass, the reflectance becomes :

$$R_{gf}^\infty = R + \frac{(1-R)^2 R_{gf}}{1 - R R_{gf}} = \frac{R + R_{gf} - 2R R_{gf}}{1 - R R_{gf}} \tag{4.6}$$

Now that we have calculated the reflectance of a transparent thick layer and the reflectance of a system glass plus absorbing layer, we can calculate the intensity of the detected signal after reflections from the sapphire substrate, the glass substrate, and the film-coated glass substrate (cf figure 4.3). For a light source of intensity S, the intensity reflected to the detector from the sapphire window alone is $I_{nosubstrate} = S.R_s^\infty$. The intensity reflected to the detector from the clean glass through the sapphire window is $I_{glass} = S.(T_s^\infty)^2.R_g^\infty$. This assumes that there is no coherent interference between the sapphire and the glass,
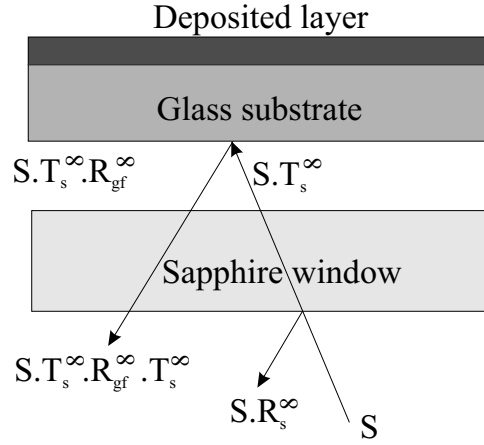
Figure 4.3: *Infinite reflections model.*

because of the air gap between them (cf. figure 2.9). So the total intensity at the detector with a clean glass substrate is :

$$I_{cleansubstrate} = S.R_s^\infty + S.(T_s^\infty)^2.R_g^\infty \tag{4.7}$$

The total intensity at the detector with a film-coated substrate is:

$$I_{film} = S.R_s^\infty + S.(T_s^\infty)^2.R_{gf}^\infty \tag{4.8}$$

To eliminate the unknown source intensity and all terms which depend on sapphire we use a corrected intensity:

$$I_{corrected} = \frac{I_{film} - I_{nosubstrate}}{I_{cleansubstrate} - I_{nosubstrate}} \tag{4.9}$$

$$= \frac{S.R_s^\infty + S.(T_s^\infty)^2.R_{gf}^\infty - S.R_s^\infty}{S.R_s^\infty + S.(T_s^\infty)^2.R_g^\infty - S.R_s^\infty} \tag{4.10}$$

$$= \frac{R_{gf}^\infty}{R_g^\infty} \tag{4.11}$$

which only depends on the film and the glass. According to equation 4.4,

$$R_g^\infty = \frac{2R}{1+R}$$

and according to equation 4.6,

$$R_{gf}^\infty = R + \frac{(1-R)^2 R_{gf}}{1 - RR_{gf}} = \frac{R + R_{gf} - 2RR_{gf}}{1 - RR_{gf}}$$

The intensity $I_{nosubstrate}$ is called the dark intensity and $I_{cleansubstrate}$ is the reference intensity. The dark intensity is acquired by just lifting the substrate with our pins system. The reference intensity is acquired before deposition begins. The reference curve is critical for accurate deduction of the deposited layer. The substrates, glass or corning, should be clean and powder on it must be avoided. The corrected signal with the dark subtraction method, $I_{corrected}$, can be saved at different times of the deposition. With a dispersion model which includes the layer density variations, it is possible to fit the signal and to measure the deposition rate and the reproducibility of the material properties (optical band gap for example) during the film growth.

4.1.2   The Tauc-Lorentz dispersion model and the Effective Medium Approximation

In this section we will describe two models, the Tauc-Lorentz dispersion model and the effective medium approximation, which are currently used in ellipsometry to model film measurements. We use these models to fit the fringes measured by white light interferometry and to obtain information about layer thickness and layer optical properties.

The Tauc-Lorentz dispersion model

Several models provide a general parametric description of the optical functions of silicon. Recently, several workers have used the Forouhi and Bloomer model (F&B) [26]. But it appeared that the F&B model had several fundamental problems which were solved with a new parameterization of the optical functions. This new parameterization is obtained from the Tauc joint density of states and the Lorentz model for the dielectric response for single atoms [27, 28].
If only a single transition is considered, the imaginary part of the dielectric function is given by :

$$\varepsilon_{2TL}(E) \; = \; \frac{AE_0C(E - E_g)^2}{(E^2 - E_0^2)^2 + C^2E^2} \frac{1}{E} \qquad E > E_g \tag{4.12}$$

$$\varepsilon_{2TL}(E) \; = \; 0 \qquad E \leq E_g$$

where E_0 is the peak transition energy, C is the broadening term, E_g is the optical band gap and A is proportional to the transition probability matrix element. The real part of the dielectric function is given by the Kramers-Kronig integral of equation 4.12 :

$$\varepsilon_{1TL}(E) \; = \; \epsilon_1(\infty) \; + \; \frac{2}{\pi}P\int_{E_g}^{\infty} \frac{\xi\varepsilon_{2TL}(\xi)}{\xi^2 - E^2}d\xi \tag{4.13}$$

where P stands for the Cauchy principal part of the integral and $\epsilon_1(\infty)$ has been added as an integration constant. In general, it is expected that $\epsilon_1(\infty) = 1$. The integral can be solved in closed form, and is given by :

$$\varepsilon_{1TL}(E) \; = \; \epsilon_1(\infty) \; + \; \frac{AC}{\pi\xi^4}.\frac{a_{ln}}{2\alpha E_0}.ln(\frac{E_0^2 + E_g^2 + \alpha E_g}{E_0^2 + E_g^2 - \alpha E_g}) \tag{4.14}$$

$$-\frac{A}{\pi\xi^4}.\frac{a_{atan}}{E_0}.[\pi - atan(\frac{2E_g + \alpha}{C}) + atan(\frac{-2E_g + \alpha}{C})]$$

$$+ 2.\frac{AE_0}{\pi\xi^4\alpha}.E_g.(E^2 - \gamma^2).[\pi + 2atan(2.\frac{\gamma^2 - E_g^2}{\alpha C})]$$

$$-\frac{AE_0C}{\pi\xi^4}.\frac{E^2 + E_g^2}{E}.ln(\frac{|E - E_g|}{E + E_g}) \; + \; 2.\frac{AE_0C}{\pi\xi^4}.E_g.ln[\frac{|E - E_g|.(E + E_g)}{\sqrt{(E_0^2 - E_g^2)^2 + E_g^2.C^2}}]$$

where

$$
\begin{aligned}
a_{ln} &= (E_g^2 - E_0^2)E^2 + E_g^2 C^2 - E_0^2(E_0^2 + 3E_g^2) \\
a_{atan} &= (E^2 - E_0^2)(E_0^2 + E_g^2) + E_g^2 C^2 \\
\xi^4 &= (E^2 - \gamma^2)^2 + \frac{\alpha^2 C^2}{4} \\
\alpha &= \sqrt{4E_0^2 - C^2} \\
\gamma &= \sqrt{E_0^2 - C^2/2}
\end{aligned}
$$

The model is assumed to be for 100% dense layer. The porosity of the layer, consisting of a percentage of void in the layer, is introduced in the model by using the Bruggeman effective medium approximation.

Effective Medium Approximation

The Bruggeman effective medium approximation (EMA) allows the calculation of the dielectric constant of a mixture of two media (cf. figure 4.4) [29] :

$$
\delta.\frac{\epsilon_1 - \varepsilon}{\epsilon_1 + 2\varepsilon} + (1 - \delta).\frac{\epsilon_2 - \varepsilon}{\epsilon_2 + 2\varepsilon} = 0 \tag{4.15}
$$

where ϵ_1 and ϵ_2 are the dielectric constants of each medium, δ is the percentage of the medium 1 in the mixture and ε, what we are looking for, is the dielectric constant of the mixture. In our case, ϵ_1 is the dielectric constant of pure amorphous silicon calculated
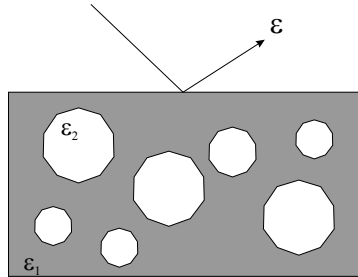
Figure 4.4: *Mixing of two components.*

with the Tauc-Lorentz model, $\epsilon_2 = 1$ (for the void) and δ represents the density of the amorphous silicon layer.

The fitting is performed using a MATLAB non-linear curve fitting function, where six parameters were fitted : the four Tauc-Lorentz parameters (A, C, E_0, E_g), the layer density and the layer thickness. The initial value for the layer thickness should not be too far from the real value, otherwise the fit can be poor. The value of $\epsilon_1(\infty)$ is fixed at 1. With this method, we can distinguish between amorphous silicon and micro-crystalline silicon during the deposition as we can see in figure 4.5. Or we can measure the layer deposition rate and follow the reproducibility of the Tauc-Lorentz fit parameters (meaning the material properties) during the film growth (cf. figure 4.6).

The drawback of the white light interferometry and modeling is that, with six fitting parameters, we must be careful about the physical validity of the fit results, particularly about the layer density. We have checked that, by fixing the density at 100 % or 80 %,

a)

<u>Amorphous silicon</u>
680 nm, E_0 = 3.47 eV, E_g = 1.56 eV, C = 2.16 eV, A = 173

b)

<u>Micro-crystalline silicon</u>
698nm, E_0 = 3.96 eV, E_g = 1.40 eV, C = 0.82 eV, A = 100
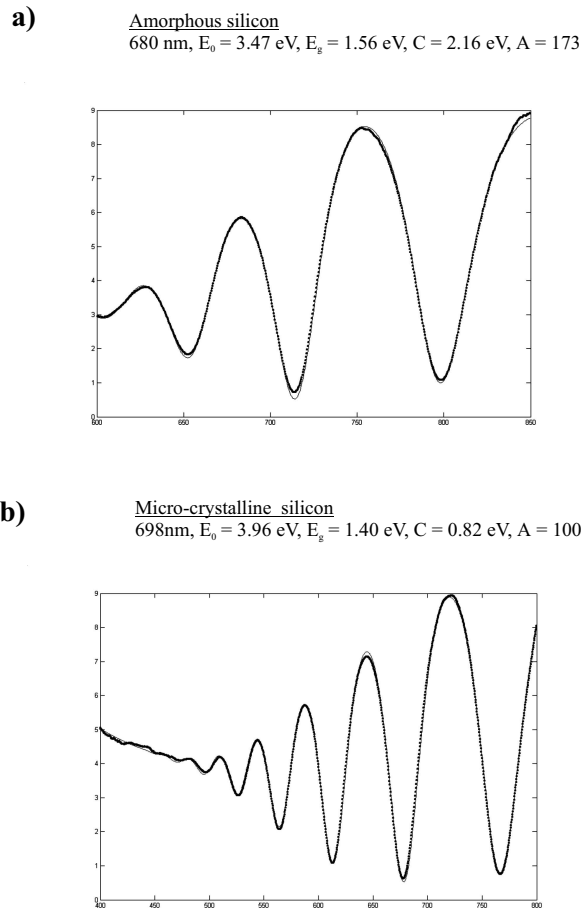
Figure 4.5: *The dashed line represents the white light fringes and the solid line the fitting curve of a) an amorphous silicon layer and b) a micro-crystalline layer. For both fittings, the layer density was fixed at 90 %*

it is always possible to get a good fit of the fringes. In fact, it is necessary to fix the density of the layer as we have done for the example on figure 4.5 and 4.6 (density of 90%). To quantitatively measure the layer density, the ellipsometry method appears an efficient one.

4.2   Layer density measurements with ellipsometry

The ellipsometer was already introduced in section 2.2.3. In this section we will explain, after the measurement of the optical characteristics of the layer, how we use the ellipsometer simulation program to obtain the layer density.

4.2.1   Stages of the ellipsometric measurement

The ellipsometric measurement is the most critical part of the density measurement procedure as false measurements will give, after simulation, false density values. Ellipsometer calibration procedures must be performed carefully. For this we use reference samples which allow us to check the positions of the modulator, analyser and monochromator. It appeared that any imprecision in the angle between the modulator and the
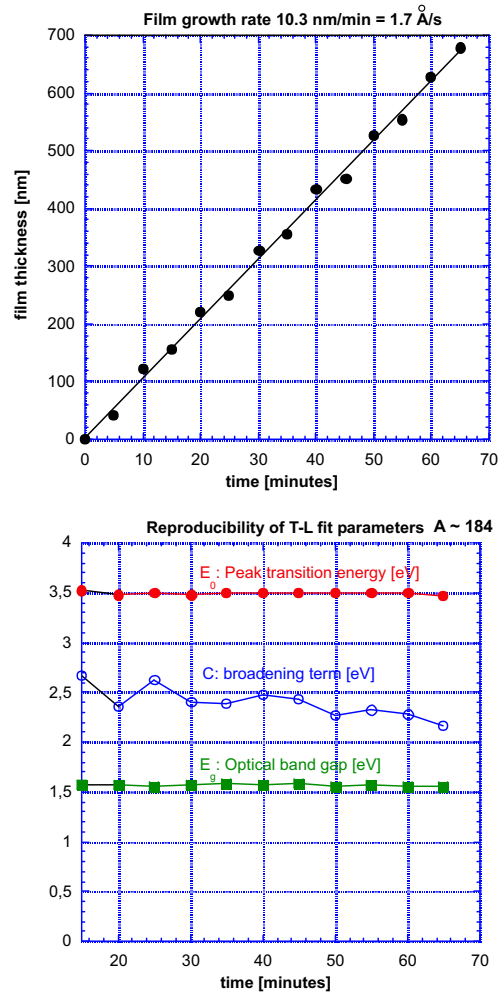
Figure 4.6: *Measurements of deposition rate and reproducibility of material properties during film growth of amorphous silicon.*

analyser, which is fixed in our case, can be a significant source of error as describing in the following.

If we consider how the layer dielectric function of the material is deduced from the ellipsometric raw measurements, the treatment of the signal measured by the detector gives the Fourier harmonic amplitudes S_0, S_1, S_2 [17]. These harmonic amplitudes define $R_\omega = S_1/S_0$ and $R_{2\omega} = S_2/S_1$. From R_ω and $R_{2\omega}$, I_s and I_c, the raw data of the ellipsometer measurements, are defined:

$$I_s = R_\omega - c_{c,\omega}R_{2\omega} + c_{s,0}R_\omega^2 \tag{4.16}$$

$$I_c = R_{2\omega} - c_{s,2\omega}R_\omega + c_{s,0}R_\omega R_{2\omega} \tag{4.17}$$

The coefficients $c_{c,\omega}$, $c_{s,2\omega}$ and $c_{s,0}$ are defined by ellipsometer calibration. For the given position of the polarizer angles of modulator and analyser, I_s and I_c are used to calculate the ellipsometric angles Ψ and Δ and the complex ratio ρ of the Fresnel coefficients r_p and r_s :

$$\rho = \frac{r_p}{r_s} = \tan(\Psi e^{i\Delta}) \tag{4.18}$$

Until now, the angle between analyser and modulator, the incident angle, has not been used. Now, to deduce the dielectric function, we use :

$$\varepsilon \;=\; \varepsilon_0 . sin^2\varphi^0 \{1 \;+\; tan^2\varphi^0 (\frac{1-\rho}{1+\rho})^2\} \tag{4.19}$$

which depends on I_s, I_c and the incident angle φ^0. From the dielectric function, we will estimate the layer density (see below). If the estimated value of the incident angle used in equation 4.19 is wrong, then ε will be wrong. Between 70.3° and 70.9° the layer density error is +/-2 %. So we can compare density values obtained with the same fixed ellipsometer but it is delicate to compare values from different ellipsometers, as we are never sure that the incident angles are identical. Our ellipsometer has its incident angle fixed at 70.3°, modulator angle 0° and analyser angle 45°.

The measurement is done between 1.5 eV and 5 eV (cf. figure 4.7). There are fringes between 1.5 eV and 2 eV because in this range, the light penetrates the whole film thickness and interference fringes are visible due to reflections at the top of the film and the film-substrate interface. Above $\sim$ 2 eV no fringes are observed because light is absorbed before traversing the film, meaning the measurement depends only on the bulk layer properties and the top roughness.
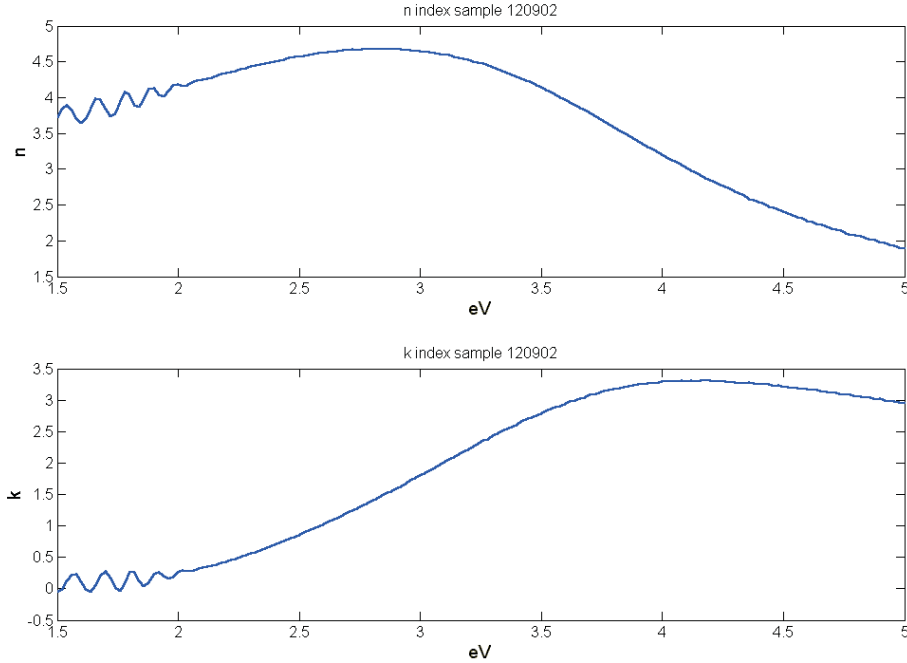
Figure 4.7: *Ellipsometric measurement of an aSi:H layer deposited on wafer.*

4.2.2   Ellipsometric model

The ellipsometer software includes a simulation function which allows users to obtain, from layer optical parameters, information such as roughness thickness and layer density. On figure 4.8 is represented the diagram of the model we used to simulate the substrate plus layer system. The ellipsometer software contains measured references for various materials like amorphous silicon, silicon oxide, micro-crystalline silicon. These

roughness layer 50% aSi 50% void
thickness y

bulk x% aSi (1-x)% void
thickness d

SiO$_2$ 100% thickness 3.3 nm
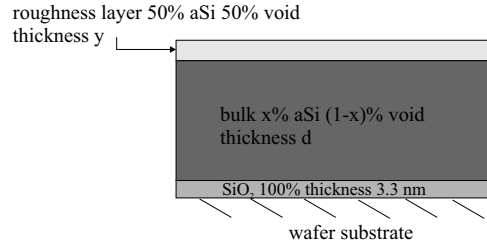
wafer substrate

Figure 4.8: *Diagram of the model used for the simulation.*

references correspond to the measured optical data of typical, good quality, materials. It supposed that the reference materials are 100% dense.

The substrate is a wafer (reference included in the software). The native oxide layer is also a reference from the ellipsometer software. We fixed the native oxide thickness at 33 Å. The bulk is a mixture of void and amorphous silicon, reference aSi.asp [30]. The bulk thickness is given by the in-situ interferometer (cf. section 2.2.2). The bulk density x, the percentage of amorphous silicon in the bulk, is one of our fitting parameters. The effective medium approximation (cf. section 4.1.2) is used to model the mixture. We added on the top a roughness thickness layer, composed of 50% void and 50% amorphous silicon, whose thickness y is our second fitting parameter. We suppose that the roughness thickness is small and that the effect of surface roughness on ellipsometry can be modelled by the effective medium approximation. We will see in the following section how a high roughness can perturb the measurement and induce false layer density estimations.

So we have the following two fitting parameters : x the percentage of aSi in the bulk and y the roughness thickness. For the fit between the model and the measured data, the ellipsometer software uses a Marquardt-Levenberg algorithm which is a standard nonlinear least-squares routine to find the minimum of non-linear equations [31].

As we are not interested in the layer thickness here, we can fit the measurement beyond the fringe region between 2.5 eV and 5 eV. We can see on figure 4.9 the measurement and fitting result of a 1 μm aSi layer deposited on wafer : estimated layer density 89.5 % ±0.336, roughness thickness 10 Åand fitting error $\chi^2 = 0.81$ ($\chi \leq 1$ implies a good fit).

This ellipsometric method was systematically used for the study of the plasma parameter influence on the amorphous silicon layer density, presented in chapter 6.

4.3 Ellipsometric measurement artefact due to highly rough layer

For the fabrication of solar cells, 'Asahi U' (TCO-coated glass) substrates are used [32]. To improve the performance of the solar cells, this kind of substrate is textured, which enhances the light absorption by introducing light scattering at the rough substrate interface [33]. We checked aSi:H layer density on a 37 cm × 47cm 'Asahi U'(rough SnO$_2$) substrate of 3 mm thickness. A silicon wafer, a small piece of corning (borosilicate) glass with and without a film of smooth TCO (ZnO) were also put into the reactor. One micrometer of amorphous silicon was deposited simultaneously on the four substrates. Then, the aSi layer density was measured on each substrate by ellipsometry with the method described above. It can be seen on table 4.1 that the aSi layer deposited on the rough substrate apparently has a very poor density. The difference between the rough
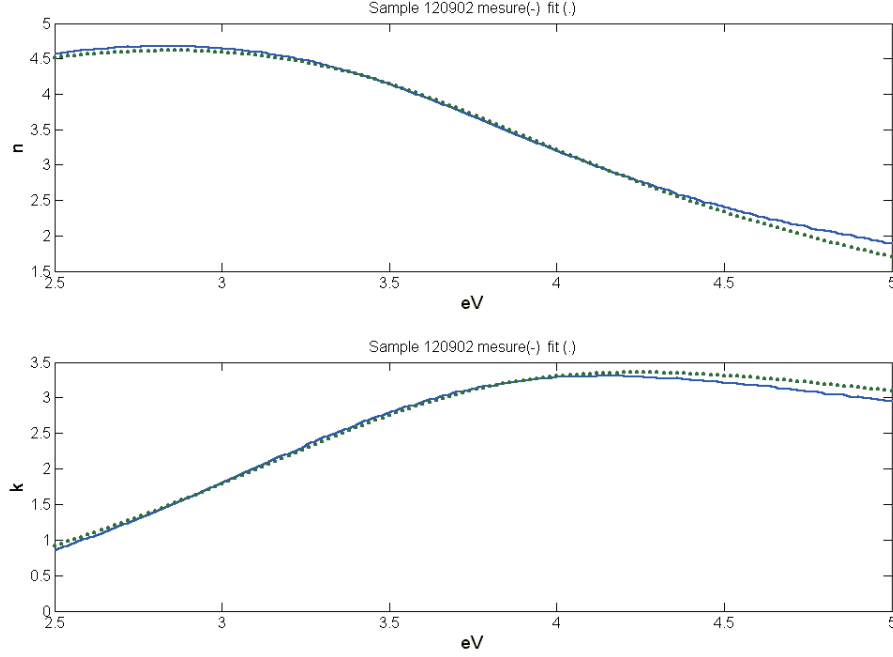
Figure 4.9: *Fitting result : the continuous line is the measurement and the dashed curved is the fit. Layer density is 89.5 % and roughness thickness is 10 Å*

substrate layer and the others can be seen also on the ellipsometric measurements (cf. figure 4.10). The low values of n and k suggest a low layer density or a high roughness thickness.

Substrate	Density	Roughness layer thickness
	% of aSi in the bulk	Å
Wafer	89.5±0.336	10
Corning	89.8±0.347	9.5
Smooth TCO (ZnO)	90.4±0.327	9.3
Rough TCO (SnO$_2$)	70.5±0.480	27

Table 4.1: *Ellipsometric estimations of density and roughness thickness of aSi layer deposited on various substrates.*

The roughness scattering model for the ellipsometer model is complex [34]. One way to distinguish between a low density effect or a high roughness effect is to physically remove the roughness overlayer. To eliminate the roughness, the aSi layer deposited on the rough TCO substrate, was Syton polished on a felt pad [35]. We used Atomic Force Microscopy (AFM) to compare the surface state of the rough TCO substrate, and of aSi layer on rough TCO, before and after polishing, and of aSi layer on wafer. I thank Mrs Laub from EPFL-CIME laboratory for her help during the polish operation and Dr. Rosendo from EPFL-LPCM laboratory for the AFM measurements.

asi layer on : TCO RWE, TCO IMT, corning, wafer
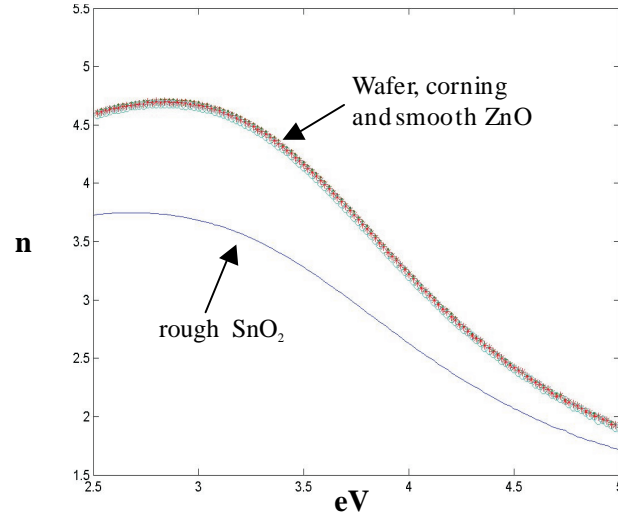
asi layer on : TCO RWE, TCO IMT, corning, wafer
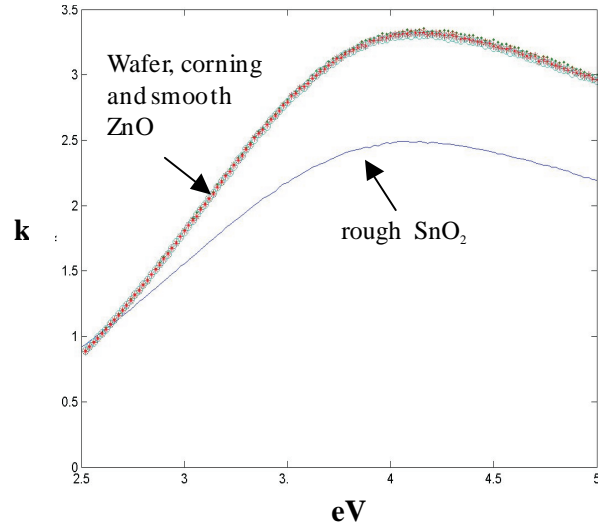
Figure 4.10: *Ellipsometric measurements, n and k index, of aSi layer deposited on wafer, corning, rough TCO and smooth TCO*

4.3.1 Atomic Force Microscopy images of sample surfaces

The AFM allows us to obtain images of surface layers. It also gives us the surface parameters described below :

a) $Ra = < \sum |a_i - \bar{a}| >$ is the mean roughness.

b) $RMS = \sqrt{< \sum |a_i - \bar{a}|^2 >}$ is the root mean square roughness which represents the thickness of the roughness layer.

c) Average height and Maximum Range.

d) Projected area and Real area.

AFM image of a rough TCO (SnO$_2$) coated glass

The 3D AFM image is on figure 4.11. Below the 3D image are cross profiles of the surface. From the total area measurement, the *RMS* roughness of the TCO is 45.4 nm.
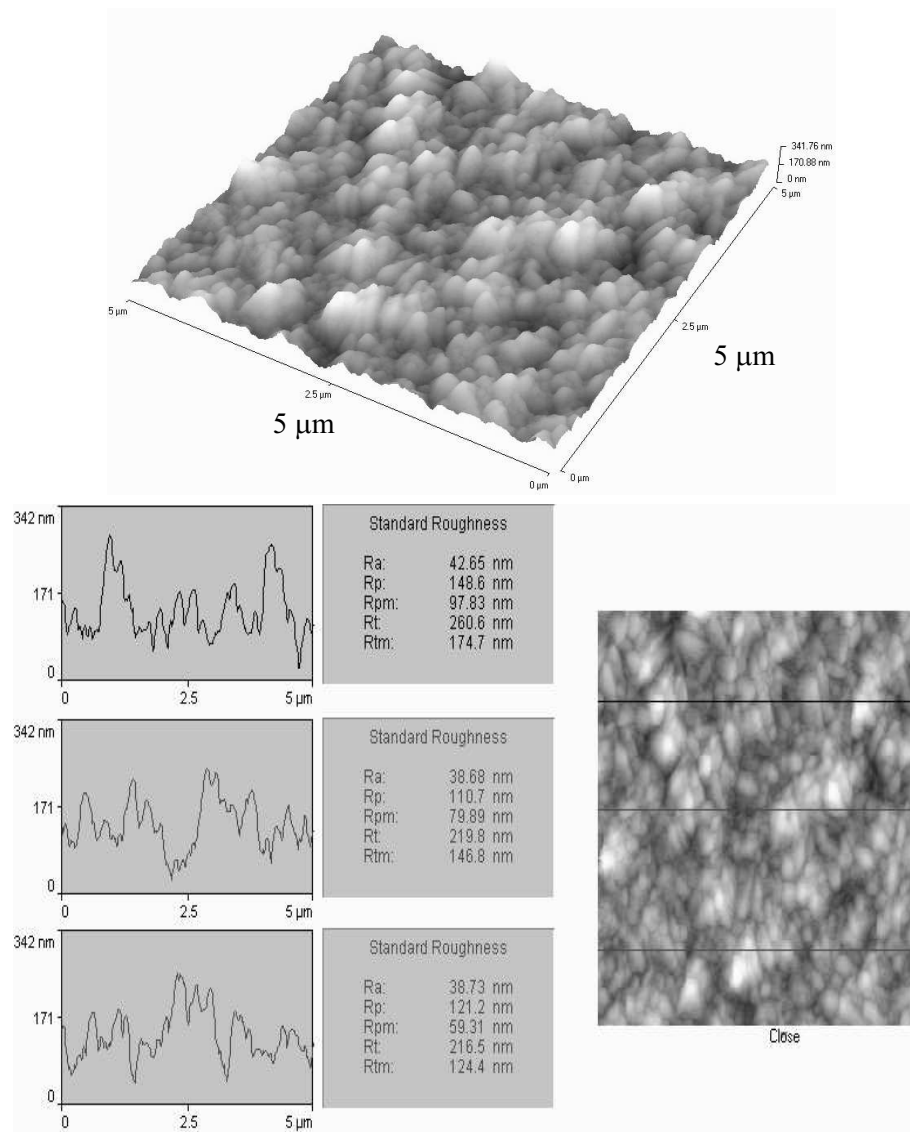
Figure 4.11: *AFM :* SnO$_2$ *on 3 mm glass. 3D image and line profiles.*

AFM image of aSi:H layer deposited on SnO_2

We deposited 1 μm of amorphous silicon with a standard recipe : SiH_4/H_2/pressure/power = 160 sccm/40 sccm/0.2 mbar/56W.

From the total area measurement, the *RMS* roughness is 22 nm. If we compare the line profiles of the substrate surface (figure 4.11) with the ones of the deposited layer (cf. figure 4.12), the deposition is conformal to the large scale roughness, but fills in the fine scale roughness. We note that the roughness of aSi:H on SnO_2 is halfway between the roughness of SnO_2 coated substrate and aSi:H on wafer.
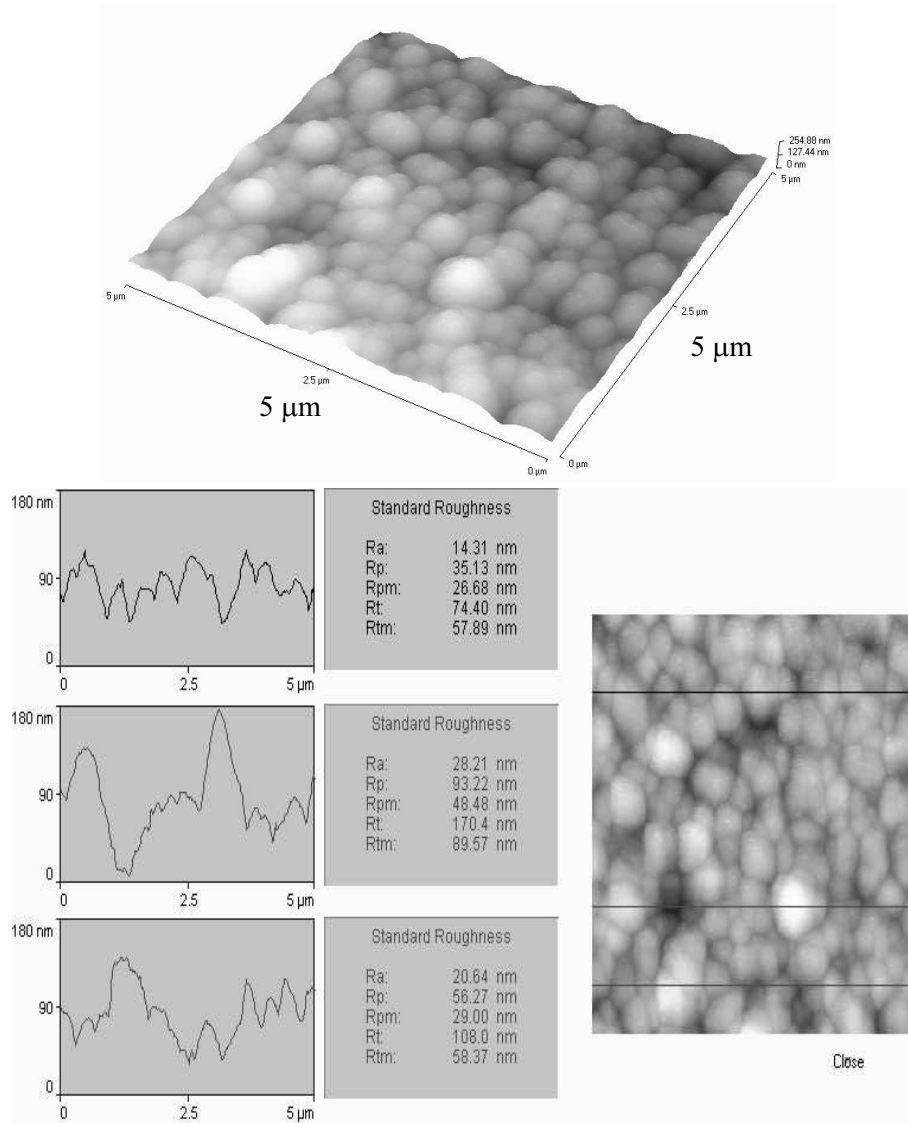
Figure 4.12: *AFM : aSi layer on rough TCO-coated glass. 3D image and line profiles.*

AFM image of aSi:H on silicon wafer

From the total area measurement (cf. figure 4.13), the *RMS* is 3.6 nm, much smoother than all the profiles using SnO_2-coated glass.
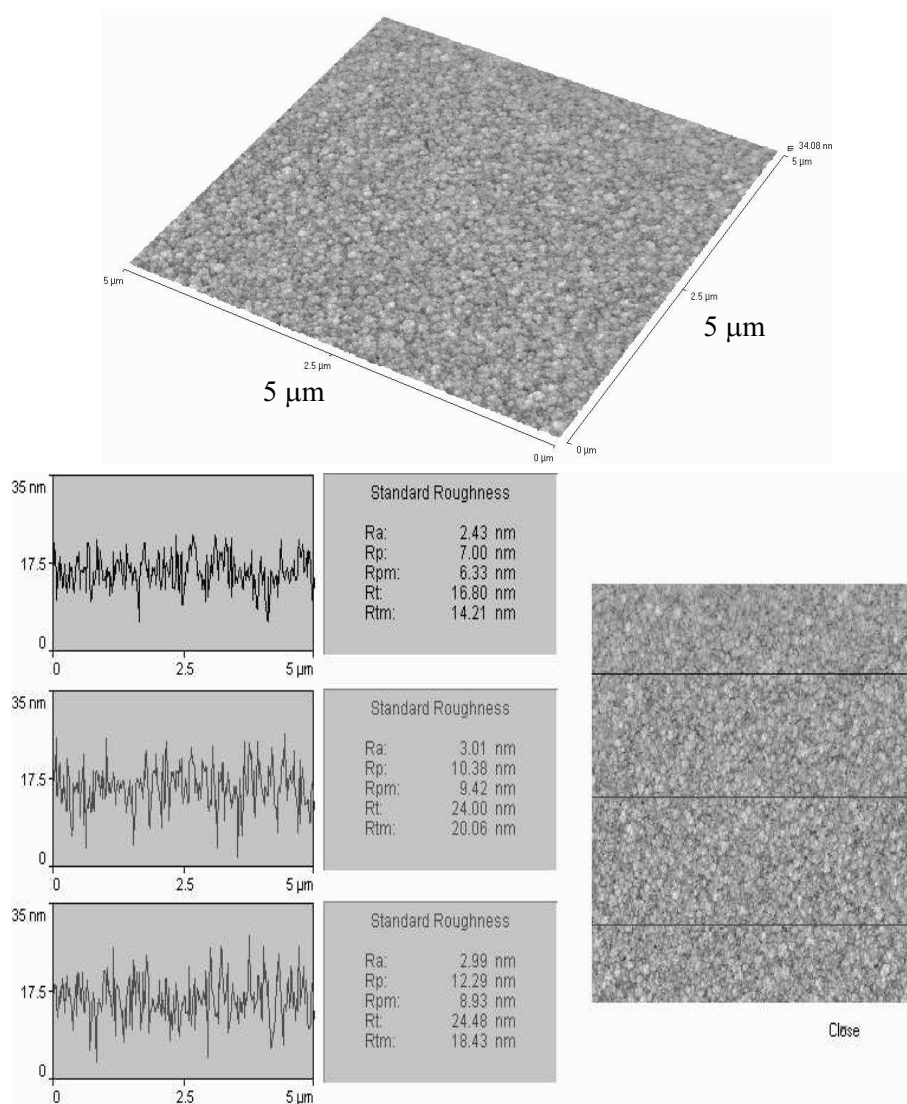
Figure 4.13: *AFM : aSi layer on silicon wafer. 3D image and line profiles.*

AFM image of aSi:H layer deposited on SnO_2 coated substrate after polishing

To eliminate the surface overlayer, the sample was Syton polished on a felt pad and cleaned in a ultra-sonic bath of alcohol [35]. Syton is a colloidal suspension of $0.05\mu m$ silicon dioxide grains. The polishing solution is 3 parts Syton 1 part de-ionized water. It is alkaline (pH 9.8). It needs 90 seconds polishing to remove 500 nm of silicon (mechanical/chemical polishing).

After each polishing sequence, the density and roughness thickness of the sample were estimated with the ellipsometer. A convergence of the measured n and k index is observed. At the end of the treatment, once the convergence is reached, the AFM image of the top layer was repeated (cf. figure 4.14).

Figure 4.14: *AFM : polished aSi layer on rough TCO-coated glass. 3D image and line profiles.*

From the total area measurement, the *RMS* roughness is 3.8 nm. We can remark that, after the polishing treatment, the roughness thickness of aSi:H on rough TCO is the same as the roughness of aSi:H on wafer, although it has a different form.

Finally, table 4.2 summarizes the AFM measurements.

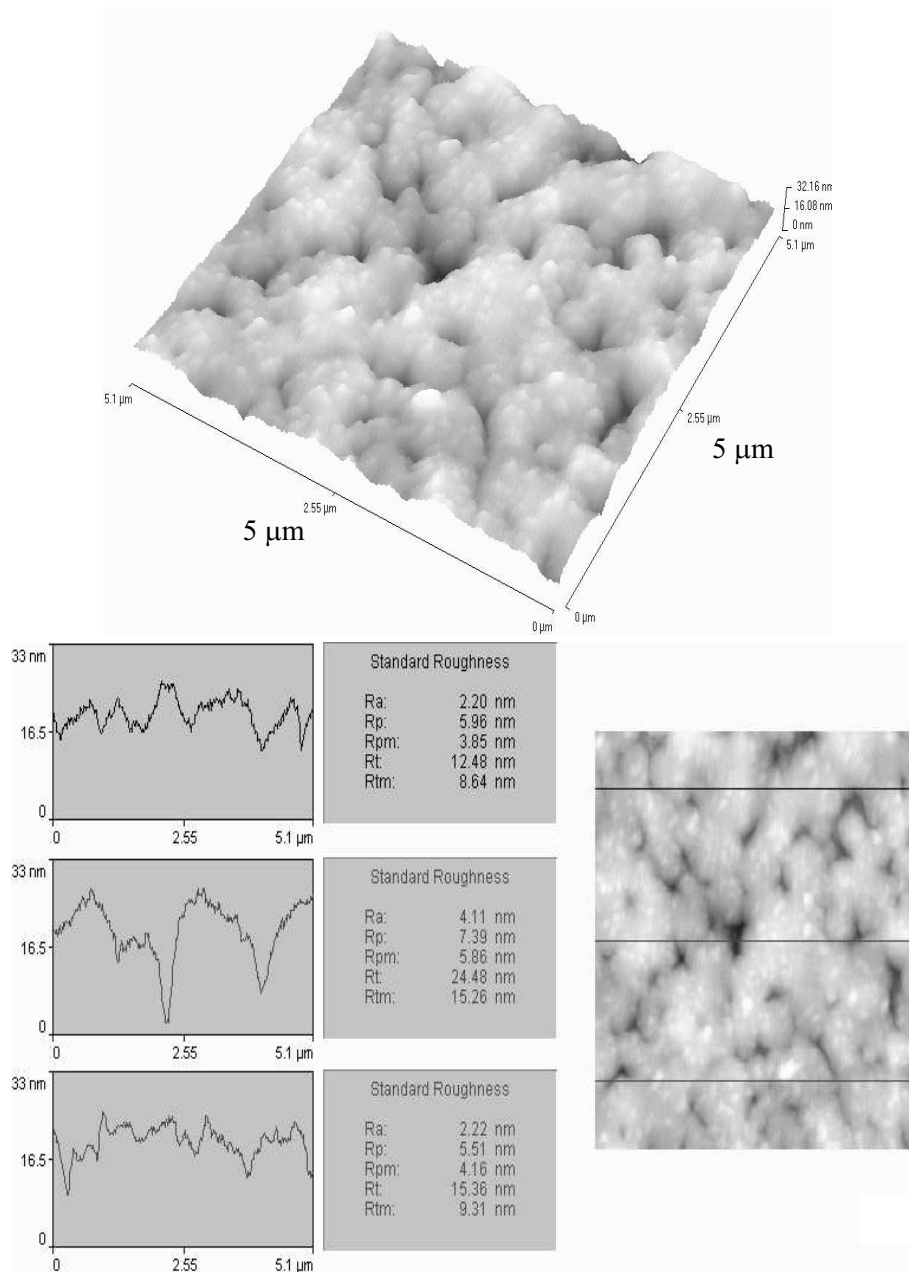| AFM measure	SnO_2	aSi on SnO_2	polished aSi on SnO_2	aSi on wafer
Ra (nm)	35.7711	16.87	2.89	2.8
RMS (roughness thickness) (nm)	**45.3547**	**21.97**	**3.77**	**3.6**
Avg Height (nm)	137.9506	84.38	19.47	15.56
Max Range (nm)	341.76	180	32.13	34.1
Projected area (μm^2)	25.00	25.00	26.01	25.00
Real area (μm^2)	31.17	26.01	26.16	26.00

Table 4.2: *Summary of AFM measurements.*

4.3.2   Polishing operation and ellipsometric measurements

Density layer evaluation during and after the polishing treatment

After several polishing steps, we found a convergence of n and k index, close to the values of aSi layer on wafer. Figure 4.15 shows n/k profiles of the aSi layer on wafer and n/k profiles of aSi layer on rough TCO, at different times of the polishing. Table 4.3 summarizes the ellipsometric estimations of the layer density.

Sample	Density	χ^2	Polishing sequence	Estimated thickness
	%		nb. of figures of eight	nm
aSi on rough TCO	**70.5±0.480**	4.18	0 (before polishing treatment)	~ 1000
1292P12	**83.3±0.425**	1.5	12	1000
1292P42	**86.4±0.335**	0.8	42	985
1292P110	**90.0±0.265**	0.5	110	974
1292P150	**91.4±0.353**	0.7	150 (end of polishing treatment)	962
W120902	**89,5±0.336**	0.81	aSi:H on wafer	1000

Table 4.3: *Summary of ellipsometric estimated densities and thickness .*

It is important to see that after the polishing treatment, the density of the aSi layer on rough TCO reaches 91,4 % which is similar to the density of the layer on wafer.

Estimation of the removed film thickness during polishing

We measured the layer thickness for each polishing step with the ellipsometer. The measured n and k are fitted between 1.5eV and 1.8eV (fringe region) with layer thickness for the fit parameter. Roughness thickness was kept at 22 Å and density at 90%. From the results in table 4.3, it can be said that an average of 15 nm was removed after each polishing step, a total of 38 nm has been removed.

Before the polishing treatment, we were not able to say if the aSi layer deposited on the rough TCO coated glass was very porous or if it had a high surface roughness. But after the polishing treatment, which removed the top roughness, the layer density is equivalent to the density of layers deposited on wafer, corning and smooth ZnO : around 90%. So, in our case, the density of a-Si:H layer seems to be not affected by the nature of the substrate.

It is clear that the ellipsometry estimation of density is strongly perturbed in presence of surface roughness greater than about a 10 nm and that the initial roughness of the substrate has a strong effect on the finale roughness of the deposited layer. Therefore, for a comparative study of the influence of plasma parameters on layer density, it is more suitable to use always the same kind of substrate (a silicon wafer was used in CRPP).

4.4 Comparison between ellipsometric density measurement and I.R. microstructure parameter

The I.R. microstructure parameter R has been defined in the section 2.2.3. Figure 4.16 shows I.R. spectra for layers of various densities deposited on a silicon wafer.

We can see the appearance of 2080 cm^{-1} peak for the porous layer of 87% density. But eye judgement is not sufficient to estimate density values. Peak deconvolution and calculation of R is needed to compare I.R. method and ellipsometric method (cf. section 2.2.3).

Figure 4.17 shows the microstructure parameter R as a function of the layer porosity measured with the ellipsometer. The ellipsometric porosity and IR microstructure parameter are roughly linearly related. It confirms the validity of ellipsometric E.M.A. estimation of layer density. Note that even if there is no detectable peak at 2080 cm^{-1}, there can still remain a residual porosity of 5 % measured with ellipsometer. It is confirmed by Finger *et al.* which said that the microstructure parameter R underestimates the percentage of microvoids in the layer [36].

Compared to the ellipsometric method, I.R. method is simpler but gives only a rough estimation of the layer density.

asi layer on wafer (*)
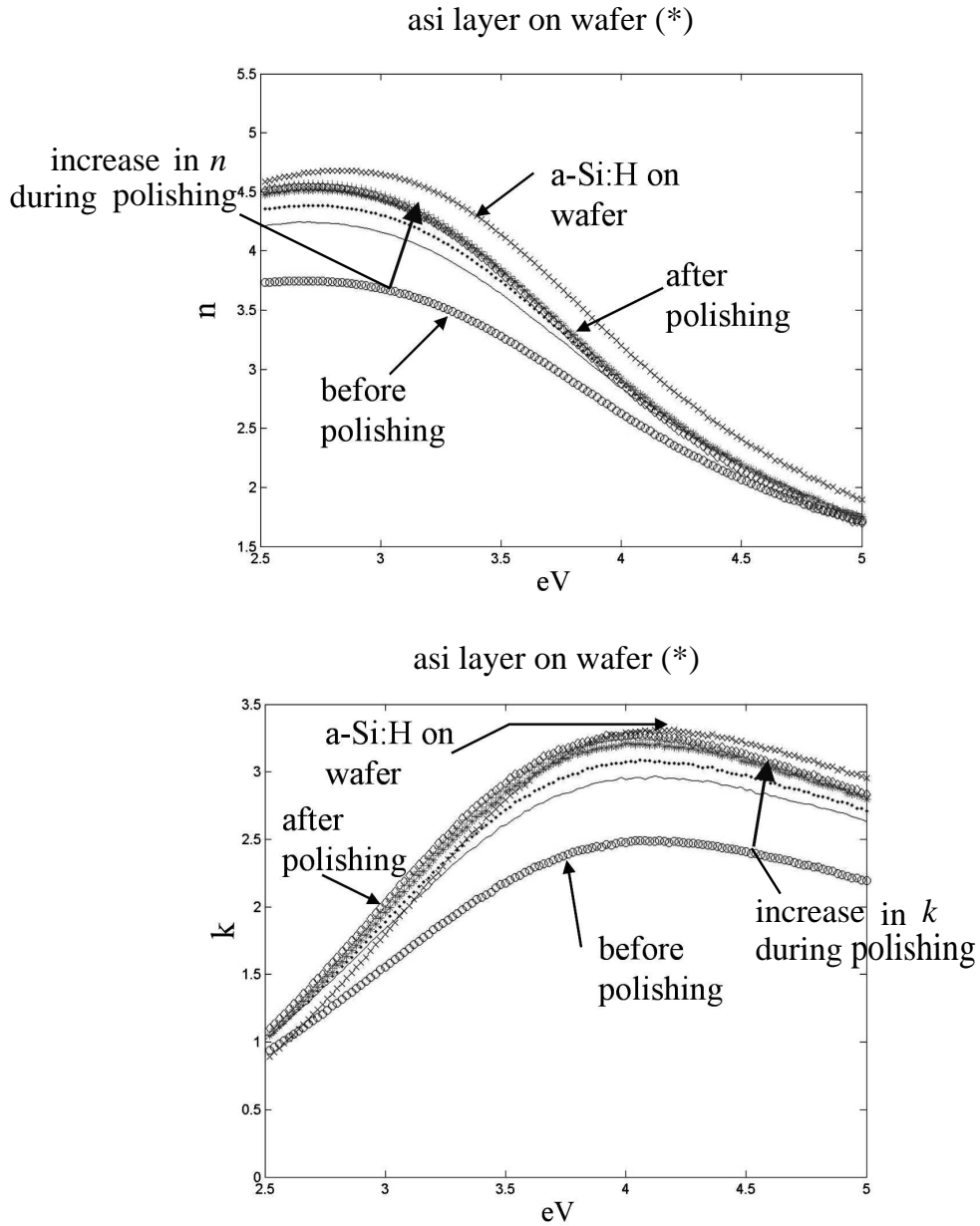

asi layer on wafer (*)

Figure 4.15: *Ellipsometric measurements : aSi on wafer and aSiH on rough TCO at different times of the polishing treatment.*
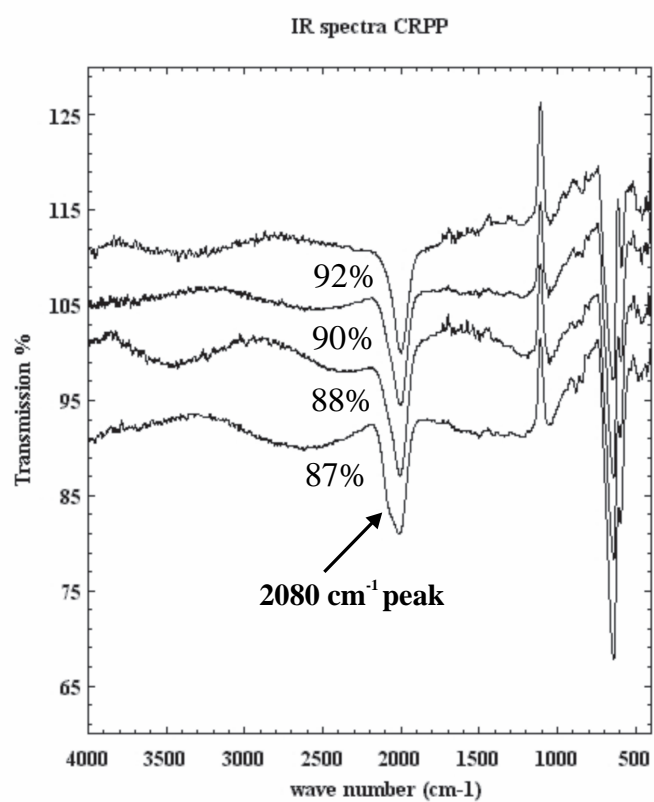
Figure 4.16: *I.R. sprectra for various density layer. The density was estimated by ellipsometry.*
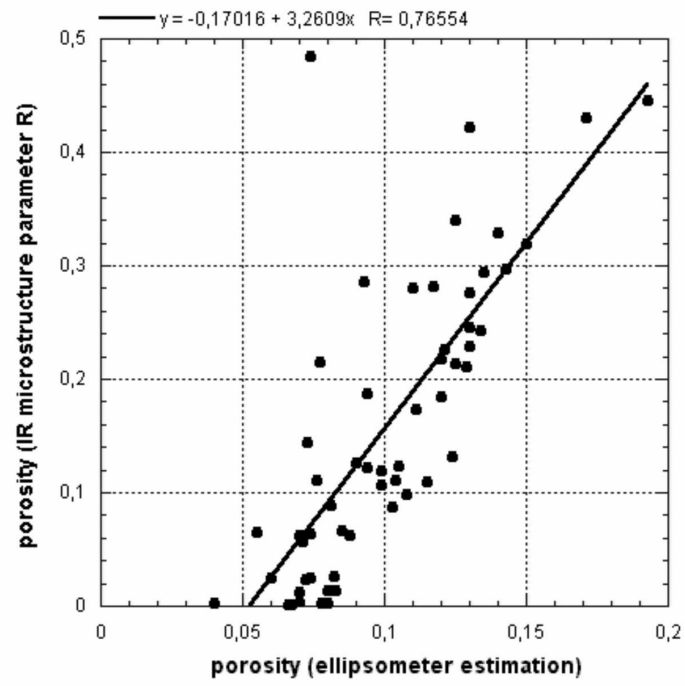
Figure 4.17: *micro structure parameter R function of ellipsometric porosity.*

Chapter 5

Small Gap reactor

The effect of the electrode gap variation on a-Si:H deposition has already been studied [37, 38] but mostly in small area plasma reactors. Unaxis industrial large area reactors have a standard electrode gap of about 2.4 cm. We have studied a-Si:H deposition in a small electrode gap (smaller than 2.4 cm), large area reactor. It appeared that in the small gap reactor, the deposition rate of a-Si:H layer increases but uniformity problems become more important.

5.1 Uniformity problems due to small gap reactor

For a first test, we used a aluminium plate, put on the ground electrode, to reduce the electrode gap in a non definitive way. Then we modified the industrial KAI-S reactor, by decreasing the height of the reactor walls to have a electrode gap of 1.7 cm, while keeping the electrode area at 57 cm × 47 cm.

5.1.1 Non uniformity, turtle shell effect

Before definitively modifying the reactor, we put a 8 mm thick aluminium plate in the standard reactor to reduce the gap to 1.5 cm. We measured the uniformity of the layer deposited on the plate with the global interferometry method (cf. section 2.2.3) by reflection. We observed the non uniformity of the layer which has a turtle shell appearance (cf. figure 5.1).
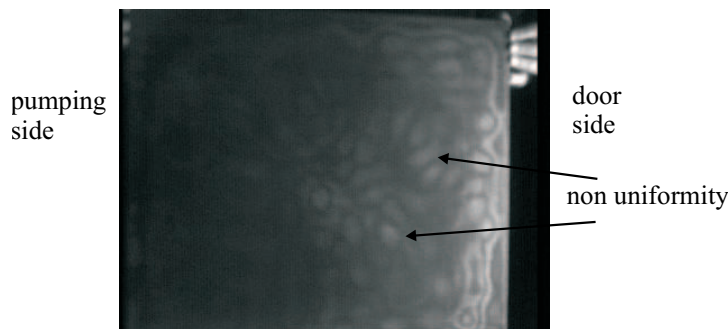

Figure 5.1: *Global Interference fringes of a-Si:H deposited on aluminium plate (effective electrode gap 1.7cm).*
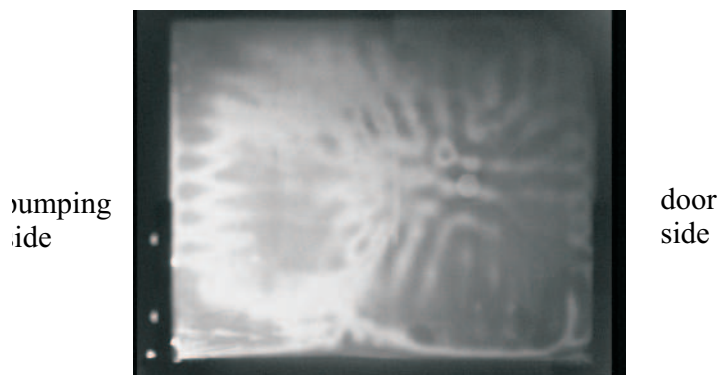
pumping
side

door
side

Figure 5.2: *Global Interference fringes of a-Si:H deposited on 1 mm glass substrate in small gap reactor, turtle shell effect.*

After modifying of the reactor walls, we again found this effect for particular process conditions when a-Si:H was deposited on 1 mm thick glass. On figure 5.2, we can see this turtle shell appearance combined with a more usual dome effect [2]. The a-Si:H layer of 0.5 μm was deposited at 13 Å/s (SiH$_4$ = 100 sccm, 0.8 mbar, 300 W, 27 MHz). The uniformity was measured to be +/- 10%.

We have targeted a process zone for which this effect may happen : high power and high deposition rate (10 Å/s, 300 W), low pressure (< 0.8 mbar), and hydrogen dilution.

This turtle shell effect is not well understood but it could be due to a non-uniform distribution of powder clouds in the reactor (cf. section 5.1.2). Such non-uniformities have not been observed in the standard gap reactor.

5.1.2   Non-uniformity due to the reactor edge and to powder

In the KAI-S reactor, the design of the RF connection and showerhead ensures the voltage and gas flow to be uniform. The pressure range, for all the electrode gaps and flow rates used, is high enough to ensure uniform gas pressure (cf. appendix A). The reactor is isothermal, therefore there is no thermophoresis effect, and we should expect uniform films. In the standard gap reactor, uniform films can be obtained over a large parameter space. For small gap reactor (1.7 cm), however we are obliged to work at high pressure to avoid the turtle shell effect. Moreover, uniformity problems due to edge effects and to powder limit even more the operational parameter space. It is important to solve these uniformity problems before studying deposition rate or layer properties, first for 1 mm glass and then for 3 mm glass. For a 3 mm thick glass substrate, the problem of the electrode-substrate transition adds a source of non-uniformity.

Edge non-uniformity

Siglo 2D simulations were performed to study the effect of the edge reactor design on plasma intensity. SIGLO 2D is a 2D fluid model of glow discharges in cylindrical geometries. It can be used for the simulation of RF glow discharges in conditions typical of plasma processing situations for low temperature plasmas. The configuration of the electrodes, dielectric and reactor walls is determined by the user. The output from this code includes current and voltage waveforms, power deposition profiles, mean energy, ionization rates, electron and ion densities and electric field distribution between the electrodes. SIGLO 2D comes with a data base including electron and ion transport
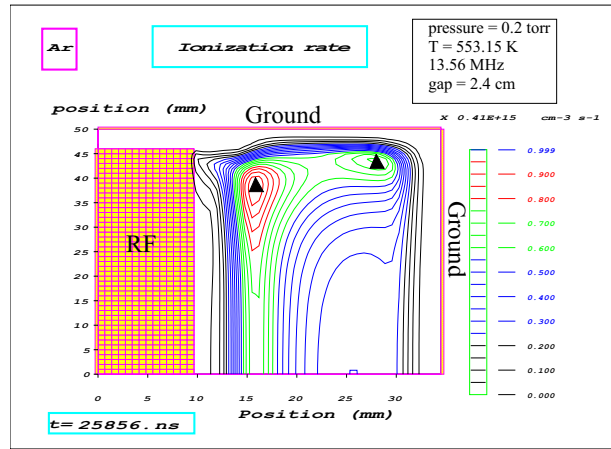
Figure 5.3: *Siglo2D simulation of plasma ionization rate for a standard edge geometry.*
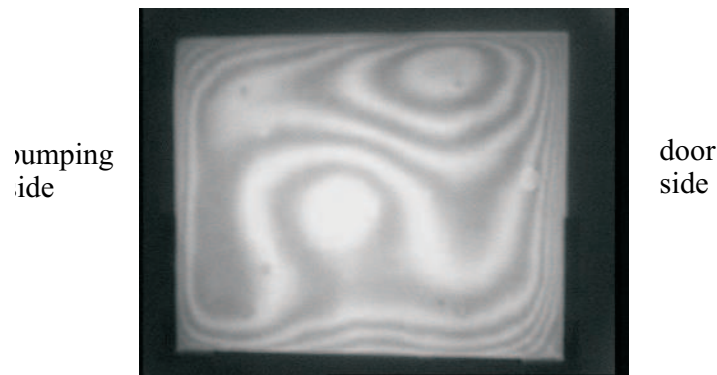
Figure 5.4: *Global Interference fringes of a-Si:H deposited on 1 mm glass substrate in small gap reactor, powder and edge effect.*

coefficients and rate data in 15 gases.

Simulations were done with argon. Figure 5.3 shows the plasma ionization rate, a good indication of plasma intensity, in a standard reactor edge geometry. It shows two zones of intense plasma in the corners due to the fringing fields, because of the proximity of RF and ground electrode. We can also suppose the formation of partial hollow cathodes, due to focussing effect of concave fields in corners. These effects are the direct consequence of an inadequate electrode design. Experimental experience also show the appearance of hollow cathode produced plasmas in confined space when working at 27.12 MHz at high pressure.

Locally intense plasma implies a higher silane depletion in this zone. Radicals do not diffuse far before depositing on surfaces. It results in a faster deposition rate at the edge and in gradients in silane concentration.

Powder effect

Even without edge and parasitic plasmas, dust formation seems to cause higher deposition rates at the edges. High power and high pressure uniform plasmas initially cause uniform powder production (polymerisation). But viscous drags reduces the gas flow at closed boundaries. Slower flow at the edges causes the powder to accumulate there. A higher concentration of powder at the edge leads to a positive feedback process
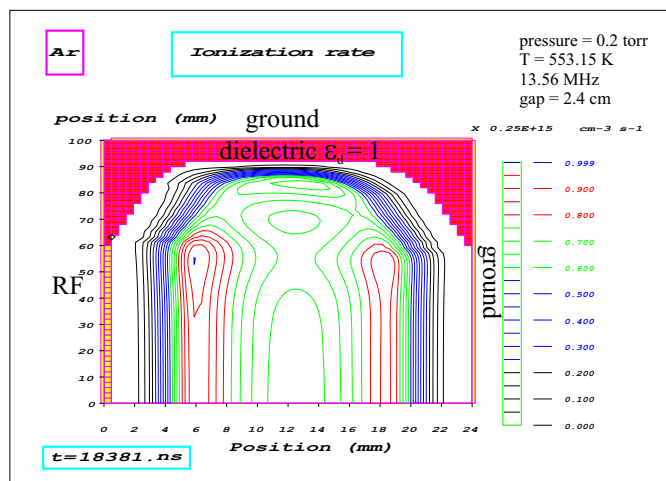
Figure 5.5: *Siglo2D simulation of plasma ionization rate for a new edge geometry, using dielectric material at the edge.*

which implies strong local power dissipation, faster deposition rate and powder formation. Once powder formation begins, the plasma resistivity increases which implies more power dissipation and more powder production [39]. Dust clouds will accumulate and fill any local potential traps. The fact of working in a small gap reactor increases the viscous drag effect and the problem of non-uniform powder distribution into the reactor.

We can see on figure 5.4 the uniformity of a 1 μm a-Si:H layer deposited on a 1 mm glass substrate. The layer was deposited at higher pressure of 1.3 mbar, 150 W to avoid the turtle shell effect (27.12 MHz). The layer is thicker around the glass edges. This is a good illustration of the powder and edge effect on layer uniformity in a small gap reactor.

Reduction of strong edge plasma and parasitic plasma

The solution is to reduce the focusing edge effect and to keep plasma away from confined spaces. Figure 5.5 shows the Siglo 2D simulated plasma ionization rate for a new reactor edge design. Hypothetical dielectric material ($\varepsilon_d = 1$) with a smooth concave shaping is used to attenuate the focus effect.

Experimentally, we used straight teflon bars (permittivity of 2.1 at 22°C) to distance the plasma from the edge region. Teflon was mounted along the reactor wall in the reactor length, not along the pumping side and the door side. We also filled in with teflon all confined spaces to avoid hollow cathodes (cf. figure 5.6).

We repeated the deposition conditions of figure 5.4 in the reactor equipped with the teflon jigsaw. We can see on figure 5.7 the uniformity measurement which is clearly an improvement on figure 5.4. The layer has a uniformity of about 5% which is acceptable. This solution works but is difficult to realize in an industrial environment.

Even if the edge problem is solved, we still have to deal with the powder formation if it is produced in the plasma bulk. Without modifying the pumping system we will always have to deal with the viscous drag at the edges. In fact we can divide our process condition locus in the small gap reactor into three sections (cf. figure 5.8). In the first section, there is no powder formation so, with the teflon jigsaw at the edges, we have a uniform deposition of the layer. In the third section, the powder is produced everywhere in the plasma. Because of the drag effects we have a non uniform powder distribution and deposition
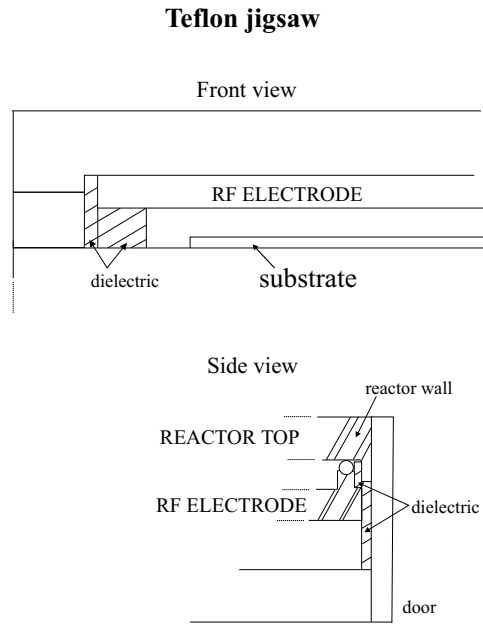
Teflon jigsaw

Figure 5.6: *Teflon jigsaw.*
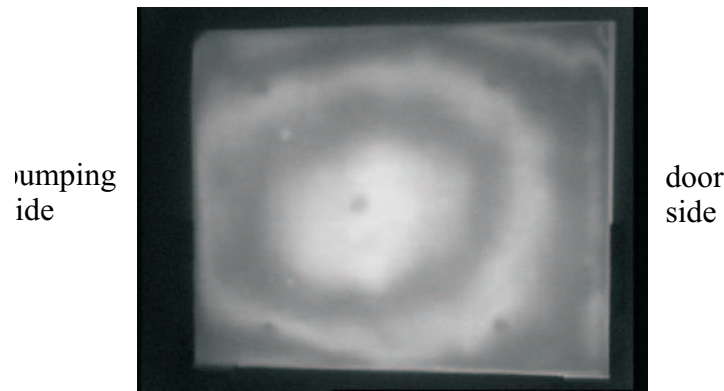
Figure 5.7: *Global Interference fringes of a-Si:H deposited on 1 mm glass substrate in the small gap reactor, teflon solution.*

of the layer. Even with the teflon jigsaw we will have a very bad layer uniformity. In the second intermediate section, powder is produced in intense plasma zones, at the edge or in small spaces. The teflon jigsaw has a beneficial effect and it widens the parameter space in the small gap reactor.

Until now, we have worked with 1 mm thickness glass substrate but solar cells are deposited on 3 mm thickness glass substrates. Besides the edge effects and the powder effects, a third source of non uniformity is added : the 3 mm transition between the ground electrode and the substrate surface. Moreover, in a small gap reactor, we must realize that there is only 1.4 cm gap between the RF electrode and the substrate surface. Figure 5.9 shows the uniformity measurement of 1 μm a-Si:H layer deposited on 3 mm glass substrate at 7 Å/s. The conditions were : SiH_4 = 128 sccm, 1.3 mbar, 150 W and 27.12 MHz. A teflon jigsaw was installed in the reactor. Interference fringes are visible along the substrate lengths from the door side to the pumping side. The lateral non-uniformity in figure 5.9 is therefore clearly due to the electrode-substrate transition.
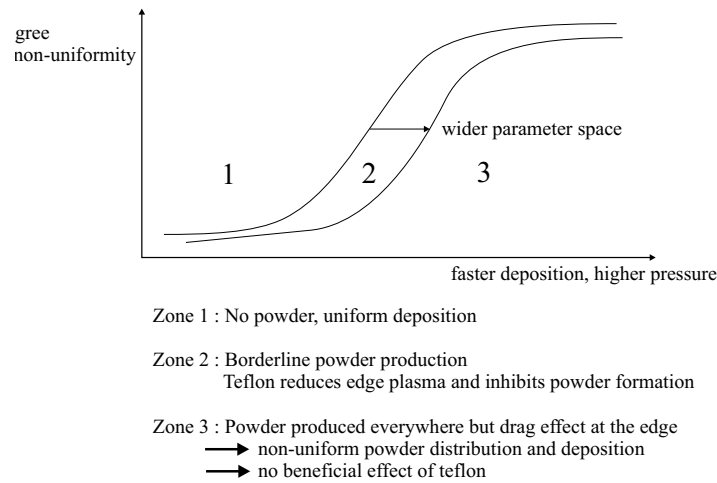
Figure 5.8: *Non uniformity zone function of plasma conditions.*

Figure 5.9: *Global Interference fringes of a-Si:H deposited on 3 mm glass substrate in small gap reactor, teflon solution.*

The most trivial way to solve this problem is to suppress the transition by surrounding the substrate with an aluminium frame of 3 mm thick which covers the ground electrode. Conditions of figure 5.9 were repeated, using the aluminium frame and the teflon jigsaw [7]. Uniformity measurement can be seen on figure 5.10. We obtained a very good layer uniformity with this system.

The small gap reactor presents uniformity problems which reduce the operation parameters space. It is possible to attenuate these non-uniformity problems by using a modified reactor design at the edge, which has been done in CRPP reactor thanks to a teflon jigsaw and aluminium frame at the reactor edge. It should be possible to go further in reactor design modifications, especially as regards the pumping system. At present, a new generation of KAI reactors uses a two side pumping system which improves the powder uniform distribution. The ideal would be to pump over the whole circumference (although the center region would be a stagnation zone) which would imply a new design of the reactor. Now that the uniformity problem can be solved by various methods, we can go on to consider the parameters of the deposited film.
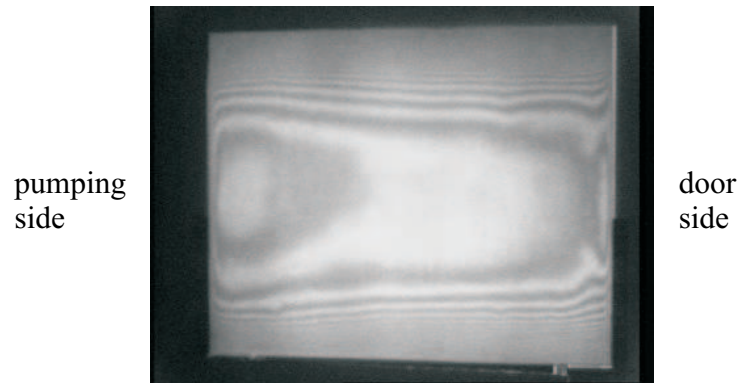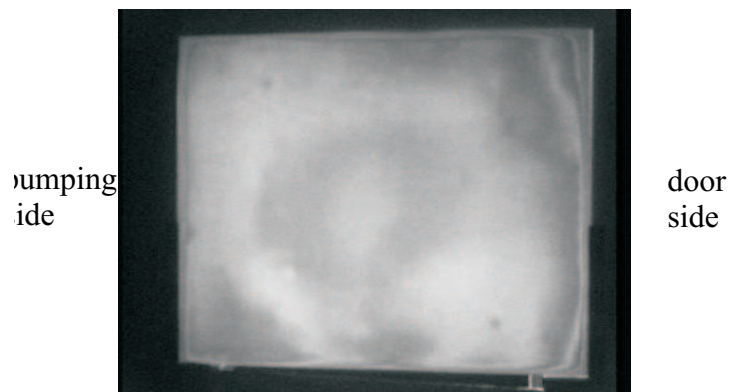
Figure 5.10: *Global Interference fringes of a-Si:H deposited on 3 mm glass substrate in small gap reactor, teflon and aluminium frame solution.*

5.2 Study of a-Si:H layer deposition rate

We have tested several plasma recipes for a-Si:H in the small gap reactor. Layer deposition rate and layer density were systematically measured. Results of layer density measurements will be presented in detail in the following chapter 6. We just mention here that, for the same deposition rate, the layer density is slightly better when deposited in small gap reactor. In this section we will discuss the effect of the small gap on the deposition rate.

5.2.1 Experimental results

Process was done at 13.56 MHz and 27.12 MHz. We worked at high pressure to avoid the turtle shell effect. No high hydrogen dilution was used. The deposition rate was measured by the in situ interferometer (cf. section 2.2.2). We can see on table 5.1, typical recipes used for a-Si:H with corresponding deposition rates.

temperature	RF	SiH$_4$	H$_2$	pressure	power	D.R.
°C	MHz	sccm	sccm	mbar	W	Å/s
200	13.56	100	0	0.8	150	8.1
200	27.12	100	0	1	150	9.5
200	27.12	150	0	0.8	150	7.8
200	27.12	128	128	1.3	150	3.8

Table 5.1: *Typical experimental conditions used in small gap reactor .*

If we compare our results with the literature [2,21,40] in a standard gap reactor, generally, we obtain faster deposition rates in the small gap reactor for 13.56 MHz and 27.12 MHz. The increase of deposition rate when electrode gap decreases has already been observed by Ross *et. al* [38]. Note that deposition rates in standard gap reactors increase with the frequency [13]. It would be interesting in the future to compare small gap deposition with high frequency deposition from the point of view of deposition rate, layer qualities. There are two possible explanations for faster deposition rate in small gap : the increase

of the electron temperature and the sheath coalescence. This will be explained in the following sections.

5.2.2   Effect of electrode gap on electron temperature, positive column theory

Theoretically, in DC glow discharges, the positive column maintains the level of ionization in the plasma against charge losses. The theory assumes that, first, the ionization is entirely due to electron collisions. Second, electron energy is gained from drift in the plasma electric field (ohmic heating). And third, charge loss is due to diffusion to the wall [1, 41]. Then, applied to a uniform RF plasma :

$$\text{volume ionization} = \text{charge losses to walls.}$$

Per unit area, for an electrode gap a, the previous assertion is :

$$n_e \langle \sigma \nu_e \rangle n_g . a \; = \; 2 n_e u_{Bohm} \tag{5.1}$$

where n_e and n_g are the electron and neutral gas density ; ν_e is the electron-neutral collision frequencies and σ is the electron-neutral cross section for ionisation. The Bohm velocity u_{Bohm} is given by :

$$u_{Bohm} \; = \; \sqrt{eT_e/m_i} \quad , \quad m_i = \text{ion mass} \tag{5.2}$$

Assuming the Boltzman distribution of electron energy [1] :

$$\langle \sigma \nu_e \rangle \; = \; \sigma_0 \sqrt{\frac{8eT_e}{\pi m_e}} . exp(\frac{-E_{ion}}{T_e}) \, , \tag{5.3}$$

Here, we suppose that $\langle \sigma \nu_e \rangle$ is uniform in the plasma bulk. We can write :

$$n_g a \; = \; \frac{2}{\sigma_0} \sqrt{\frac{\pi m_e}{8 m_i}} . exp(\frac{-E_{ion}}{T_e}) \, . \tag{5.4}$$

With the perfect gas law, pressure $p = n_g k T_g$ we can express T_e as a function of the pressure and the electrode gap :

$$pa \; = \; \frac{2kT_g}{\sigma_0} \sqrt{\frac{\pi m_e}{8 m_i}} . exp(\frac{-E_{ion}}{T_e}) \tag{5.5}$$

$$T_e \; = \; \frac{E_{ion}}{ln(K.pa)} \quad \text{where} \quad K = \frac{\sigma_0}{2kT_g} \sqrt{\frac{8 m_i}{\pi m_e}} \tag{5.6}$$

It means that for pa constant, T_e is constant, independently of plasma power or voltage. Therefore increasing the RF power should only increase the charge density for constant (pa). For a given pressure, reducing the electrode gap should increase the electron temperature. The simple physical reason is that there are fewer gas molecules for creating charge by electron collisions, but the charge loss rate is the same, therefore the ionization rate constant $\langle \sigma \nu_e \rangle$ must increase, necessitating an increase in T_e. This is what Maemura et al. calls a plasma self-organization mechanism [37]. If an increase in T_e means that proportionately more dissociation occurs per Watt of plasma power [42], then this could
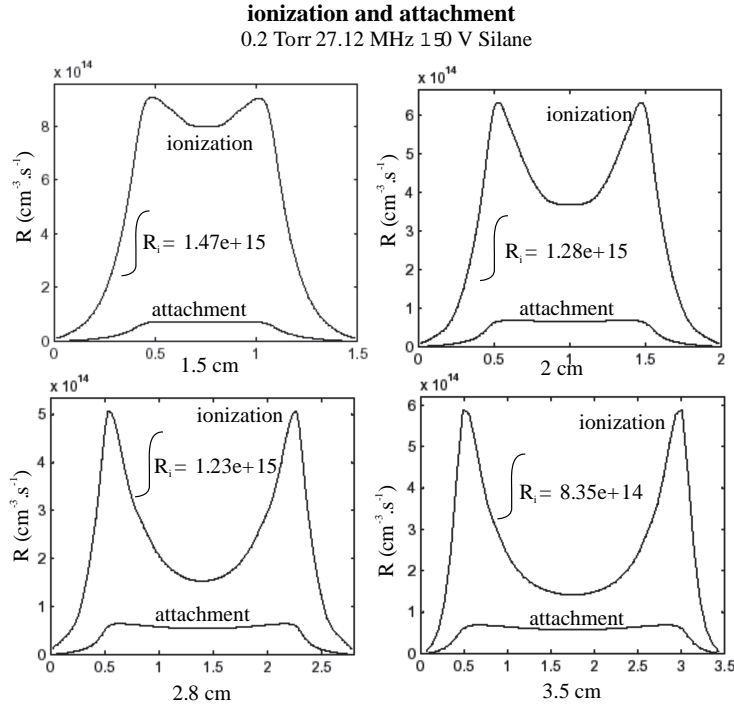
Figure 5.11: *Siglo 1D simulations : ionization profile and total ionization rate for various electrode gaps at 27.12 MHz.*

explain the higher growth rate observed with a small gap (17 mm) compared to standard gap (24 mm), for the same pressure, power and RF frequency.

Nevertheless this positive column theory presents some limitations. In the positive column theory, the deposition rate at 0.8 mbar in 1.7 cm gap reactor should be the same as the one at 0.57 mbar in 2.4 cm gap reactor. But experimentally, the deposition rate in the standard reactor doesn't improve strongly for this pressure. Therefore the positive column theory can't explain alone why deposition rate is faster in small gap reactor.

5.2.3   Sheath coalescence

If the electrons are also heated by stochastic heating, which is RF sheath phenomena, and (or) by wave-riding, then the assumption of electron ohmic heating by electric field in the bulk plasma volume must be revised. In the limit where RF sheath heating dominates, then the ionization source is proportional to the sheath area, just as for charge loss. So T_e will not depend on electrode gap until the gap become comparable to twice the sheath width, in case of sheath coalescence.

We have done Siglo 1D plasma simulations to see the influence of the electrode gap on the sheaths. Siglo 1D is a fluid model which does not consider stochastic effect or wave-riding heating but the fact that higher electric field in the sheath gives higher ionization rate at the sheath bulk transition (non-uniform $\langle \sigma \nu_e \rangle$). We can see on figure 5.11 the coalescence of the sheaths when the electrode gap decreases to 1.5 cm. At large gap, we have two ionization pics at the sheath-bulk transition. In the small gap, these two pics start to be superposed.

At the same time, the total ionization rate integrated along the electrode gap increases when the electrode gap decreases (cf. figure 5.12). Apparently sheath coalescence leads to an increase in the ionization rate which implies an increase in the deposition rate.

Total ionization rate vs. electrode gap
27 MHz 0.2 Torr 150 V silane
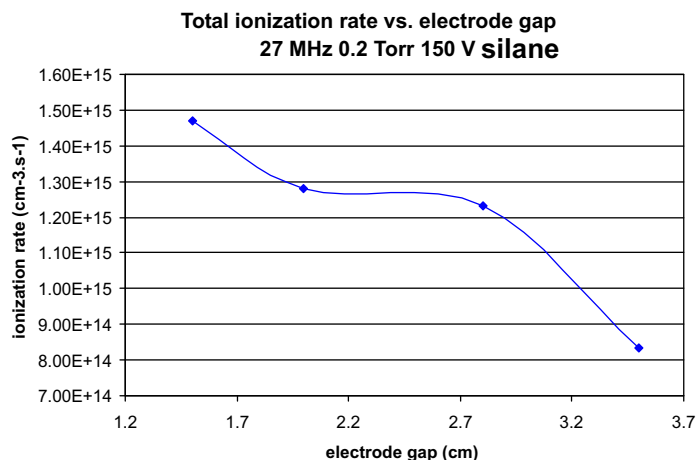
Figure 5.12: *Total ionization rate according to Siglo 1D function of the electrode gap at 27.12 MHz.*

Total ionization rate vs. Frequency
0.2 Torr 150 V silane
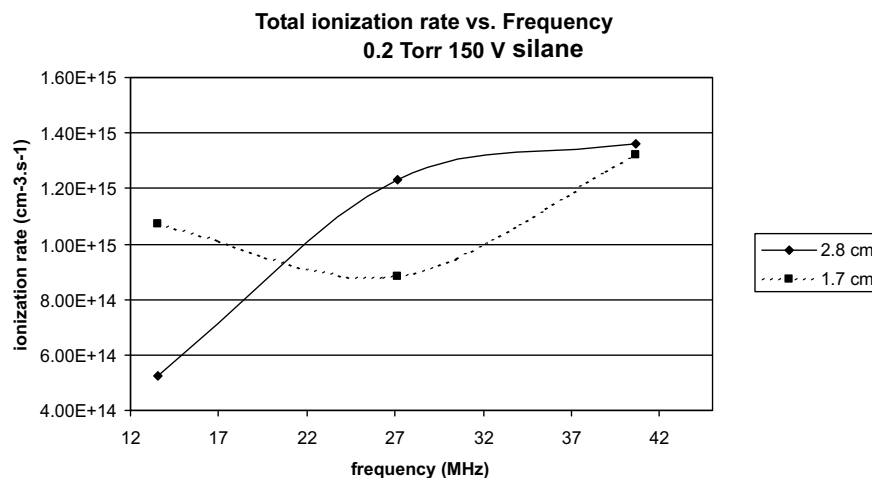
Figure 5.13: *Total ionization rate according to Siglo 1D function of the frequency.*

Figure 5.13 shows the influence of the plasma frequency on the ionization rate for a small electrode gap and a standard electrode gap according to Siglo 1D. It is interesting to see that the predicted ionization rate is the same for the small gap reactor and the standard gap reactor at 40.68 MHz, possibly because the sheaths are thinner at higher frequencies, thereby reducing sheath coalescence even at 1.5 cm gap.

Seeing the interesting influence of small gap reactor on the deposition rate and layer density (cf. section 6), it should be interesting to continue this study, particularly regarding the comparison between small gap and high frequency. Nevertheless, the small gap reactor presents problems of mechanical loading of the substrate if the standard loadlock fork is used.

Chapter 6

Study of a-Si:H layer density

6.1 Influence of deposition rate on a-Si:H layer density

6.1.1 General tendency

At the beginning, our aim was to study high deposition rate of amorphous silicon, by appropriate plasma conditions and reactor design. Deposition rates presently used in commercial cell manufacturing are around 1-2 Å/s. We have easily reached high deposition rates (13 Å/s) in the small gap reactor (cf. section 5.2.1), but systematic measurements of layer density by the ellipsometric method (cf. section 4.2) have shown that it decreases when the deposition rate increases for a standard process temperature of 200°C. Figure 6.1 compiles the layer density measurements as a function of deposition rate in a small gap reactor and standard gap reactor for various pressures, SiH_4/H_2 mixtures and RF powers.
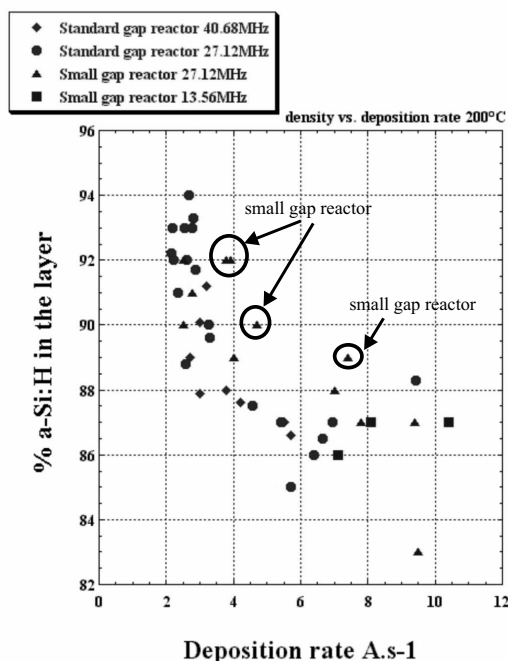

Figure 6.1: *Layer density as a function of deposition rate.*

Generally we observe a strong decrease of layer density from 94% to 87% when the deposition rate increases from 2 Å/s to 5 Å/s, independently of reactor design and process parameters (pressure, SiH_4:H_2 mixture, power).

The film properties, the microstructure, density and surface roughness, affect significantly the performance of electronic devices [43]. Nevertheless the density of the amorphous silicon layer is a delicate subject for solar cells. Generally, a dense a-Si:H intrinsic layer is necessary for a good quality cell. But other parameters influence cell performance such as layer interfaces, p-layer and n-layer properties, and boron cross-contamination. Nevertheless, in this study, our aim is to reach high layer density at high deposition rate and to understand the physical mechanisms. We have explored the parameter space to find the higher deposition rate we can reach without degrading the layer density : temperature, pressure, dilution, frequency and electrode gap. In fact, we can see on figure 6.1 interesting conditions which give better layer densities than others, especially for the small gap reactor at 27.12 MHz. We also present in the following section some physical explanations for the effect of deposition rate on layer density.

6.1.2   Layer growth phenomena at high deposition rate

Figure 6.2 shows some phenomena involved in a-Si:H growth. We can define three steps in film growth phenomena [44]. First, radicals are created and reach the substrate. Second, radicals adsorb on the surface of the substrate, diffuse over this surface and finally react on the surface, which implies their incorporation into the film or their release from the surface. Third, atoms diffuse in the bulk and bulk chemistry occurs.
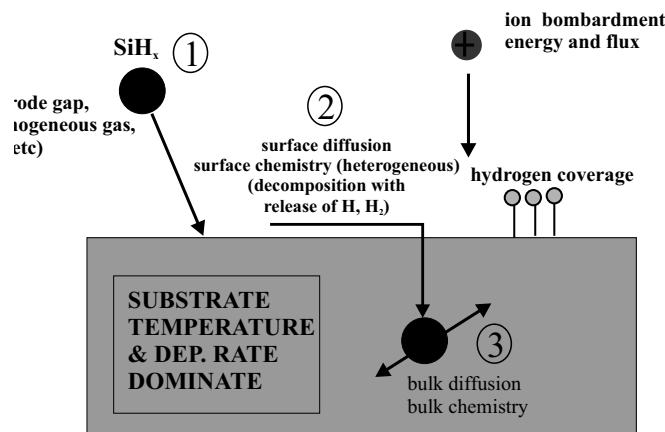
Figure 6.2: *Phenomena involved in determining a-Si:H density .*

Two phenomena appear to be particularly important for layer density : the nature of silane radicals reaching the surface and radical diffusion.

Radical contribution to growth

Porosity at high deposition rate, generally by increasing the power, may be due to a higher proportion of SiH_2 radicals contributing to the film growth. Gallagher has shown that SiH_3 radicals produce at least 98% of the Si deposit for typical deposition conditions. But as power and gas flow increase (generally conditions for high deposition rates), the probability for SiH_2 radicals to reach the surface is enhanced [45]. This is

a)

b)
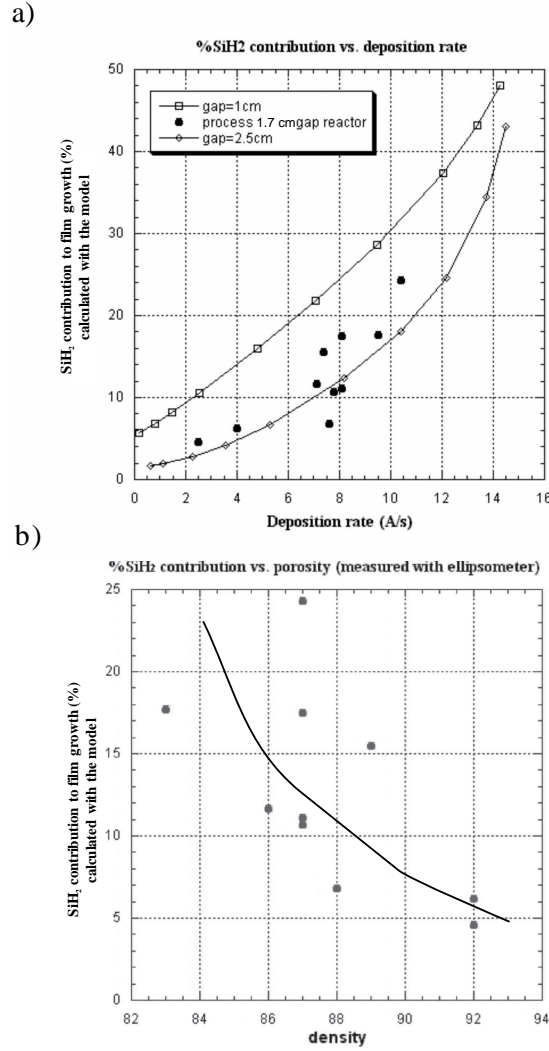
Figure 6.3: *a) Model SiH$_2$ contribution as a function of deposition rate. Solid curves are simulations and dots represent real conditions in small gap reactor for which SiH$_2$ contribution was estimated with the model. b) Model estimated SiH$_2$ contribution as a function of layer density for the previous real conditions, solid curve is a tendency curve.*

probably responsible for a transition from a low sticking coefficient (SiH$_3$) deposition, which produces high-quality film, to high sticking coefficient (SiH$_2$), which produces low-quality films. SiH$_2$ reactive radicals tend to attach wherever they impact. With no diffusion, ballistic-like deposition leads to a physical-vapour-deposition-like film growth, with a poor step coverage, rough surface and columnar structure [7, 46, 47]. This ballistic deposition type coupled with an overshadowing effect causes void formation as film deposition progresses [43]. SiH$_3$ is a low reactive radical, very mobile so it diffuses on the surface and fills surface valleys. It lead to CVD-like film growth with conformal step coverage, smooth surface and dense material [43, 46, 48].

We used a one-dimensional model of gas flow and chemistry in the plasma to simulate the SiH$_2$ contribution for plasma conditions in our KAI-S reactor. In this model, we solve the diffusion continuity equation for the neutral species in the inter electrode gap space. The input flux is introduced as a volumetric source for the corresponding species and the

pumping is introduced as a loss term :

$$\nabla.\vec{J_i} = \phi_i - aC_i + R_i \qquad (6.1)$$

where J_i is the diffusion flux, ϕ_i the input flux/volume, a the pumping speed, C_i the specie concentration and R_i the chemical reaction. For a-Si:H deposition, we consider 6 species (SiH_4, SiH_3, SiH_2, H_2, H and SiH_6) and 10 gas phase reactions (cf. table 6.1) [49,50].

Reaction	Rate coefficient ($cm^{-3}.s^{-1}$)
$SiH_4 + e \rightarrow SiH_3 + H$	$8.4.10^{-11}$
$SiH_4 + e \rightarrow SiH_2 + 2H$	$1.1.10^{-10}$
$H_2 + e \rightarrow H + H$	$4.49.10^{-12}$
$Si_2H_6 \rightarrow 2SiH_3$	$4.75.10^{-10}$
$H + SiH_4 \rightarrow SiH_3 + H_2$	$2.8.10^{-11} \exp(-1250/T)$
$H + SiH_3 \rightarrow SiH_2 + H_2$	$5.0.10^{-10}$
$H_2 + SiH_2 \rightarrow SiH_4$	$2.0.10^{-13}$
$SiH_4 + SiH_2 \rightarrow Si_2H_6$	$1.0.10^{-11}$
$SiH_3 + SiH_3 \rightarrow SiH_4 + SiH_2$	$7.0.10^{-12}$
$SiH_3 + SiH_3 \rightarrow Si_2H_6$	$1.0.10^{-11}$

Table 6.1: *Summary of reaction kinetics used in the model. T is the gas temperature. Data from L. Sansonnens's private communication.*

The resolution of the model was done using Matlab. The input parameters are gap distance, pressure, flow rate, electron density n_e and temperature T_e. The output parameters are the concentration of the species in the plasma, the silane depletion, the deposition rate and the SiH_2 contribution to film growth.

Figure 6.3 (a) represents the model SiH_2 contribution to film growth as a function of the deposition rate for various input conditions. With the model, we also estimated the SiH_2 contribution for real conditions (cf. black dots on 6.3 (a)) by adjusting n_e so that the calculated and real deposition rates are the same. Figure 6.3 (a) shows that the SiH_2 contribution increases when the deposition rate increases for both a 2 cm gap reactor and a 1 cm gap reactor (same pressure, flowrates and T_e). In the standard gap reactor, SiH_2 contribution is lower because SiH_2 reacts with SiH_4 in the gas phase more than in the small gap reactor since it has more time to diffuse. Nevertheless, if the pressure in the small gap reactor is higher then the one in the standard gap reactor, SiH_2 contribution will be lower in the small gap reactor also.

Figure 6.3(b) shows the calculated SiH_2 contribution for real conditions as a function of measured layer density. The SiH_2 contribution has the tendency to decrease when the density increases which is also consistent with Gallagher and Tsai's observations and model [43].

Surface diffusion

Besides the radical type implied in layer growth, surface mobility and reaction time also influence layer density (cf. figure 6.2). The importance of surface diffusion was recognized since model and experiments have shown that conditions of low radical surface diffusion lead to a high void fraction volume in the bulk and a columnar growth [44,51]. For a given substrate temperature, an increase of the deposition rate (generally by increasing

the power) will limit radical diffusion and surface reactions [52] since new radicals will arrive on top of the layer and bury the radicals before they have time to diffuse across the surface. One way to compensate this effect is to increase the temperature. Using a Maxwell-Boltzman distribution of radical speed and energy, it appears that the rate of surface diffusion and the diffusion length increases exponentially with temperature [51]. According to Collins *et al.*, a shorter diffusion length of film radicals on the film surface and a poor layer properties is due to low substrate temperature ($< 250°$C) [53]. Experimentally, it has been found that substrate temperature is the key parameter for the film growth [44, 53–55]. According to Ross *et al.*, 230°C is the optimal temperature for solar cell performance and pressure, power, electrode gap can be chosen arbitrarily, provided that there is no plasma polymerization [38]. Other workers have found that the optimum growth temperature of a-Si:H for electronic applications was between 250°C and 300°C [56].

To conclude, the solid state physics determined by the substrate temperature is probably the determinant factor for dense film growth, whereas plasma phase conditions, such as pressure, gas mixture and frequency, have relatively little effect on layer density [52, 54]. In the next section, we attempt to improve the layer density at high deposition rate. As discussed above, it experimentally appears that substrate temperature has a great effect on layer density.

6.2 Attempts to improve the layer density at high deposition rate

6.2.1 Small gap reactor

The circled data on figure 6.1 indicates layers deposited in the small gap reactor at 27.12 MHz. Generally, the layer density is better compared to the density of layers deposited in the standard gap reactor. This is coherent with theoretical results about SiH_2 contribution in layer growth (cf. section 6.1.2) since the SiH_2 contribution is lower for the high pressure process in the small gap reactor.

6.2.2 High pressure, high hydrogen dilution

Good cells (initial efficiencies of 7.1% to 11.1%) were achieved with a deposition rate of 7 Å/s, using high pressure and high H_2 dilution [57]. At a given RF power, increasing the pressure reduces the average ion impact energy and favours high mobility radicals such as SiH_3 [7]. According to Rech *et al.* a high deposition pressure and dilution is found to be the key parameter to achieve high efficiencies (for a-Si:H and μc-Si:H) at high growth rates. Table 6.2 shows Rech's deposition conditions and the equivalent ones for application in KAI-S reactor, scaled-up by the electrode area ratio.

The equivalent hydrogen flow for KAI-S reactor is large, 10sLm. The maximum flow we can use is 500 sccm and, because of a Plasma Box^{TM} leak, the maximum pressure we can reach in the reactor is 2 mbar. We tested various silane dilutions, keeping the hydrogen flow at 500 sccm. We regulated the plasma power (at 40.68 MHz) to have a deposition rate between 2.7 Å/s and 4 Å/s. Each time, the layer density was measured (cf. figure 6.4). We can see a optimum silane percentage of 35%, which gives a density layer of 91.5% at 3 Å/s. Above 50% of silane, there is a lot of powder, the deposition rate decreases

	Rech typical recipe (μc-Si:H) [57]	For application in KAI-S (electrode area ratio)
electrode area	150 cm^2	2475 cm^2
silane	6 sccm	100 sccm
hydrogen	600 sccm	10000 sccm
pressure	7 torr	7 torr
power (13.56 MHz)	40-80 W	660-1320W

Table 6.2: *Experimental conditions used by Rech for high pressure high H_2 dilution process and corresponding conditions for application in a KAI-S reactor.*
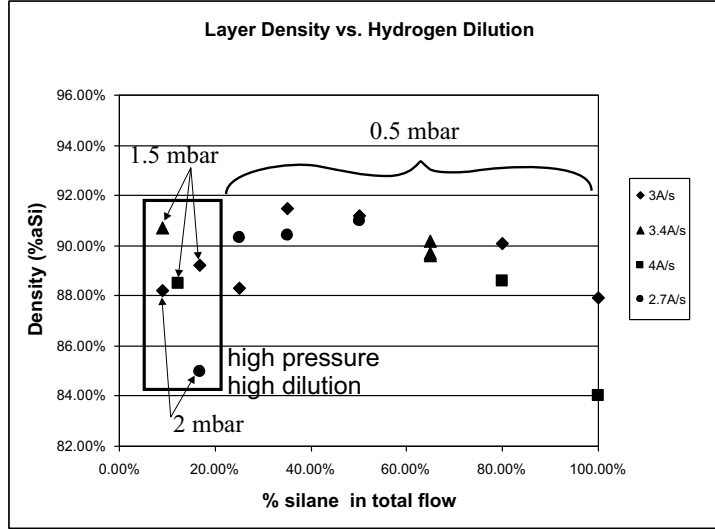

Figure 6.4: *Layer density as a function of the percentage of silane in the total SiH_4 plus H_2 flow.*

during the process and the layer density degrades. For high pressure and high dilution (cf. data in rectangle on figure 6.4), there is no great improvement of the density layer. Nevertheless, these first tests are encouraging as we can reach a layer density of 90.7% at 3.4 Å/s.

6.2.3   Comparison between 27.12 MHz and 40.68 MHz

An increase in excitation frequency presents several advantages : higher ion density and higher ion flux bombardment with lower ion energy at the substrate [36]. Moreover, a reduction of electron attachment and negative ion formation reduces the powder formation [7]. It implies high deposition rates, reduced layer stress and layer defects due to powder [58, 59]. We have reproduced the same conditions of flows and pressure respectively at 27.12 MHz and 40.68 MHz. The input power was adjusted to have the same plasma power (50 W) for each frequency as described in section 2.2.1. The deposition rate was measured each time and table 6.3 presents the results.   Concerning the deposition rate, there is no clear difference between 27.12 MHz and 40.68 MHz. Figure 6.5 shows the evolution of the deposition rate as a function of excitation frequency [62]. Working in small plasma reactors Curtins *et al.*, Heintze *et al.* and Howling *et al.* have observed a effect of frequency on deposition rate from 27 MHz. But Sansonnens *et al.*, who worked
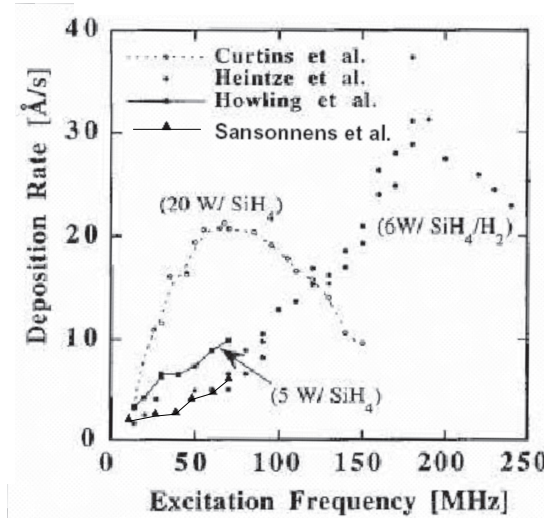
Figure 6.5: *Deposition rate as a function of excitation frequency. Data from Curtins et al., Howling et al., Heintze et al. and Sansonnens et al. [2, 13, 60, 61].*

	27.12 MHz	40.68 MHz
Standard $SiH_4/H_2 = 160/40$ sccm pressure = 0.5 mbar	3.8 Å/s	4.1 Å/s
Pure Silane $SiH_4 = 160$ sccm pressure = 0.5 mbar	5.2 Å/s	4.6 Å/s
Low pressure $SiH_4/H_2 = 160/40$ sccm pressure = 0.2 mbar	2.4 Å/s	2.6 Å/s

Table 6.3: *Comparison of deposition rate at 27.12 MHz and 40.68 MHz.*

in the same KAI-S reactor as this thesis work, saw only a small increase in deposition rate till 50 MHz. So it appears that 40.68 MHz is not a high enough to observe a strong increase in deposition rate in the larger reactor, for reasons not understood presently.
Figure 6.6 shows the layer density as a function of deposition rate, only for layers deposited in the standard gap reactor at 27.12 MHz and 40.68 MHz. We observe no striking difference between frequencies.

6.2.4 Process Temperature

Until now, we have always worked at 200°C. We have tested higher process temperatures from 220 °C to 280°C in the standard gap reactor, using the same pressure, gas flush, power and frequency : pressure/SiH_4/H_2/power/frequency = 0.5 mbar/160 sccm/40 sccm/ 80W/27 MHz. For each layer, the deposition rate and density were measured and added to the graph of density vs. deposition rate on figure 6.7.
Up to 230°C, the increase in layer density is important, from 86% to 90% for a deposition rate of 6 Å/s, which is a high rate compared to that used in industry.
Even though a-Si:H layer density improves above 230°C, this increase in process temperature would imply other problems for solar cell performance. A possible increase in boron diffusion at the p-i layer interface could be significant at high process temperature.

Specifically, the solar cell V_{oc} decreases when temperature process increases [55, 63] due to the lower H-content. Presently, the process temperature in industry remains at 200°C.

It is no surprise that a temperature increase has a striking effect on layer density. It was explained in section 6.1.2 that increasing the temperature should increase radical diffusion rates. It shows that the effect of deposition rate on layer density is especially a surface effect, depending on substrate temperature and, to some extent, on radical type reaching the surface.

Actually, industrial constraints impose a process temperature below 200°C and a standard gap reactor (because of the substrate loading difficulties in a small gap reactor). So our parameter space for the optimization of an high deposition rate, good quality, a-Si:H layer was narrow. We finally established a standard recipe at 200°C, 40.68 MHz, $SiH_4/H_2 = 160/40$ sccm, 60W, 0.5 mbar. For this recipe, deposition rate is 3 Å/s and density, 90%. To conclude, at the Institute of Microtechnology of Neuchâtel, solar cells were deposited in a KAI-S reactor. They deposited a-Si:H intrinsic layer at 3 Å/s, 200°C, 40.68 MHz, $SiH_4/H_2 = 105/45$ sccm, 60W, 0.3 mbar, conditions similar to our standard ones. With an appropriate treatment for boron cross-contamination in a single chamber process (cf. chapter 8), the cell performances met industry specifications. The full process for solar cell manufacture will be established in the RWE Schott Solar plant, using the single chamber reactor from UNAXIS (Plasma Box^{TM} system) starting from the 3 Å/s recipe for a-Si:H intrinsic layer.
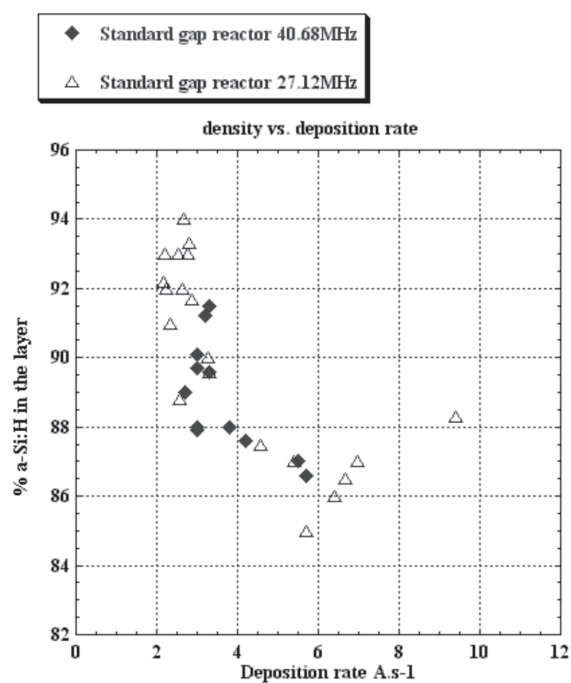
Figure 6.6: *Layer density function of deposition rate in standard gap reactor at 27.12 MHz and 40.68 MHz.*
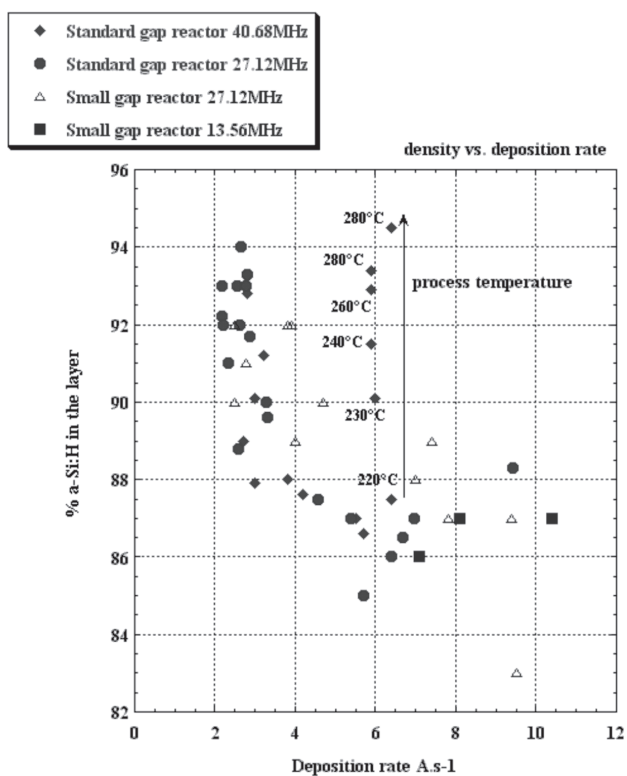

Figure 6.7: *Layer density function of deposition rate for different temperatures.*

Chapter 7

Consequences of non-uniform RF plasma potential in large-area capacitive reactors

With no standing wave effect, people see the large area reactor as an uniform central part and a non-uniform edge due to fringing field (cf. chapter 5). What we show in this chapter is that the edge non-uniformity can propagate inside the reactor over a long range, due to finite plasma conductivity. Therefore, the edge perturbation is not only a fringing field problem but a propagation problem. A perturbation in RF plasma potential, due to electrode edge asymmetry or the boundary of a dielectric substrate, propagates along the resistive plasma between capacitive sheaths. This chapter consists of a theoretical and an experimental section. In the first part, we develop a model based on a telegraph equation to show how the plasma potential is affected in large area reactors. Perturbations in potentials and currents due to the edge effects of the electrodes will be demonstrated by means of a simple analytical model assuming sinusoidal plasma potential and Langmuir-Hertz sheaths. In the second part we present measurements of the DC current and potential using an array of Langmuir probes in the ground electrode of two large area reactors, one cylindrical and the other rectangular. These measurements are used to test some predictions of the telegraph model.

7.1 The telegraph equation applied to large area reactors

The non-uniformity considered here is due to perturbations in RF potential in the vicinity of the edges of electrodes and dielectric substrates. Many other phenomena can give rise to non-uniform deposition or etching in RF parallel plate reactors, including imperfect contact of substrate with the electrode [64], inappropriate gas flow distribution [65], clouds of dust particles [39], and finite wavelength effects associated with high frequency in large reactors [48,66–68]. In this work the RF frequency (40.68MHz) is low enough such that a quarter RF wavelength is much longer than the reactor dimensions. Therefore we need consider only the edge effects.

At the edge of the RF plasma reactor represented in figure 7.1, the electrode areas are asymmetric because of the sidewall. In order to preserve RF current continuity, the RF sheath voltage at the larger area electrode will locally be less than the RF sheath voltage
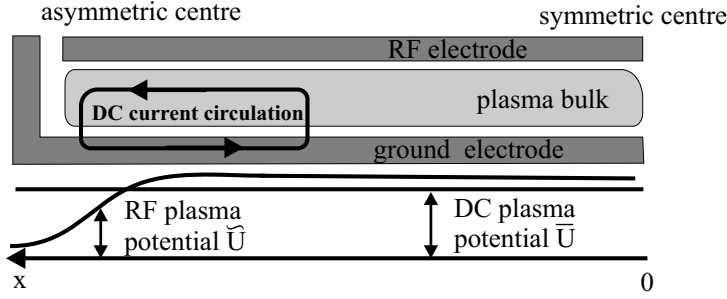
Figure 7.1: *Schematic cross-section of an asymmetric reactor, from the left hand sidewall to the center, showing profiles of the RF and DC components of the plasma potential, and the circulation of DC current between the ground electrode and the plasma.*
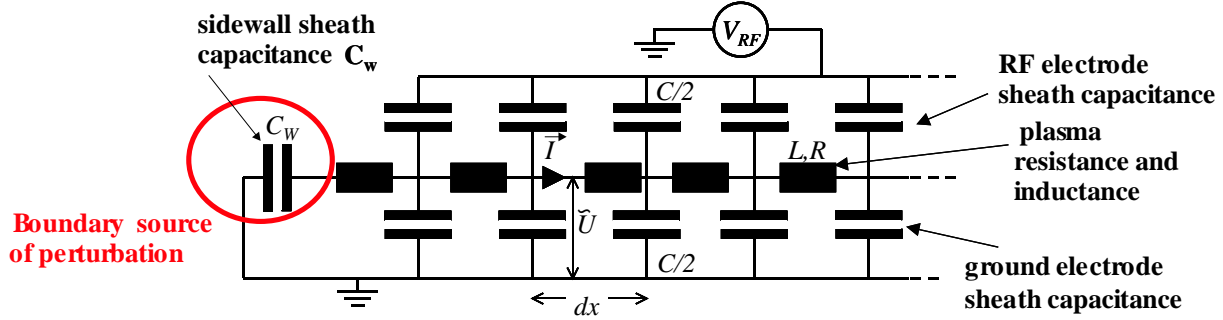

Figure 7.2: *The equivalent circuit used for the telegraph description, the sidewall sheath capacitance is represented by C_W.*

at the smaller electrode, the sum of the potentials being equal to the applied RF voltage. In the middle of the reactor, however, the electrode areas are symmetric and both RF sheath voltages would be expected to equal half of the applied RF voltage V_{RF}.

The different sheath potentials in these two zones can be reconciled by allowing the RF plasma potential to vary across the reactor with a characteristic damping length λ due to the non-zero plasma resistivity [69]. We introduce the lateral plasma impedance via the plasma resistance R and inductance L. The plasma resistance and inductance values are averaged over the bulk plasma height. In the absence of any dielectric substrate, RF sheath capacitance and ground sheath capacitance are equal to $C/2$ (capacitance per unit length). The ground sheath potential for a symmetric discharge would be:

$$\tilde{U}(x,t) \;=\; \frac{V_{RF}.C/2}{C/2+C/2}.e^{i\omega t} \;=\; \frac{V_{RF}}{2}.e^{i\omega t} \tag{7.1}$$

The boundary source of perturbation, the wall, is represented by a capacitance C_W. In the presence of this perturbation, we can consider a lateral voltage perturbation $\underline{V}(x,t)$ which propagates along the plasma. The ground sheath RF potential becomes :

$$\tilde{U}(x,t) \;=\; \frac{V_{RF}}{2}.e^{i\omega t} \;+\; \underline{V}(x,t) \tag{7.2}$$

The redistribution of the sidewall RF current is represented by a lateral RF current $\vec{I}(x,t)$ in the simplified 1D equivalent circuit model in figure 7.2. The lateral current $\vec{I}(x,t)$ flows through R and L, the plasma resistance and inductance per unit length, where :

$$\nabla \underline{V} \;=\; -R\vec{I} - L\frac{\partial \vec{I}}{\partial t} \tag{7.3}$$

and current continuity requires:

$$\nabla.\vec{I} = -C\frac{\partial V}{\partial t} \tag{7.4}$$

We therefore obtain :

$$\frac{\partial^2 V}{\partial x^2} = LC\frac{\partial^2 V}{\partial t^2} + RC\frac{\partial V}{\partial t} \tag{7.5}$$

which is the telegraph equation. Note that only the RF plasma potential is non-uniform. The DC plasma potential is considered as uniform because of the high plasma DC conductivity. With a first order approximation, the sheath widths a, and therefore C are also uniform over all the reactor. The damping dominates if $R/\omega L = \nu_m/\omega \gg 1$ (ν_m electron-neutral collision frequency) for high pressure and low excitation frequency. In 1D cartesian coordinates, with $V(x,t) = V(x)e^{i\omega t}$, the particular solution is :

$$V(x,t) = \underline{B}exp(\frac{\pm x}{\underline{\lambda}})e^{i\omega t} = \underline{B}e^{\pm x/\lambda}e^{i(\omega t \pm x/\lambda)} \tag{7.6}$$

where

$$\underline{\lambda} = \frac{\lambda}{(1+j)} \quad \text{and} \quad \lambda = \sqrt{\frac{2}{\omega RC}} = \omega_{pe}\sqrt{\frac{ag}{\omega\nu_m}} \tag{7.7}$$

with a the sheath width, g the plasma bulk height, ν_m the electron-neutral collision frequency, and ω_{pe} the electron plasma frequency. The voltage perturbation is a strongly-damped wave ; the value of λ increases with electron density, sheath thickness and bulk plasma height, and decreases with higher excitation frequency and collision frequency (higher pressure). If inductance is included, the damping length increases and the wavelength decreases. The boundary condition at the sidewall is :

$$\frac{\partial \tilde{\underline{U}}}{\partial x}|_{x=L} = -I_{sidewall}R = -\tilde{\underline{U}}(L)j\omega C_W R \tag{7.8}$$

where C_W is the sheath capacitance at the sidewall (cf. figure 7.2).
Note that this simple model makes several assumptions, such as constant sheath width, uniform plasma density and temperature. The 1D approximation treats the plasma as a sheet with no vertical structure, with no allowance for charge screening and diffusion in the vicinity of discontinuities in sheath potential. The RF plasma potential is the same as the ground sheath RF voltage in this simple model where the transverse (vertical) impedance of the bulk plasma is neglected compared to the sheath impedance. Comparison between this solution and a numerical solution of Maxwell's equations for the voltage distribution in a lossy dielectric shows that the telegraph model is a good approximation. Figure 7.3 shows the estimated value for the telegraph equation damping length (for hydrogen). The combination of a reduced and augmented sheath potential at the asymmetric edge results in a net increased power deposition at the edge. We usually work around $0.4/1.6$ mbar and 10^{10} cm^{-3} which gives a damping length around 5 cm to 10 cm. In the KAI-S reactor, the gap between substrate and the reactor edge is 5 cm. If λ is more than 5 cm, the RF plasma potential non-uniformity will extend within the edge of the substrate, which will imply a non-uniform deposition rate on the substrate.
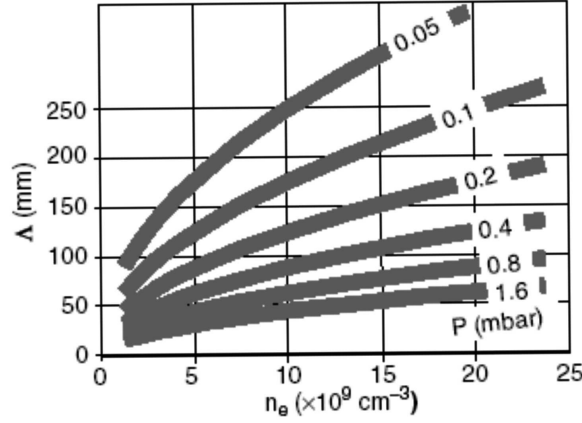
Figure 7.3: *Estimated values for the telegraph equation damping length (for hydrogen) [69].*

7.2   Consequences of non-uniform RF plasma potential

7.2.1   Local non ambipolarity

Since the DC plasma potential is uniform across the plasma, and a conducting electrode is an equipotential surface (in absence of a dielectric substrate), a consequence of the non-uniform RF plasma potential is that local ambipolarity cannot be satisfied over all the electrode surface. This is because the RF and DC sheath voltages, $\tilde{U}$ and $\bar{U}$ respectively, cannot everywhere simultaneously satisfy the self-rectification condition [70] for zero average current flow to the surface, which is :

$$\bar{U} = \frac{T_e}{2}ln(\frac{M_i}{2.3m_e}) + T_e ln[I_0(\frac{\tilde{U}(x)}{T_e})] \tag{7.9}$$

A sinusoidal plasma potential, and therefore sinusoidal sheath voltages, have been assumed for the sake of convenience in this simplified model. Any spatial variation in the plasma RF potential will necessarily lead to time-averaged current flow across the sheaths. However, the reactor is capacitively coupled which prevents any DC current in the external circuit. Therefore, any DC current which flows across the sheaths must circulate through the plasma and return via the conducting surface of the electrode, so that the integral of the DC current over the electrode area is zero. The DC plasma potential adjusts to satisfy this condition at the ground electrode, and the self-bias of the RF electrode adjusts to satisfy this condition at the RF electrode. Consequently, the reactor asymmetry drives DC current circulated within the reactor as shown in figure 7.1.

These DC sheath currents can be measured with grounded probes in the ground electrode surface, as shown in the following sections. These probes measure the local DC current density to the ground electrode. The DC floating potential of the surface probes can also be used to give an indirect indication of the spatial variation of the plasma RF potential amplitude. In the previous equation 7.9, where the plasma potential is not equal to the

value necessary for local ambipolarity, a floating probe in the electrode surface will have the time-averaged voltage:

$$\bar{V}_f(\underline{x}) = \bar{U} - \frac{T_e}{2}ln(\frac{M_i}{2.3m_e}) + T_e ln[I_0(\frac{\tilde{U}(\underline{x})}{T_e})] \neq 0 \qquad (7.10)$$

because the grounded surface is not floating.
In the limit $\tilde{U}(\underline{x}) \gg T_e$, we can write :

$$\bar{V}_f(\underline{x}) = \bar{U} - \tilde{U}(\underline{x}) + \frac{T_e}{2}ln[2\pi(\frac{\tilde{U}(\underline{x})}{T_e})] - \frac{T_e}{2}ln(\frac{M_i}{2.3m_e}) \qquad (7.11)$$

and, therefore, $\Delta \bar{V}_f(\underline{x}) \approx -\Delta\tilde{U}(\underline{x})$ because the variations of $ln[2\pi(\frac{\tilde{U}(\underline{x})}{T_e})]$ are very small. It means that the variation in the ground electrode probe DC floating potential $\bar{V}_f(\underline{x})$ is approximately equal or opposite to the variation in RF plasma potential amplitude $\tilde{U}(\underline{x})$ across the reactor.
To summarize, the experimental measurements in this work are made with probes mounted in the ground electrode. The current to a grounded probe represents the DC current density flowing locally to ground, and the negative of the probe floating potential represents approximately the deviation of the RF plasma potential amplitude from the value necessary for local ambipolarity.

7.2.2 Negative charges on a thin dielectric substrate

We consider the effect of a thin dielectric substrate placed centrally on the ground electrode as in figure 7.4. By 'thin dielectric' it is meant that the capacitance of the
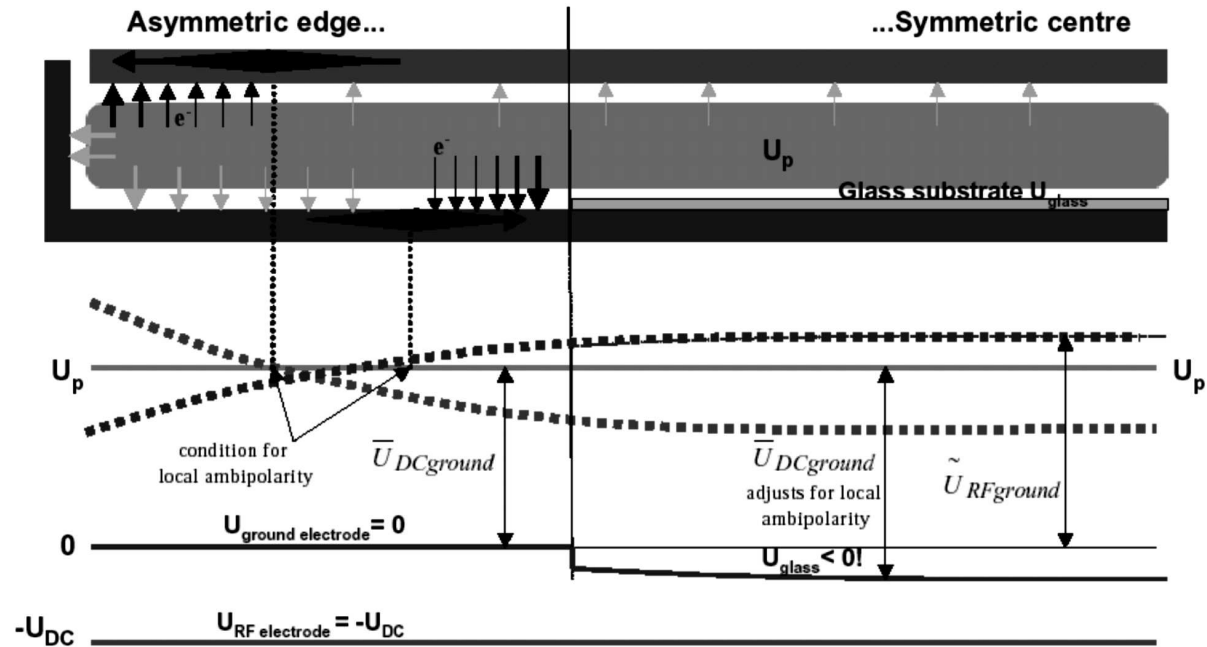

Figure 7.4: *Schematic representation of DC and RF sheath potentials considering a thin substrate on the ground electrode.*

dielectric is large compared with the sheath capacitance, therefore the dielectric substrate does not alter the RF current distribution in the reactor. Consequently, the envelope of the RF sheath potential amplitude remains the solution of the telegraph equation 7.5 in 1D cartesian geometry. The insulating substrate surface charges up to reach the DC sheath voltage necessary for local ambipolarity, according to equation 7.9. There is no circulating current above the substrate. Global ambipolarity for the ground electrode now concerns the DC current only near to the reactor edge, beyond the substrate and so the surface integral of the time-averaged sheath current is performed in the small gap between the reactor wall and the substrate edge. A schematic representation of the potentials and currents is shown in figure 7.4. There arises an electron current spike at the edge of the substrate because the RF sheath amplitude there is larger than the one necessary for local ambipolarity. Because the DC sheath potential above the substrate is larger than the DC sheath potential at the substrate edge, a surprising consequence is that the substrate surface becomes *negatively* charged. This effect has been observed experimentally by measuring a negative substrate charge [71]. This negative polarity would be impossible to explain in the context of a single potential plasma, because capacitive division between the positive plasma potential and the substrate surface would always lead to a positive substrate potential and positive surface charge.

7.3   Experimental results and comparison with a telegraph model

Figure 7.5 shows the diagram of the probe we used for measuring the DC current and the DC floating potential (cf. section 7.2.1).
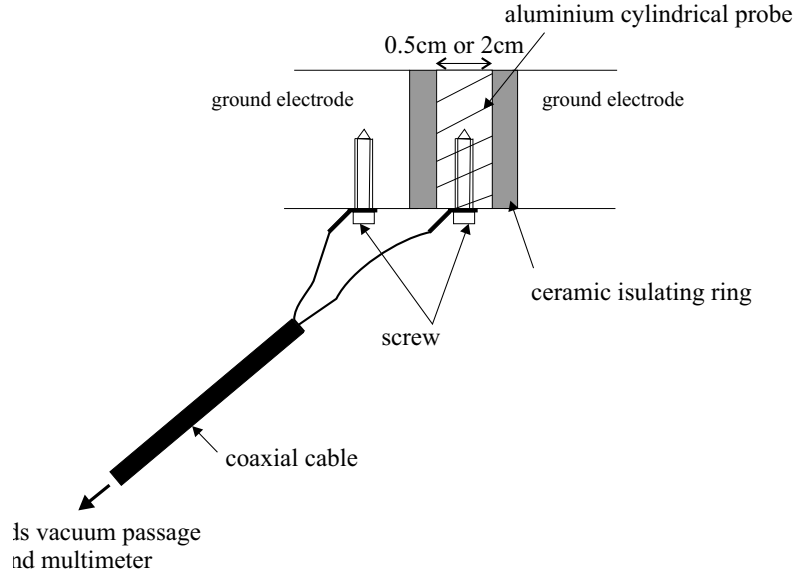
Figure 7.5: *Schematic representation of the probe used for telegraph effect measurements.*

Two kind of probes were used, 0.5 cm diameter installed in the KAI-S reactor and 2 cm diameter installed in a 1 meter diameter cylindrical reactor (cf. section 7.3.1). The RF impedance of a probe seen by the plasma should be very small compared to the sheath impedance over the probe area, so that the probe is not a perturbation for RF currents.

Sheath impedance is $Z_{sheath} = \frac{1}{\omega C_{sheath}}$ with $C_{sheath} = \frac{\varepsilon_0 S}{a}$ where a is the sheath thickness and S is the probe area. In the KAI-S reactor at 40.68 MHz, if we estimate the sheath thickness at 2 mm, Z_{sheath} is around 56 Ω. We have checked with an impedance meter that probe impedance is about few ohms at 40.68 MHz, negligible compared to sheath impedance. It was not necessary to connect a capaciton between the probe and the ground to decrease the probe circuit impedance [72].

A $6^{1/2}$ digit multimeter (Agilent 34401A) was used to measure the DC current and floating potential of the probes.

7.3.1 Cylindrical reactor

Figure 7.6 shows the the schematic cross section section of the cylindrical reactor used for the following experiments. The probe diameter is 2 cm.
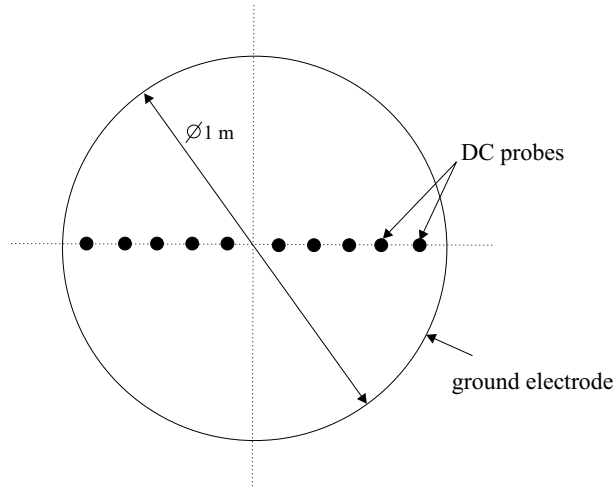

Figure 7.6: *Schematic top view of the ground electrode of the cylindrical reactor. DC probes are installed along the reactor diameter*

This plasma cylindrical reactor works on the same principle as the KAI-S reactor. It is installed in a vacuum chamber according to the Plasma Box^{TM} system. Compared to the KAI-S reactor, the major differences are the reactor cylindrical symmetry (no corner effect) and the grounded sidewall (1 cm high) is smaller than the sidewall of the RF electrode (2 cm high), therefore the grounded electrode has the smallest area, opposite to the case shown in figure 7.1 and to the KAI-S configuration. Optical fibers were also installed along the reactor diameter in the ground electrode which allow the measurement of the plasma emission intensity.

Figure 7.7 shows the measured radial profiles of the optical emission intensity, the DC current density, and the probe floating potential. These radial profiles were cylindrically symmetric, as shown in the figure, provided that the sidewall height was precisely the same around the reactor circumference [73].

The damping length λ is estimated to be a few cm (cf. figure 7.3) for the plasma parameters given in the caption to figure 7.7. At 13.56 MHz, any standing wave non-uniformity is negligible since the RF wavelength is much larger than the reactor radius. The edge plasma non-uniformity can be seen on the emission intensity profile. The plasma power is higher towards the reactor edge, in agreement with the telegraph model. The radial
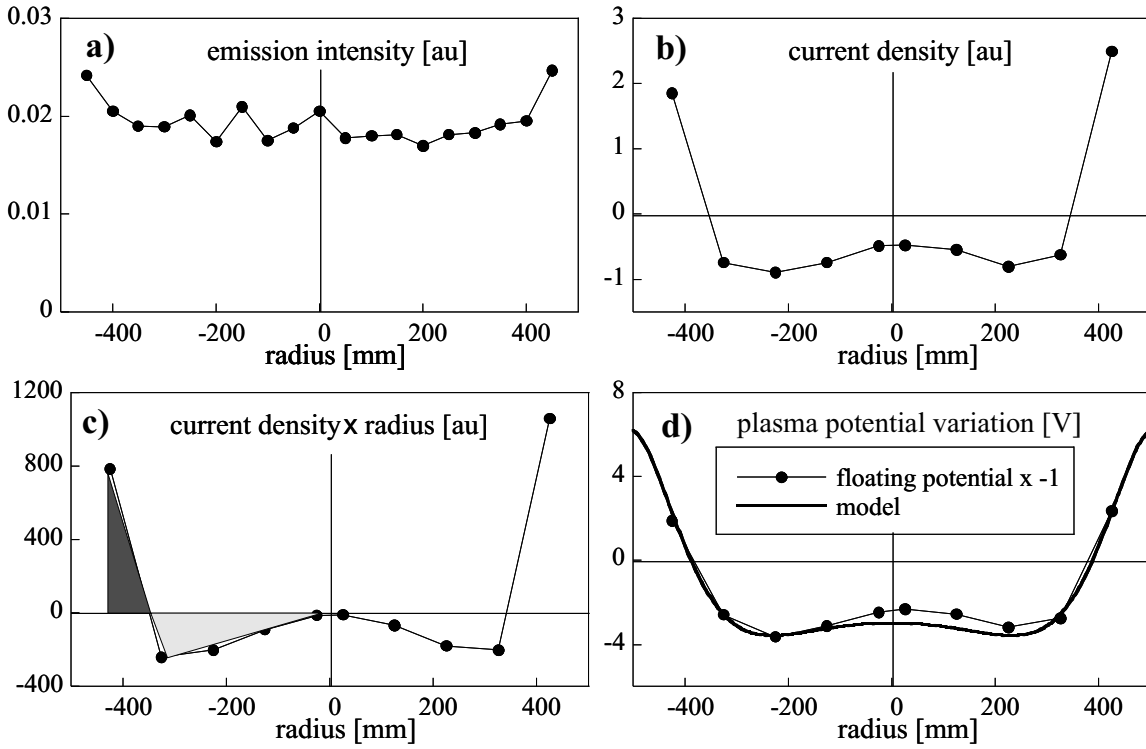
Figure 7.7: *Measured profiles of a) emission intensity, b) DC current density, c) DC current, and d) floating potential profiles for probes mounted along a 1 m diameter of the cylindrical reactor. Comparison of the deduced RF plasma potential amplitude profile with a numerical solution of the telegraph equation ($\lambda = 0.06$ m) is also shown. Electrode gap 3 cm, grounded sidewall 1 cm high, RF sidewall 2 cm. Plasma parameters: argon/hydrogen flow ratio 2:1, 13.56 MHz, pressure 100 mTorr, 200 W RF power.*

profiles of the DC current density and floating potential are both bipolar, with the zero crossing point at the same radius as expected. This radius is the null point about which the DC current circulates from larger to smaller radii. DC current from probe to plasma is defined as positive throughout this work.

The surface integral $2\pi \int_0^R r j(r) dr$ of the current density $j(r)$ shows that the net DC current to the ground electrode is indeed zero (within experimental error due to the limited number of probes defining the DC current profile) as expected for the capacitively-coupled reactor. The DC current density near the wall is majority electron current, being balanced by a majority ion current within the radius of zero current. This corresponds to the current flow in figure 7.1 for the smaller (upper) electrode.

The negative profile of the probe DC floating potential is compared with a numerical solution of the telegraph equation for the RF plasma potential amplitude in cylindrical geometry. Given the approximations made and the assumption of uniform plasma resistivity and sheath capacitance in the telegraph model, there is reasonable agreement for a value of $\lambda = 0.06$ m. Note that the deduced envelope of the RF plasma potential amplitude increases towards the wall, which corresponds to figure 7.1 for the smaller (upper) electrode. When the sidewall height asymmetry was reversed (grounded sidewall larger than the RF electrode sidewall), the DC current and floating potential profiles were inversed, as expected (cf. figure 7.8). If the sidewall height differed by a few mm around the perimeter, the cylindrical symmetry was broken and the profiles became skewed with a marked slope across the diameter, demonstrating that the sidewall geometry can have a
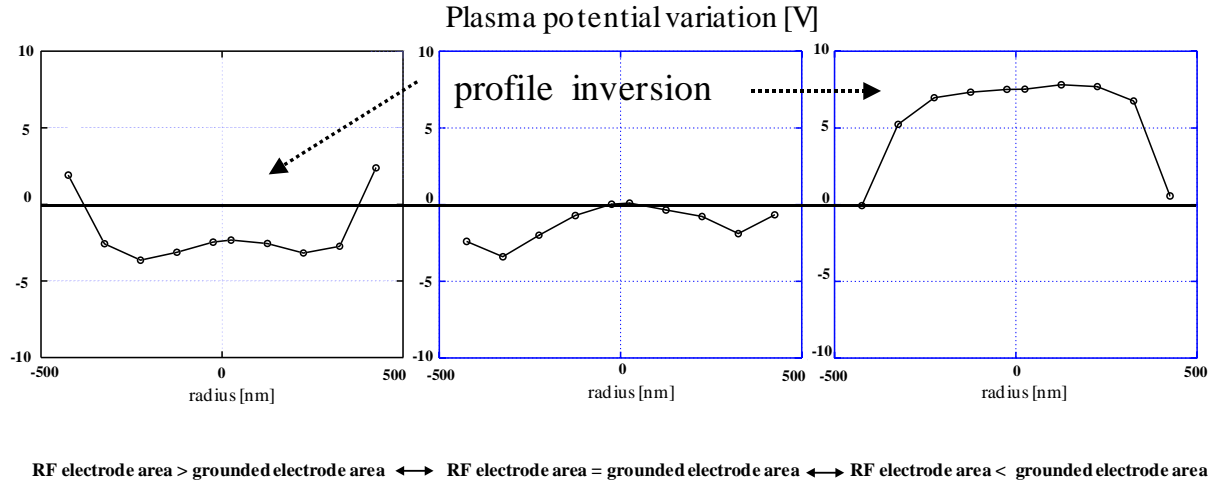
Figure 7.8: *Measured profiles of floating potential profiles for probes mounted along a 1 m diameter of the cylindrical reactor. Profile inversion is shown (Ar/H_2 plasma).*

strong influence on the plasma uniformity, even across the entire 1 m diameter. However, when the RF and grounded sidewalls were accurately equalized (equal effective sidewall areas for the ground and RF electrodes), then the measured values of probe current density and floating potential were strongly reduced along the whole diameter, indicating that there was no systematic variation in RF plasma potential, and the plasma emission intensity was uniform. Any remaining edge non-uniformity is due to fringing fields which are localized close to the junction between the sidewalls (cf. figure 7.8).

As a supplementary demonstration of the experimental method, it is interesting to consider measurements performed at a higher RF frequency where standing wave effects become important, and even dominate edge effects. Figure 7.9 shows the same profile measurements as for figure 7.7, but at 67.8 MHz. In contrast to a telegraph model at low frequency, the plasma profile is dominated by a central peak. The RF voltage amplitude has the Bessel function radial distribution $J_0(k_{eff}r)$, where k_{eff} is the effective wavenumber due to the plasma permittivity [69]. This voltage profile is a solution of Maxwell's equations in parallel plate cylindrical geometry, and is independent of plasma resistivity effects. Nevertheless, any phenomenon which causes the RF plasma potential to be non-uniform (in the presence of a uniform DC plasma potential) will cause DC currents to compensate for the local loss of ambipolarity as explained in the previous section. Figure 7.9 shows that the current density profile, as measured by the grounded probes, integrates approximately to zero. Furthermore, the negative floating potential profile approximates to a Bessel profile, shifted by a DC value corresponding to the DC plasma potential. This shows the probe method used in a different context independently of the telegraph effect.
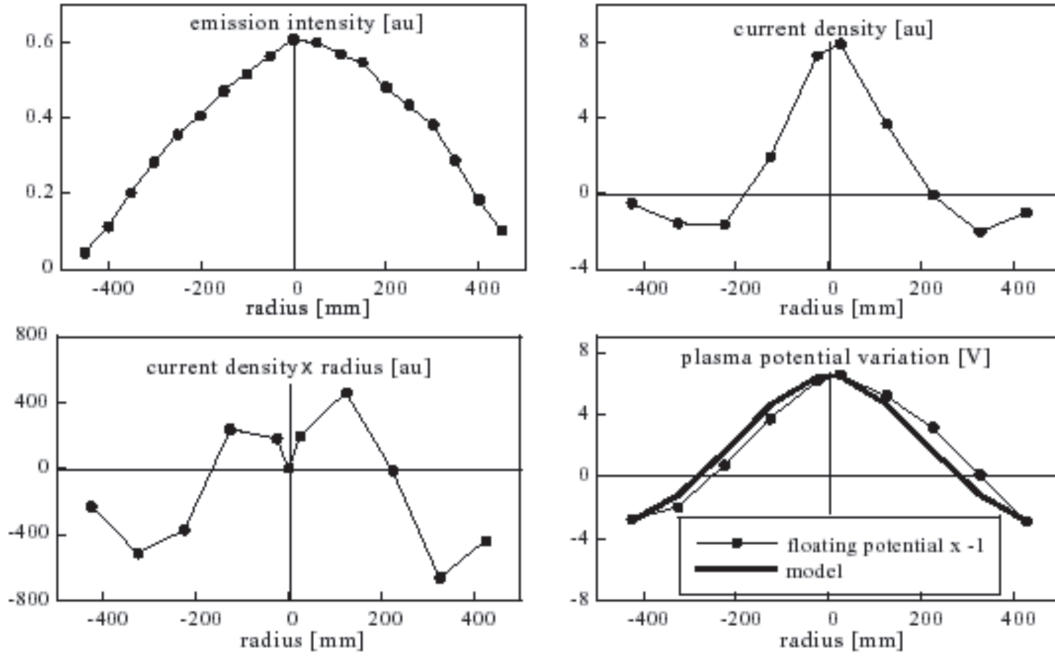
Figure 7.9: *The same cylindrical reactor as for figure 7.7, but at 67.8 MHz, Ar 250 mTorr, 300 W. The RF plasma potential amplitude profile, deduced from the probe floating potential profile, is compared with a Bessel function solution for the standing wave. The standing wave effect is seen to dominate the edge asymmetry effect at this high frequency.*

7.3.2 Rectangular reactor

The rectangular KAI-S reactor has electrode dimensions 47 cm by 57 cm, with a grounded sidewall of height 2.5 cm. The grounded electrode now has the largest area, corresponding to figure 7.1, which is the opposite case to the cylindrical reactor in the previous section. An array of surface probes (diameter 0.5 cm) is mounted in the ground electrode along a line from the reactor axis towards the sidewall (cf. figure 7.10 for the probe positions) with another probe in the sidewall itself. In figure 7.11 (a) we see that the sign of the current density is inversed (with majority DC electron current contribution this time on the interior of the grounded electrode surface) with respect to figure 7.7 because the electrode area asymmetry is reversed.

In contrast to the data presented up to now with no substrate, figure 7.11 (c) shows the DC current density measurement in presence of a centrally-positioned glass substrate 37 cm x 47 cm, leaving a 5 cm gap between the substrate edge and the sidewall. The insulating substrate now constrains the DC current to circulate in the 5 cm gap between the sidewall and the substrate. The DC plasma potential and the RF electrode self-bias voltage adjust to maintain global ambipolarity. The integral of the DC current is still roughly zero although accurate values are difficult to obtain because the current density in the vicinity of the sidewall is not measured with sufficient spatial resolution [73].

The envelope of the RF plasma potential, inferred from the negative of the DC floating potential profile, decreases towards the wall, also opposite to the behaviour for the previous results in figure 7.7 for the same reason of reversed electrode area asymmetry. This fall-off in amplitude is to reduce the RF current contribution from the grounded sidewall. The negative profile of the probe DC floating potential is compared with the analytic expression for the RF plasma potential amplitude in Cartesian geometry. There
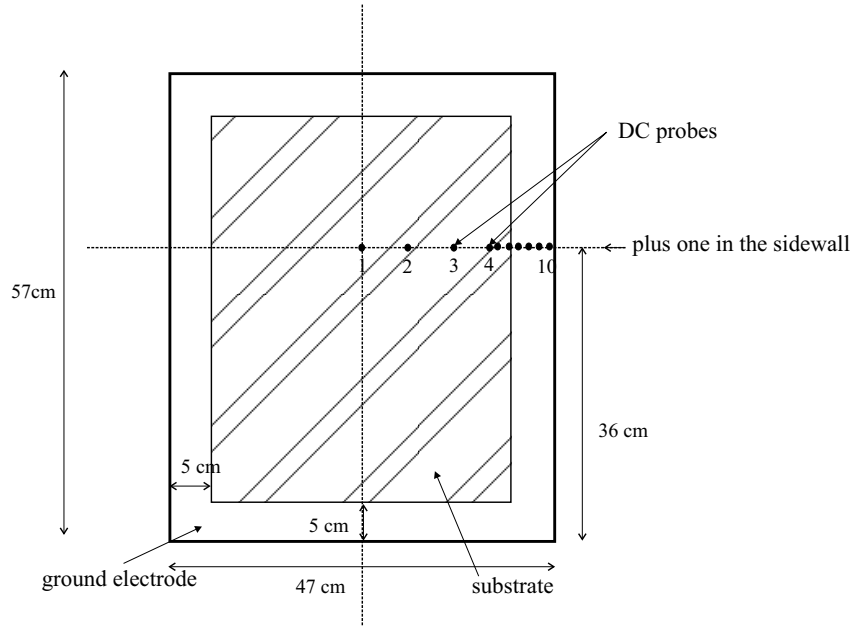
Figure 7.10: *Schematic top view of the ground electrode of the KAI-S reactor with probe positions.*

is reasonable agreement between the measurement and the telegraph 1D profile using a damping length distance $\lambda = 0.02$ m, provided that the sidewall current is 2-3 x smaller than the extrapolated value, as observed experimentally. It seems reasonable that this is due to imperfect contact of the plasma with the sidewall.

The experimental parameters were purposely chosen to obtain a damping length much smaller than the reactor width, because otherwise a one-dimensional treatment is not sufficient. Figure 7.12 shows 2D solutions of the telegraph equation in the reactor geometry for $\lambda = 0.03$ m and 0.1 m. For $\lambda = 0.1$ m, the voltage perturbation extends over a large distance, and the enhanced area asymmetry due to the corner sidewalls influences the DC current dynamo flow far from the corners, to the extent that all the probes measure a positive DC current density (unipolar profile), as observed, and the negative DC current density is concentrated in the corners. For $\lambda = 0.03$ m and less, the range of influence of the corners is restricted, and, for most of the reactor perimeter, the perturbation can be described by the 1D model as used in figure 7.11.

In conclusion, model and measurements with surface probes show that non-symmetric electrode areas cause a spatial variation in the RF plasma potential which can be described by a telegraph equation. This leads to non-uniform RF sheath voltages and RF power density. The non-uniform RF plasma potential in presence of the uniform DC plasma potential results in non-ambipolar currents circulating through the plasma and along conducting surfaces. If the electrode sidewall areas are accurately equalized, then the RF plasma potential amplitude and the power density are made uniform [69].
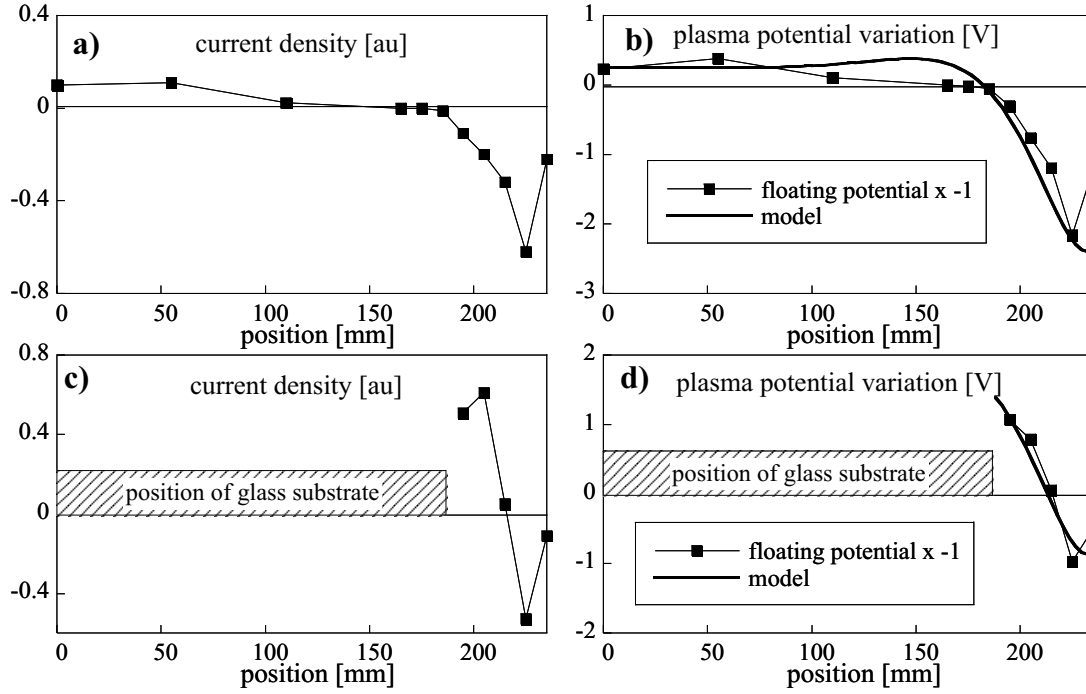
Figure 7.11: *Measured DC current density and DC floating potential profiles for probes mounted along the 0.235 m halfwidth of a rectangular reactor. Top: no substrate. Bottom: with a glass substrate to 5 cm from the sidewall. Comparisons of the deduced RF plasma potential amplitude profile with a telegraph solution ($\lambda = 0.02$ m) are also shown. Hydrogen plasma parameters: 40.7 MHz, 0.6 mbar, 60 W.*

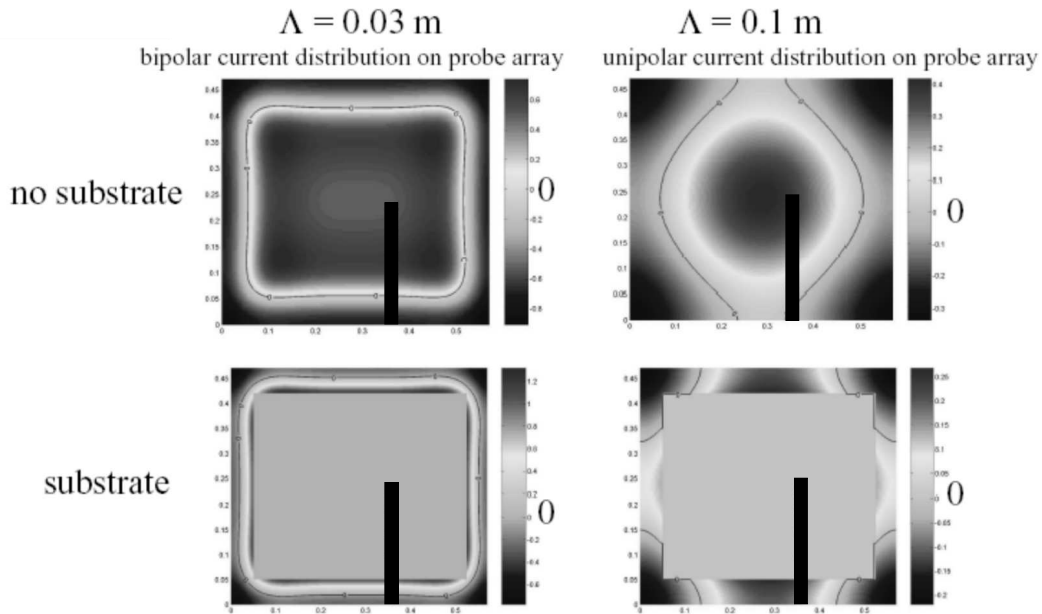

Figure 7.12: *2D colour contour plots of the RF current density solutions of the telegraph equation for damping lengths L = 0.03 m (left) and 0.1 m (right). Above: no substrate; below: with glass substrate. The location of the probe array is shown by the bar. The contour of zero DC current is indicated.*

Chapter 8

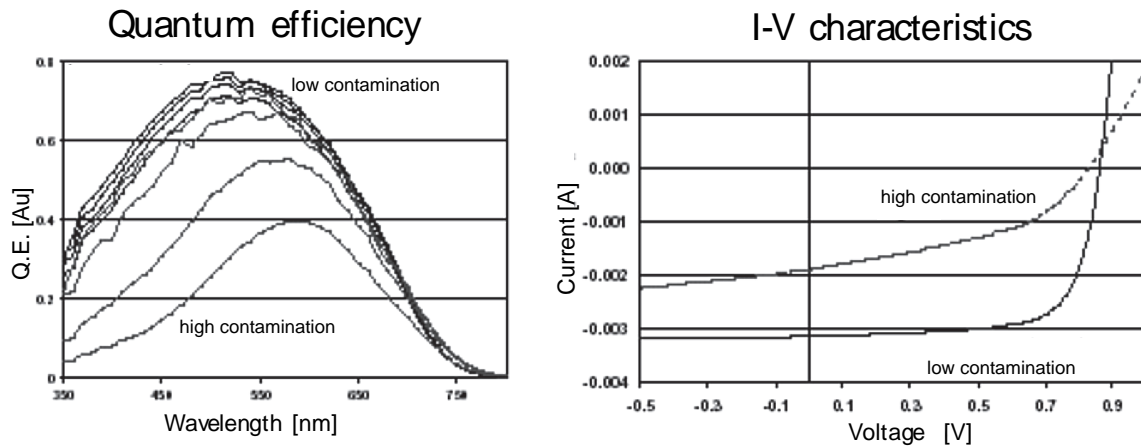# Boron contamination

8.1 Introduction

Figure 8.1: *Deterioration of cell performance with boron contamination : spectral response and IV characteristics [74]*

In all the preceding work, only the i-layer was considered. However, if only one Plasma Box^{TM} reactor is to be used for depositing solar cells, then the feasibility of single chamber operation must be investigated. Plasma-enhanced chemical vapour deposition (PECVD) of photovoltaic p-i-n solar cells in a single plasma reactor offers advantages of time and cost compared to multi-chamber processes which use separate reactors for production of the p-, i- and n-layers. The p-layer is a boron-doped silicon thin film deposited by plasma in a gas mixture containing silane and a boron source gas. In a single chamber PECVD reactor, the silane plasma subsequently used to deposit the undoped silicon intrinsic film (i-layer) leads to the recycling of impurities [75]. It can cause boron contamination from the reactor walls, pumping ducts or layer itself. Boron contaminates the i- layer at the p-i interface and thereby weakens the strength of the critical field in the i- layer close to the p-i interface. This provokes a less efficient carrier separation just in this zone and leads to a reduced collection efficiency in the solar cell. This results in a degradation of the final solar cell performance (cf. figure 8.1) [76]. Therefore, for mass production of solar cells in a single chamber reactor, it would be practical if some
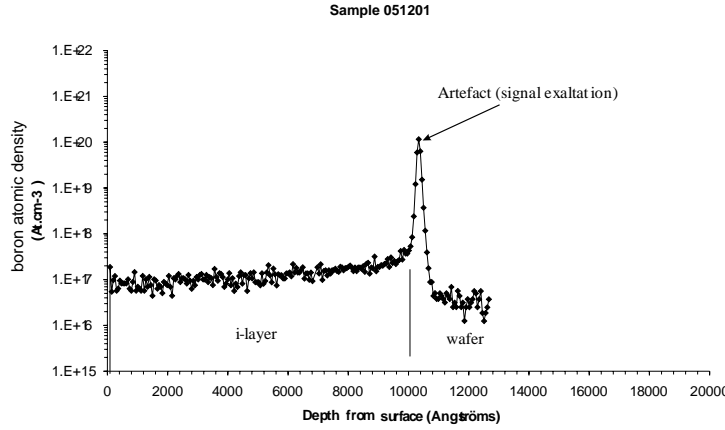
Figure 8.2: *Boron SIMS profile, background level of contamination*

treatment applied between the deposition of the p- and i-layers could reduce the boron contamination at the interface and so maintain the cell quality. The fall of boron concentration at the p-i interface should be as sharp as possible so that the transition between the p-layer and i-layer is abrupt.

In this work, various techniques to reduce the boron contamination at p-i interface were investigated. Their effectiveness was evaluated by means of Secondary Ion Mass Spectroscopy (SIMS), to study the boron concentration depth profile across the p-i interface. Trimethylboron (TMB), $B(CH_3)_3$, instead of diborane, B_2H_6, was used as the boron source gas because it has superior thermal stability in the hot reactor and causes less contamination [77]. We used the standard electrode gap KAI-S reactor. Sequences of p-i layers were deposited on silicon wafers put on a glass substrate 47cm $\times$ 37cm $\times$ 1mm to test different procedures between the p- and i-layers. The gas parameters used for the p-layer were : flow rates 70/60/1/50 sccm of $SiH_4/CH_4/TMB/H_2$ at 0.4 mbar; for the i-layer (a-Si:H) : flow rates 160/40 sccm of SiH_4/H_2 at 0.5 mbar. The excitation frequency was 27.12 MHz and 40 MHz at 60 W RF power for an i-layer deposition rate of approximately 0.3 nm/s at substrate temperature of 200° C.

We tried various procedures : pumping between p-layer deposition and i-layer deposition, reactor treatments, gas flush processes. First we will present these procedures and their influence on the level of contamination in section 8.2, from the longest to the shortest in treatment time. In the following section 8.3 we will discuss the origin and the localization of the boron contamination. In the last section 8.4, applications to solar cell manufacturing will be shown.

8.2   Treatments to remove boron contamination of the intrinsic layer

8.2.1   Background level of contamination in the reactor

On figure 8.2 we can see the boron profile of the i-layer. After one month without using TMB, the deposition was done to estimate the background level of boron contamination in the i-layer. The peak around 11000 Å (depth from surface) is an artefact effect from SIMS. The boron signal is exalted by the oxygen present at the interface layer-wafer in the native oxide. The background level of boron contamination is 10^{17} At.cm^{-3}.

It means that the lowest level of boron contamination we can possibly measure in the intrinsic layer is 10^{17} At.cm^{-3}.

8.2.2 Long time procedure

Pump all night

Compared to the untreated interface on figure 8.5, all night pumping, at 200° C and 40° C improves the p-i interface as we can see on the boron profiles of figures 8.3 and 8.4. It is surprising that the temperature does not have the expected effect on the boron profile in the i-layer. If desorption of physisorbed boron was the mechanism for reduction of the contamination, then the effect of temperature would be expected to be very opposite. It seems that the key point is the long pumping time and, or, the exposure to background water vapour at the base pressure (10^{-2} mbar) during pumping.
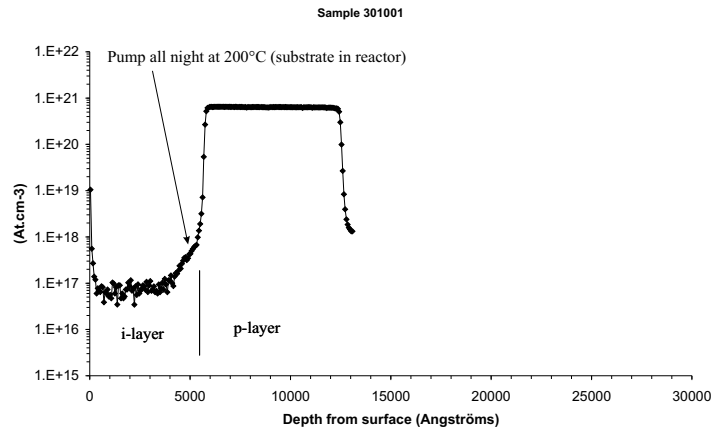

Figure 8.3: *Boron SIMS profile, one night pumping at 200° C*

Deposition of the i-layer at low power

The boron containing radicals are desorbed during a high power plasma as seen during i-layer deposition. A power of 60 W seems enough for this. If we begin the i-layer with a very low power plasma, we could hope that the boron source would be efficiently coated by the a-Si:H layer with no desorption. The boron profile resulting from the experiment is in figure 8.5. A first i-layer of 400 Å was deposited at 30 W. Then the power was increased. Compared with the not treated p-i interface, the one when beginning with a low power plasma is slightly sharper. It is presumably due to the decrease in ion flux and energy in the low power plasma. It could be an alternative treatment to the ones which require the substrate to be moved or to add specific flushing gas in the line, as we will see in section 8.2.3 and 8.2.4, although the improvement is only slight.

8.2.3 Reactor treatments between p-layer and i-layer which require substrate removal

The aim is to remove the contamination source or to seal it before the deposition of the i-layer. These treatments would degrade the quality of the final cell, therefore it is necessary to move the substrate into the loadlock.
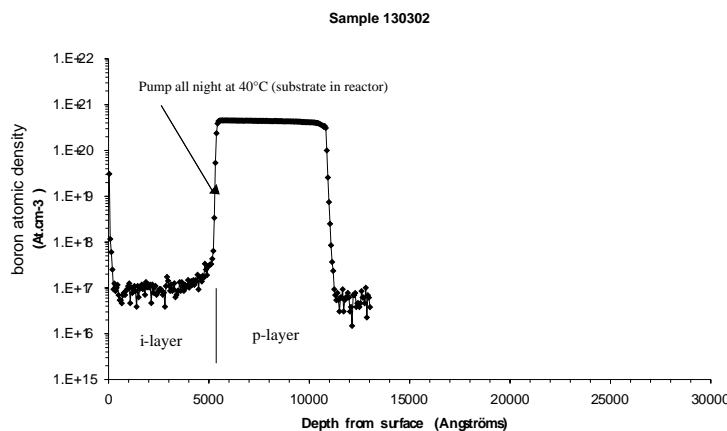
Sample 130302

Figure 8.4: *Boron SIMS profile, one night pumping at* 40° C *between p layer and i layer*
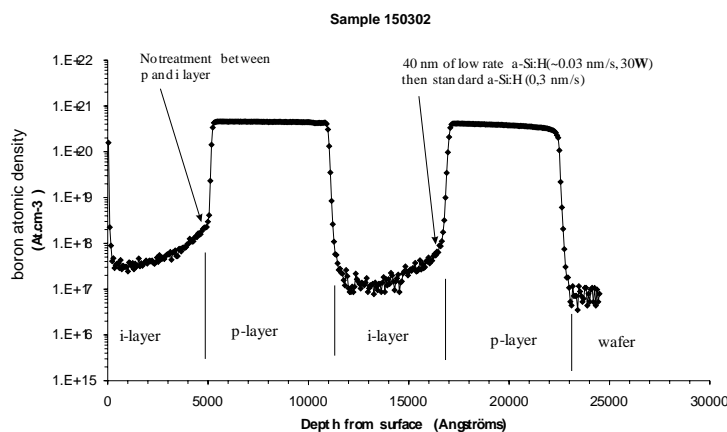
Sample 150302

Figure 8.5: *Boron profile, experience with a low power plasma*

Etch plasma cleaning

The etch plasma is used as a cleaning plasma to remove layers deposited around the reactor wall. The recipe is $50/136/20$ sccm of $He/SF_6/H_2$ at 0.5 mbar and 200 W. Here we use this treatment to 'reset' the reactor between p-layer and i-layer. The profile in figure 8.6 shows that the boron contamination at the p-i interface is efficiently treated. The profile is sharp. It also confirms that the source of boron contamination is on the reactor walls, and maybe in the pumping line also, but not directly from the p-layer on the substrate itself.

a-Si:H reactor coating

During this experiment, we removed the substrate into the loadlock and deposited $800\,\text{Å}$ of a-Si:H (standard recipe). We suppose that a part of boron radicals are removed during this high power plasma and the other part is buried under the a-Si:H layer. The boron profile on figure 8.7 shows a sharp transition between the p- layer and the i- layer. Moreover, this treatment tells us that the source of contamination is not in the pumping line because the pumping line is not coated with a-Si:H ; the path length of silane radicals out of the reactor is not more than few centimeters.

Sample 061201
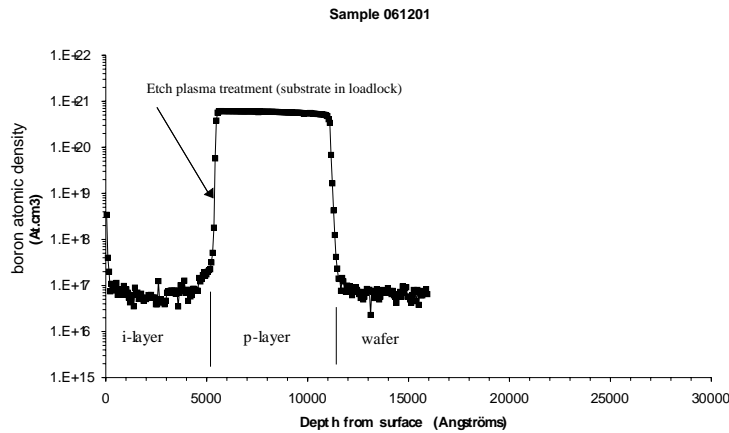
Figure 8.6: *Boron profile, etch plasma treatment*

Sample 071201
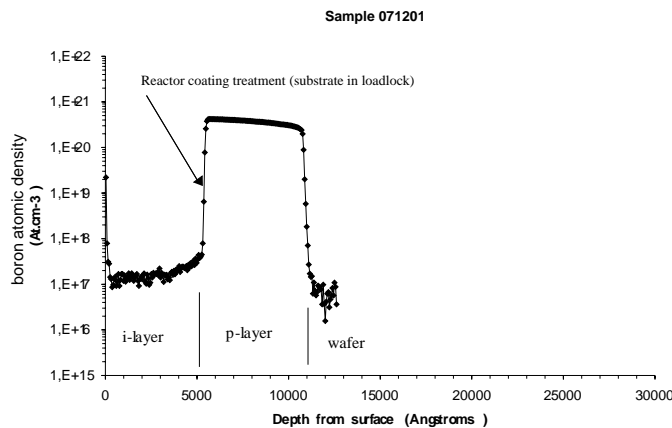
Figure 8.7: *Boron profile, reactor coating treatment*

Oxygen plasma treatment

The strategy is to immobilize the boron in the p-layer on the reactor walls by means of an oxidizing plasma : 10 minutes of plasma treatment with CO_2 [78] [79] or O_2 (figure 8.8) between the p-layer and i-layer (always with substrate in the loadlock) was observed to give a clean p-i interface. Exposure to O_2 gas alone would be expected to oxidize boron in the top monolayer, but flushing with O_2 gas was in fact ineffective. Therefore, efficient oxidation requires plasma-produced radicals, and/or oxidation of subsurface boron assisted by ion bombardment. Boron desorption by ion bombardment alone is insufficient because the same procedure using an argon or hydrogen plasma, instead of oxygen, did not reduce boron contamination of the i-layer. This idea of oxidation of the contaminant source will be used later (cf. section 8.2.4).

We have seen that these three treatments efficiently removed the boron contamination in the intrinsic layer at the p-i interface. However it is necessary to move the substrate into the loadlock, which is a significant drawback for an industrial application. Ideally, we would like to treat the boron contamination without moving the substrate, without destroying or degrading the cell, and in short time. In the following section, we will present treatments with special gas flushes which can offer all of these properties.
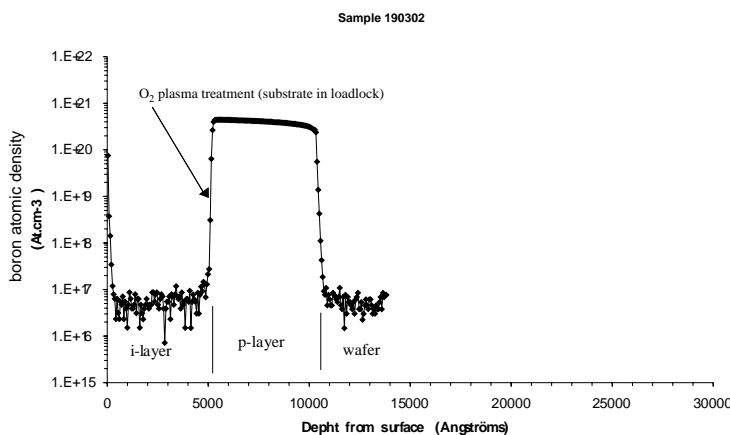
Figure 8.8: *Boron profile, O_2 plasma treatment*
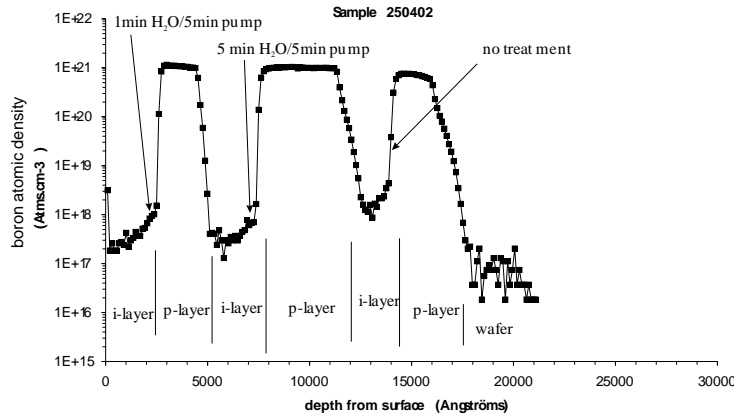
8.2.4   Gas flush treatment

Hydrogen and Argon flush
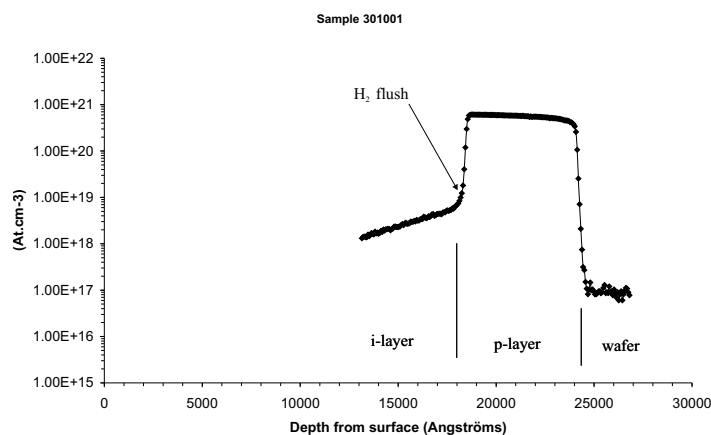
Figure 8.9: *Boron profile, H_2 flush*

Argon flush or hydrogen flush have no effect to remove the boron contamination, as can be seen in figure 8.3 for a H_2 flush. This shows that the boron contamination is not due to residual TMB gas in the reactor, but rather due to boron radicals in the deposited layers on the reactor walls. The boron radicals are not immobilized by argon or hydrogen as an O_2 plasma because these molecules are not reactive.

Water vapour flush

In section 8.2.3 we saw that boron contaminants are efficiently oxidized during an O_2 plasma but not by O_2 gas. They can, however, be oxidized during a water vapour flush: a volume of deionized water was connected to the reactor, outside the chamber, through a second process line and a manual valve. When opening the valve, water boils and water vapour flushes into the reactor. The reactor pressure is maintained by the throttle valve at 0.1 mbar. In figure 8.10 we can compare the level of boron after no treatment and after a water treatment. We have the confirmation of the action of water vapour to give a sharper transition at the p-i interface. Five minutes exposure is slightly better than one minute exposure. We have varied the pumping time after water exposure (cf. figure

Figure 8.10: *Water vapour flush treatment, variation of exposure time*

8.11). From the boron profile, we can see that one minute pump time after five minutes of water flush efficiently decreases the boron contamination at the interface. We suppose that boric acid $B(OH_3)$ is formed and is pumped out or is fixed in the p-layer. We can add that the exposure to residual water vapour during the overnight pumping may be the reason for the effectiveness of long pumping (cf. section8.2.2).
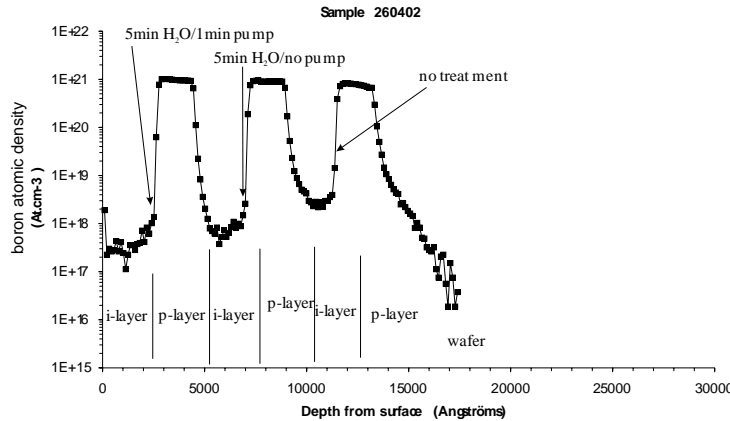
Figure 8.11: *Water vapour flush treatment, variation of pumping time*

This water vapour treatment was tested successfully in a one chamber process for solar cell manufacturing (cf. section 8.4) [76].

Ammonia flush

Drawing on previous experience with diborane/ammonia plasma reactions, it was suggested that ammonia gas flushing might be a suitable alternative to water vapour (Ch. Hollenstein's private communication). Between deposition of the i-layer and p-layer, an ammonia flush was done during 1 min at 0.3 mbar and then 1 min at 0.1 mbar for the second pair of layers. The third interface had no treatment. After each ammonia flush, a pumping period of 1 min was done. Figure 8.12 shows the SIMS boron profile of the p-i-p-i-p-i structure, superposed with the profile of a p-i interface treated with water vapour treatment (5 min H_2O flush and 5 min pump). First, if we compare the two p-i interfaces treated with the NH_3 with the one with no treatment, we observe a sharper, cleaner

transition when using the ammonia flush treatment. Second, the p-i interface treated with ammonia is similar to the p-i interface treated with the water vapour treatment flush.
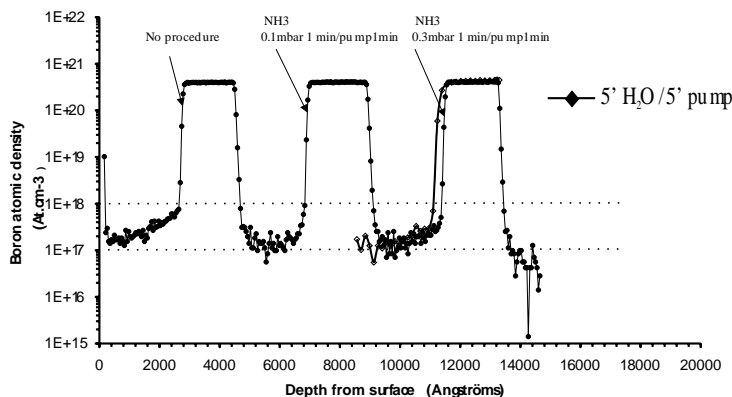

Figure 8.12: *NH$_3$ flush treatment, variation of pressure exposure, compared with no procedure profile. A profile with water vapour treatment is superposed for comparison.*

One advantage of the ammonia treatment compared to the water vapour treatment is that it is not adding oxygen contamination [48]. Oxygen impurities have been found to cause an increase in the space charge density and a degradation of the light induced effect [48,80]. Also, ammonia does not physisorb to the same extent as water which requires high temperature baking (370°C) for complete removal [81]. Figure 8.13 shows the oxygen SIMS profile of the previous p-i-p-i-p-i structure treated with ammonia, and the profile of a p-i-p-ip-i structure for which interfaces were treated with water vapour flush treatment. We can see that the level of oxygen in layers is smaller when using the ammonia treatment.

At present it is believed that the action of the ammonia flush creates B-N complexes which selectively fix boron in the p-layer or which are evaporated from the p-layer surface and pumped away. The plasma chemistry of diborane/ammonia has been investigated by infrared absorption spectroscopy. Mixing ammonia and diborane gases as precursors leads to rich gas phase precursors. Solid compounds of diammoniate of diborane $[H_2B(NH_3)_2]^+[BH_4]^-$ and aminoborane ($H_2B=NH_2$) are produced [82]. We can suppose that similar reactions happen between boron and ammonia : formation of boron nitride B:N:H, or amines $B(NH_2)_3$ instead of boric acid $B(OH)_3$ when using water [76,83].

8.3   Nature and localization of the boron contamination

8.3.1   Nature of the boron contamination

Trimethylboron (TMB) is not the source of the boron contamination as can be seen from the following. During an experiment, the TMB flush and pressure was established for the deposition of the p-layer but without igniting the plasma (substrate in the reactor). Then we deposited the standard i-layer and finally the standard p-i layers. The boron profile (figure 8.14) shows that, except for the peak at the interface i-layer/wafer (cf. section 8.2.1), the level of boron in the first i-layer is the background level. Physisorbtion
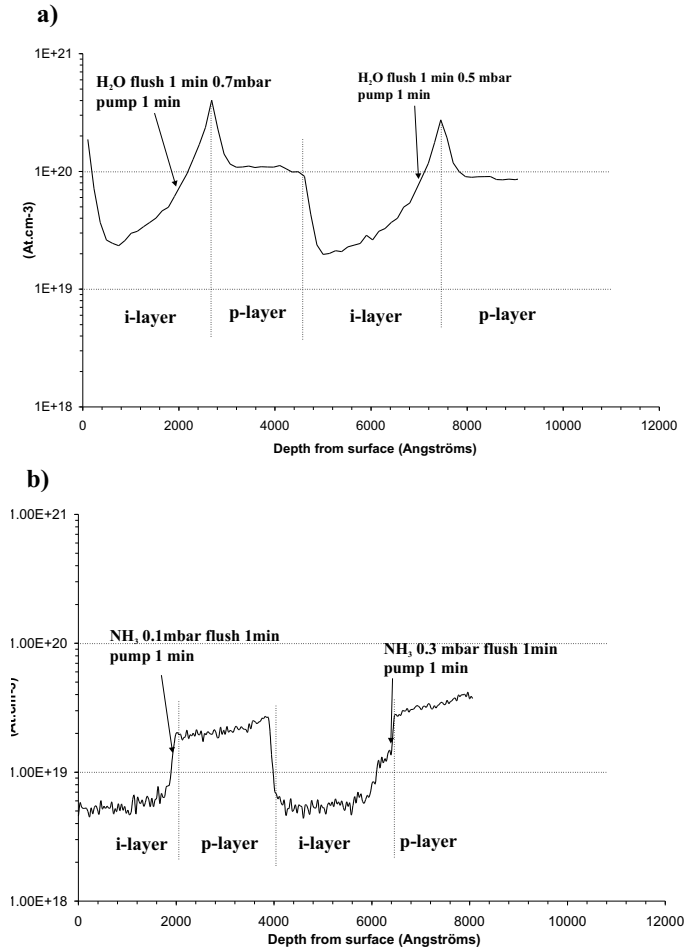
Figure 8.13: *a) Water vapour pressure treatment, b) NH₃ flush treatment : comparison of the oxygen profile.*

of TMB is therefore not a source of contamination. The sources of contamination are boron components created by the plasma. This is confirmed by A. Lloret et al. [77].

8.3.2 Localization of the boron contamination

From the experiment of section 8.2.3, reactor coating treatment, we have already concluded that the source of contamination is not in the pumping line. We can add also that the p-layer on the substrate does not contribute to the i-layer contamination, because otherwise, reactors treatments presented in section 8.2.3 would be ineffective. It is surprising that the p-layer on the reactor wall is the source of contamination and not the p-layer on the substrate, whereas they should have the same properties. Moreover, it is the condition for the multi-chamber process to work as the p-i interface is not contaminated when depositing the i-layer in another reactor. One supposition is that intense plasma at the electrode edges, due to non uniform plasma, implies the deposition of poor sticking, porous p-layer, or p-doped particles at the reactor corners. In conclusion, boron contamination of the i-layer probably desorbs from the deposited p-layer on the reactor walls during high power plasma i-layer deposition.
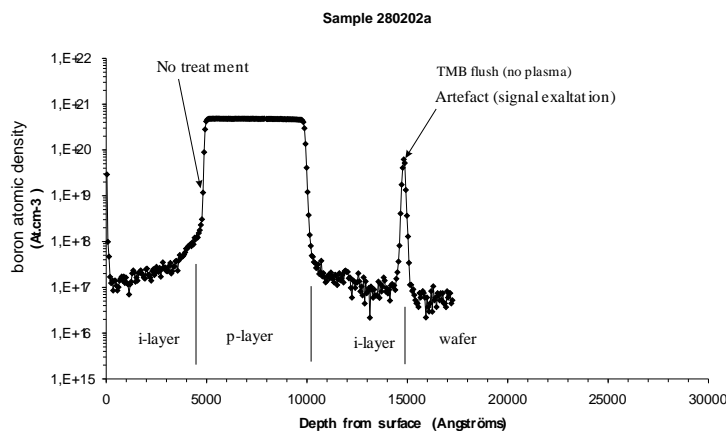
Figure 8.14: *i-p-i structure, TMB flush not source of contamination*

8.4   Application to solar cells

Figure 8.15 (a) and (b) show the I-V measurements of cells prepared with ammonia treatment (various flushing and pumping times) and the I-V measurements of a cell prepared with the water vapour flush treatment, before and after degradation. Initially (cf. figure 8.15 (a)), there is no significant influence of the ammonia flushing and pumping time. Ammonia cells are comparable to the cell prepared with water vapour flush, except for a loss in V_{oc} of 20 mV. Their efficiencies are significantly better than the performance of the cell prepared with a 30 min pumping between p-layer and i-layer (cf figure 8.15 (c)).

After degradation, (figure 8.15 (b)), the ammonia treatment does not worsen the cells degradation. All cells done with the ammonia treatment are better than the cell done with 30 min pumping and comparable to the water vapour flush treatment cells.

In figure 8.16 (a) and (b) the quantum efficiencies for a cells prepared with ammonia flush and water vapour flush are shown. Quantum efficiencies in the blue region show only a small bias-voltage dependence compared to the one on figure 8.16 (c) for a cell prepared with only a 30 min pumping time between p-layer and i-layer. The weak voltage dependence of the quantum efficiency in the blue region represents a good carrier collection in the i-layer close to the p-layer, and suggests a low boron contamination at the p-i interface. This has been confirmed by the SIMS profiles in previous sections which show sharp p-i interfaces when using ammonia or water vapour treatment.

To summarize, the source of boron contamination appears to be the p-layer deposited around the reactor walls. As we saw in section 8.2.2, if we wait a long time, the boron radicals are slowly desorbed or slowly transformed and eventually immobilized in the p-layer. If the p-layer deposition is immediately followed by the deposition of an i-layer at high power, boron radicals are desorbed and contaminate the i-layer. The solution is to remove the p-layer on the wall by etching, or to immobilize it by oxidization or nitridation, or by sealing the p-layer with a low rate i-layer deposition. Figure 8.17 is a summary of all the treatments we tested and their effect on boron contamination. Both cells prepared with ammonia flush and H_2O flush have performances which met industrial specifications. The possibility to solve the boron contamination in a single chamber is the key point for the industrial development of the KAI type reactor for the solar cell application. These two treatments are patented [84].
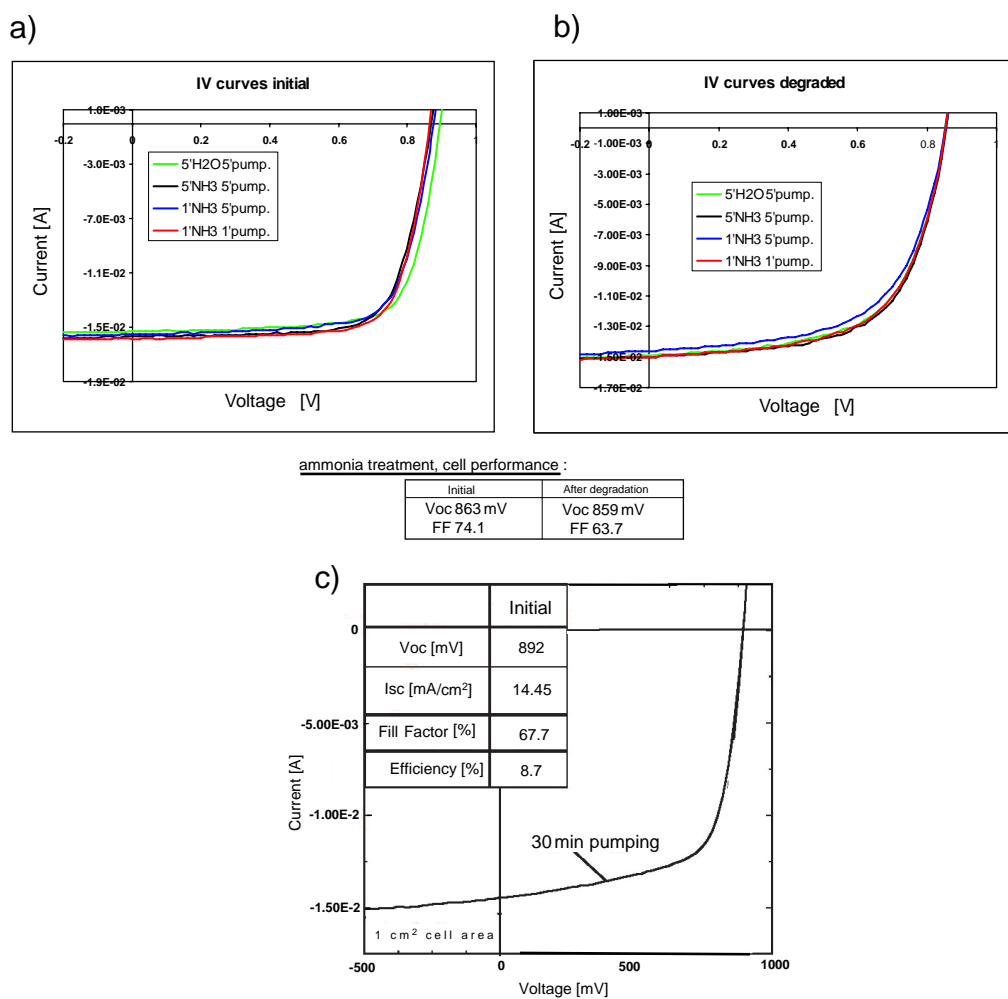
Figure 8.15: *Effect of ammonia flush on the I-V characteristics of a-Si:H cells, compared with the water vapour flush treatment : a) initial and b) after degradation. c)initial I-V characteristics of a-Si:H cell, 30 min pumping between p- layer and i- layer.*
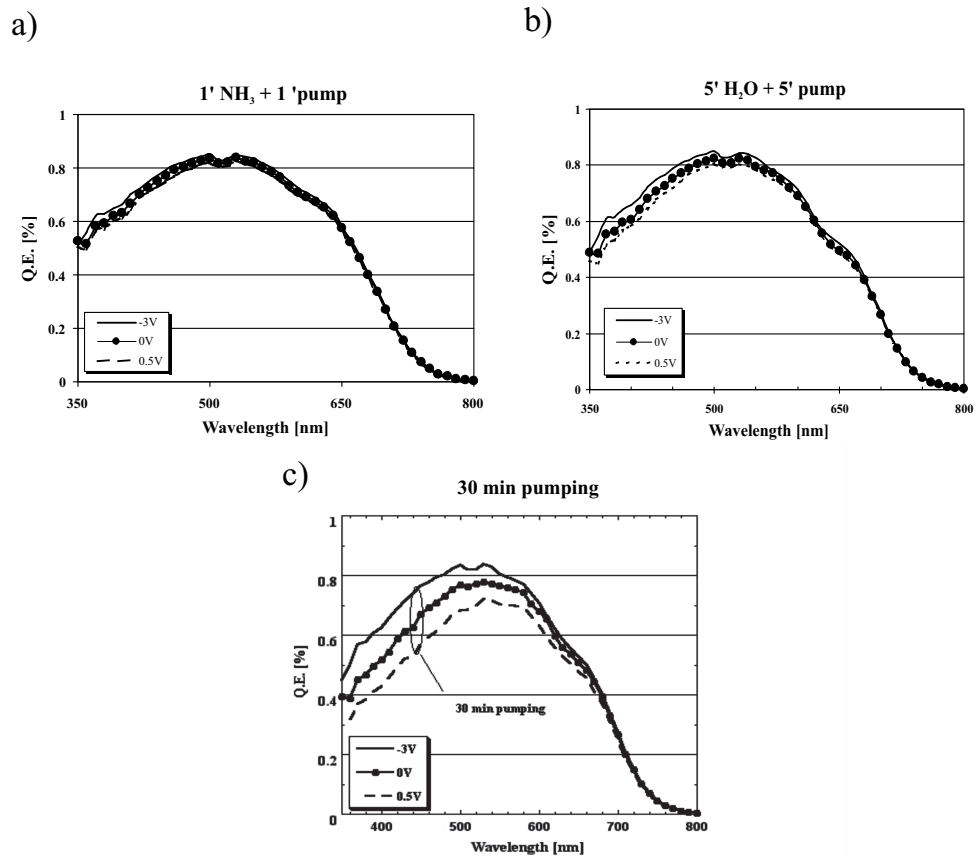
Figure 8.16: *Effect of a) ammonia flush, b) water vapour flush and c) 30 min pumping on the bias-voltage dependent quantum efficiencies.*
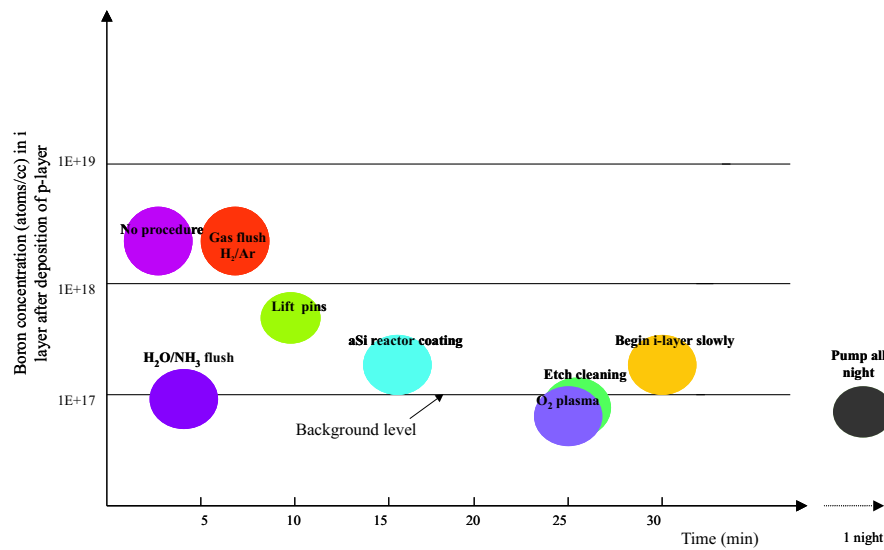
Figure 8.17: *Summary of all treatments and their action on the boron contamination at p-i interface*

Chapter 9

Conclusions

During this thesis work, we have studied the deposition of amorphous silicon by plasma enhanced chemical vapour deposition in a large area, radio-frequency reactor. These studies were about the effect of the reactor design and the plasma conditions on layer deposition rate and layer density. Other aspects of plasma assisted deposition were examined : the plasma non-uniformity due to the non-symmetry of the reactor electrodes and the boron cross-contamination which is a critical aspect for solar cell deposition in single chamber reactor.

These studies required the elaboration and the comprehension of diagnostics such as deposition rate measurement by in-situ interferometry, plasma power measurements and layer density measurement by ellipsometry. In chapter 4, we have developed the theory of white light interferometry for in-situ layer monitoring (deposition rate, energy gap) and the theory of layer density measurement by ellipsometer. In particular, we have shown how the ellipsometric measurement can be distorted because of the layer roughness. During the thesis we have also designed a matching-box circuit for using process frequencies of 27.12 MHz and 40.68 MHz.

Concerning the effect of the reactor design on a-Si:H layer deposition rate, we have observed that decreasing the reactor electrode gap leads to an increase of the deposition rate. This increase of the deposition rate could be the consequence of an increase in electron temperature T_e and a consequence of the sheath coalescence when the electrode gap decreases. Nevertheless, in a small electrode gap reactor (1.7 cm) non-uniformity problems increase due to edge focusing and powder effects. Locally intense plasma at the reactor edge implies a higher silane depletion in this zone which results in a faster deposition rate and thicker layer at the substrate edge. This edge focusing can be solved by a teflon jigsaw to keep the plasma away from the edge confined space. The second non-uniformity problem, the powder effect, is due to the accumulation of powder at the edge as viscous drags reduce the gas flow at closed boundary, especially in a small electrode gap reactor. Concerning a-Si:H layer density study, systematic ellipsometric measurements of density have shown that it decreases when deposition rate increases, independently of pressure, gas flow and frequency (27.13 MHz/40.68 MHz) of the plasma. The deterioration of the layer density at high deposition rate (above 4 Å/s) may be a consequence of a higher contribution of SiH_2 in film growth and a smaller radical surface diffusion. The importance of surface diffusion was recognized since model and experiments have shown that conditions of low radical surface diffusion lead to high void fraction volume in the bulk [44,51].

The determining factor for faster surface diffusion and dense film growth is probably the substrate temperature. Our experiments have shown that layers deposited at high temperature process (from 230°C to 280°C) have a good density, even at high deposition rate. Nevertheless, industrial constraints impose a process temperature at 200° and a standard gap reactor. By optimising the process parameters, keeping the temperature process at 200°C, good quality, uniform a-Si:H layers were deposited at 3 Å/s on 37 cm × 47 cm glass substrates at 40.68 MHz.

A general aspect of layer deposition in a large area reactor has been studied. In small area capacitive reactors, the RF and DC components of the plasma potential can be assumed to be uniform over all the plasma bulk. In large area reactors however, a perturbation in RF plasma potential, due to electrode edge asymmetry or the boundary of a dielectric substrate, propagates to the middle of the reactor. The RF plasma potential varies across the reactor with a characteristic damping length λ according to a telegraph equation. In this work, the RF frequency (40.68 MHz) is low enough such that standing wave effects are negligible. The estimated damping length for our plasma conditions is around 5 cm to 10 cm which means that the RF plasma potential non-uniformity will extend within the edge of the substrate, and cause a non-uniform deposition rate on the substrate.
Another consequence of this non-uniform RF plasma potential is that a thin dielectric substrate placed centrally in the ground electrode will become negatively charge on its surface. This has been observed experimentally by measuring a negative substrate charge [71]. Furthermore this non-uniform RF plasma potential means that the condition between RF and DC sheath voltages for zero DC current flow is not satisfied. A local DC current flows across the sheaths, circulates through the plasma and returns via the conducting surface of the electrode. It is possible to measure this local DC current with probes mounted in the ground electrode. The experimental measurements confirm the presence of a local DC current and a spatial variation in the RF plasma potential as described by the telegraph equation.

The last aspect of this work concerns the boron-cross contamination of the p-i interface. In a single chamber PECVD reactor, like the Plasma Box^{TM}, the deposition of the intrinsic layer follows the deposition of the boron-doped layer, which can cause boron contamination from the reactor walls. The result is a degradation of the final solar cell performance [76]. The solution is to apply a reactor treatment before the i-layer deposition : to remove the p-layer on the wall by etching or to immobilize it by oxidation (water vapour flush treatment) or nitridation (ammonia flush treatment). It appears that water vapour flush treatment and ammonia flush treatment are fast, efficient treatments. Cells prepared with one of these two treatments have performances which meet industrial specifications.

Finally, the results obtained during this thesis have shown the feasibility of the deposition of good quality solar cells in an industrial Plasma Box^{TM} reactor in a single chamber process, using faster deposition rate for the a-Si:H intrinsic layer. Some reactor design modifications to improve the layer uniformity and increase the deposition rate of a-Si:H layer were also proposed.

Appendix A

Pressure scaling law in large area reactor

We assume that the showerhead flow is uniform. For a viscous flow between parallel planes (single side pumping) :

$$\frac{\Delta p}{p} = \frac{6\eta L_x Q}{a^3 L_y p^2} \tag{A.1}$$

where a is the electrode gap, L_x and L_y the length and width of planes and Q the total flow.

Numerical estimations:

At 200°C for pure silane, $\eta = 1.5.10^{-5}$ kg.m^{-1}.s^{-1}, the pressure non-uniformity in the reactor is :

$$\frac{\Delta p}{p} = 1.5.10^{-5}.\frac{Q(sccm)}{a^3(cm^3).p^2(mbar^2)}.\frac{L_x}{L_y} \tag{A.2}$$

For KAI-S electrode dimensions of 57 cm × 47 cm, a silane flow of 100 sccm, a pressure of 0.8 mbar and an electrode gap of 1.4 cm (small gap reactor condition), the pressure non-uniformity is :

$$\frac{\Delta p}{p} = 0.07\,\%$$

For a 1 m² reactor, 300sccm of pure silane, 0.1 mbar, electrode gap of 2.5 cm (standard gap condition), the pressure non-uniformity is :

$$\frac{\Delta p}{p} = 2.3\,\%$$

Bibliography

[1] M. A. Lieberman and J. Lichtenberg, *Principles of Plasma Discharges and Materials Processing.* John Wiley and Sons, 1994.

[2] L. Sansonnens. PhD thesis, Ecole Polytechnique Fédérale de Lausanne, March 1998.

[3] S. Eliezer and Y. Eliezer, *The Fourth State of Matter.* IOP, 2001.

[4] D. E. Carlson and C. R. Wronsky *Applied Physics Letters*, vol. 28, p. 671, 1976.

[5] K. Tanaka, *Glow-Discharge Hydrogenated Amorphous Silicon.* KTK Scientific Publishers, Tokyo, 1989.

[6] G. Strasser, J. P. M. Schmitt, and M. E. Bader *Solid State Technology*, vol. 37, p. 83, 1994.

[7] J. Perrin, J. Schmitt, C. Hollenstein, A. A. Howling, and L. Sansonnens *Plasma Phys. Control. Fusion*, vol. 42, p. 353, 2000.

[8] J. Perrin, P. Molinas-Mata, and P. Belenguer *Journal of Physics D : Applied Physics*, vol. 27, p. 2499, 1994.

[9] K. Köhler, J. W. Cobrun, D. E. Horne, E. Kay, and J. H. Keller *Journal of Applied Physics*, vol. 57, p. 59, 1985.

[10] M. M. Salem and J. F. Loiseau *Journal of Physics D : Applied Physics*, vol. 29, p. 1181, 1996.

[11] V. A. Godyak and R. Piejak *Journal of Vacuum Science Technology A*, vol. 8, p. 3833, 1990.

[12] C. M. Horwitz *Journal of Vacuum Science Technology A*, vol. 1, p. 1795, 1983.

[13] A. A. Howling, J.-L. Dorier, C. Hollenstein, U. Kroll, and F. Finger *Journal of Vacuum Science Technology A*, vol. 10, p. 1080, 1992.

[14] A. R. Forouhi, *Properties of Amorphous Silicon*, ch. Electrical and Optical Properties of Amorphous Silicon, p. 337. INSPEC, The Institution of Electrical Engineers, London and New York, second ed., 1989.

[15] L. Sansonnens, D. Franz, C. Hollenstein, A. A. Howling, J. P. M. Schmitt, E. Turlot, T. Emeraud, U. Kroll, J. Meyer, and A. Shah *Proc. 13th EC Photovoltaic Solar Energy Conf., Nice*, p. 319, 1995.

[16] I. Solomon, M. Bhatnagar, and M. Rosso *Proc. 10th EC Photovoltaic Solar Energy Conf., Lisbon*, p. 154, 1991.

[17] M. Stchakovsky. PhD thesis, Université de PARIS-SUD, Centre d'Orsay, September 1991.

[18] D. E. Aspnes *Thin Solid Films*, vol. 89, p. 249, 1982.

[19] U. Kroll, J. Meier, M. Goetz, A. Howling, J.-L. Dorier, J. Dutta, A. Shah, and C. Hollenstein *Journal of Non-Crystalline Solids*, vol. 59-62, p. 164, 1993.

[20] E. Bhattacharya and A. H. Mahan *Appl. Phys. Lett.*, vol. 52, p. 1587, 1988.

[21] U. Kroll. PhD thesis, Institut de Microtechnique, Université de Neuchâtel, December 1994.

[22] C. A. Balanis, *Advanced Engineering Electromagnetics*. J. Wiley, 1989.

[23] I. M. Gottlieb, *Practical RF power design techniques*. Mc Graw Hill, 1993.

[24] F. E. Terman, *Radio Engineers' Handbook*. Mc Graw Hill, 1943.

[25] M. Born and E. Wolf, *Principles of Optics*. Pergamon Press, 1970.

[26] A. R. Forouhi and I. Bloomer *Physics Review B*, vol. 34, p. 7018, 1986.

[27] G. E. Jellison, Jr., and F. A. Modine *Applied Physics Letters*, vol. 69, p. 371, 1996.

[28] G. E. Jellison, Jr., F. A. Modine, P. Doshi, and A. Rohatgi *Thin Solid Films*, vol. 313-314, p. 193, 1998.

[29] D. A. G. Bruggeman *Annalen der Physik*, vol. 24, p. 637, 1935.

[30] D. E. Aspnes, B. G. Bagley, and A. C. Adams *Bulletin of American Physical Society*, vol. 25, p. 12, 1980.

[31] W. Press, B. P. Flannery, S. A. Teukolsky, and W. T. Vetterling, *Numerical Recipes in Pascal*. Cambridge Press, 1989.

[32] A. P. *et al. Solar Energy Materials and Solar Cells*, vol. 73, p. 321, 2002.

[33] J. Krc, M. Zeman, F. Smole, and M. Topic *Journal of Applied Physics*, vol. 92, p. 749, 2002.

[34] R. C. *et al. Applied Surface Science*, vol. 154-155, p. 217, 2000.

[35] G. E. Jellison, Jr., M. F. Chislom, and S. M. Gorbatkin *Applied Physics Letters*, vol. 62, p. 3348, 1993.

[36] F. Finger, U. Kroll, V. Viret, A. Shah, W. Beyer, X.-M. Tang, J. Weber, A. A. Howling, and C. Hollenstein *J. Appl. Phys.*, vol. 71, p. 5665, 1992.

[37] Y. Maemura, H. Fujiyama, T. Takagi, R. Hayashi, W. Futako, M. Kondo, and A. Matsuda *Thin Solid Films*, vol. 80-84, p. 345, 1999.

[38] R. C. Ross and J. J. Jaklik *J. Appl. Phys.*, vol. 55, p. 3785, 1984.

[39] C. Hollenstein, A. A. Howling, C. Courteille, J.-L. Dorier, L. Sansonnens, D. Magni, and H. Müller *MRS Symp. Proc. Amorphous and Microcrystalline Silicon Technology*, vol. 507, p. 547, 1998.

[40] D. Franz diploma internal report, EPFL, march 1995.

[41] R. N. Franklin, *Plasma Phenomena in Gas Discharges*. Clarendon Press, 1976.

[42] G. R. Misium, A. J. Lichtenberg, and M. A. Lieberman *J. Vac. Sci. Technol. A*, vol. 7, p. 1007, 1989.

[43] S. Sriraman, E. S. Aydil, and D. Maroudas *J. Appl. Phys.*, vol. 92, p. 842, 2002.

[44] J. A. Thornton *SPIE Modeling of Optical Thin Films*, vol. 821, p. 95, 1987.

[45] A. Gallagher *J. Appl. Phys.*, vol. 63, p. 2406, 1988.

[46] C. C. Tsai, J. C. Knights, G. Chang, and B. Wacker *J. Appl. Phys.*, vol. 59, p. 2998, 1986.

[47] J. Perrin, M. Shiratami, P. Kae-Nune, H. Videlot, J. Jolly, and J. Guillon *J. Vac. Sci. Technol. A*, vol. 16, p. 278, 1998.

[48] J. Schmitt *Thin Solid Films*, vol. 174, p. 193, 1989.

[49] O. Leroy, G. Gousset, L. A. Alves, J. Perrin, and J. Jolly *Plasma Sources Sci. Technol.*, vol. 7, p. 348, 1998.

[50] J. Perrin, O. Leroy, and M. C. Bordage *Contrib. Plasma Phys.*, vol. 36, p. 3, 1996.

[51] D. L. Smith, *Thin Film Deposition : Principles and Practice*. Mc Graw Hill, 1995.

[52] J. Perrin, I. Solomon, B. Bourdon, J. Fontenille, and E. Ligeon *Thin Solid Films*, vol. 62, p. 327, 1979.

[53] R. W. Collins, I. An, H. V. Nguyen, Y. Li, and Y. Lu *Physics of Thin Films*, vol. 19, p. 49, 1994.

[54] J. A. Thornton, *Amorphous Metals & Semiconductors Proc. Int. Workshop*, p. 299. P. Haasen & R. Jaffee Pergamon Press, 1986.

[55] T. Nishimoto, M. Takai, H. Miyahara, M. Kondo, and A. Matsuda *J. of Non-Crystalline Solids*, vol. 299-302, p. 1116, 2002.

[56] T. Shimizu, K. Nakazawa, M. Kumeda, and S. Ueda *Physical B&C Netherlands*, vol. 117&118, p. 926, 1983.

[57] B. Rech, T. Poschek, J. Müller, S. Wieder, and H. Wagner *Solar Energy Materials & Solar Cells*, vol. 66, p. 267, 2001.

[58] W. Schwarzenbach, A. A. Howling, M. F. ans S. Brunner, and C. Hollenstein *J. Vac. Sci. Technol. A*, vol. 14, p. 132, 1996.

[59] P. Torres, H. Keppner, J. Meier, U. Kroll, N. Beck, and A. Shah *Phys. Stat. Sol. A*, vol. 163, p. R9, 1997.

[60] H. Curtins, N. Wyrsch, and A. Shah *Electron Lett.*, vol. 23, p. 228, 1987.

[61] M. Heintze, R. Zeidlitz, and G. H. Bauer *J. Phys. D : Appl. Phys*, vol. 26, p. 1781, 1993.

[62] H. Keppner, U. Kroll, J. Meier, and A. Shah *Solid State Phenomena*, vol. 44-46, p. 97, 1995.

[63] T. Takahama, S. Okamoto, K. Ninomiya, M. Nishikumi, N. Nakamura, S. Tsuda, M. Ohnishi, S. Nakano, Y. Kishi, and Y. Kuwano *Technical Digest of the International PVSEC-5 Kyoto*, p. 375, 1990.

[64] H. Meiling, W. V. Sark, J. Bezermer, and W. V. der Weg *J. Appl. Phys.*, vol. 80, p. 3546, 1996.

[65] L. Sansonnens, J. Bondkowski, S. Mousel, J. Schmitt, and V. Cassagne *Thin Solid Films*, vol. 427, 2003.

[66] L. Sansonnens, A. Pletzer, D. Magni, A. A. Howling, C. Hollenstein, and J. Schmitt *Plasma Sources Sci. and Technol.*, vol. 6, p. 170, 1997.

[67] L. Sansonnens and J. Schmitt *Appl. Phys. Lett.*, vol. 82, 2003.

[68] M. A. Lieberman, J. P. Booth, P. Chabert, J. M. Rax, and M. M. Turner *Plasma Sources Sci. and Technol.*, vol. 11, p. 283, 2002.

[69] J. Schmitt, M. Elyaakoubi, and L. Sansonnens *Plasma Sources Sci. Technol.*, vol. 11, p. 206, 2002.

[70] K.-U. Riemann *J. Appl. Phys.*, vol. 65, p. 999, 1989.

[71] A. A. Howling, A. Belinger, P. Bulkin, L. Delaunay, M. Elyaakoubi, C. Hollenstein, J. Perrin, L. Sansonnens, J. Schmitt, and E. Turlot *15th Int. Symp. Pl. Chem.*, vol. I, p. 33, 2001.

[72] Y. P. Raizer, M. N. Shneider, and N. A. Yatsenko, *Radio-Frequency Capacitive Discharges*, p. 209. CRC Press, Inc, 1995.

[73] J. Ballutaud, C. Hollenstein, A. A. Howling, L. Sansonnens, H. Schmidt, and J. P. M. Schmitt *16th Int. Symp. Pl. Chem.*, vol. CD-ROM, 2003.

[74] J. Ballutaud, A. A. Howling, L. Sansonnens, C. Hollenstein, U. Kroll, I. Schönbächler, C. Bucher, J. Weichart, A. Buechel, and F. Jomard, "Plasma deposition of p-i-n devices using PECVD chamber : study of boron contamination," *Europhysics Conference Abstract, Montreux (Switzerland)*, vol. 26B, p. P2.029, 2002.

[75] P. Roca, S. Kumar, and B. Drévillon, "In situ study of thermal decomposition of B_2H_6 by combining spectroscopic ellipsometry and kelvin probe measurements," *J. Appl. Phys.*, vol. 66, p. 3286, 1989.

[76] U. Kroll, C. Bucher, S. Benagli, I. Schönbächler, J. Meier, A. Shah, J. Ballutaud, A. A. Howling, C. Hollenstein, A. Büchel, and M. Poppeller *to be published in Thin Solid Films*, 2003.

[77] A. Lloret, Z. Wu, M. Thye, I. E. Zawawi, J. Sifert, and B. Equer, "Hydrogenated amorphous silicon p-doping with diborane, trimethylboron and trimethylgallium," *Appl. Phys. A*, vol. 55, p. 573, 1992.

[78] M. Kubon, N. Schultz, M. Kolter, C. Beneking, and H. Wagner *Proc.12th European Photovoltaic Solar Energy Conference Amsterdam (Netherlands)*, p. 1268, 1994.

[79] H.Stiebig, F. Siebke, W. Beyer, C. Beneking, B. Rech, and H. Wagner, "Interfaces in a-Si:H solar cell structures," *Solar Energy Materials and Solar Cells*, vol. 48, p. 351, 1997.

[80] S. Tsuda, T. Takahama, M. Isomura, H. Tarui, Y. Nakashima, Y. Hishikawa, N. Nakamura, T. Matsuoka, H. Nishiwaki, S. Nakano, M. Ohnishi, and Y. Kuwano *Jpn. J. Appl. Phys*, vol. 26, p. 33, January 1987.

[81] A. Itoh, Y. Ishikawa, and T. Kawabe *J. Vac. Sci. Technol. A*, vol. 6, p. 2421, 1988.

[82] D. Franz, M. Hollenstein, and C. Hollenstein *Thin Solid Films*, vol. 379, p. 37, 2000.

[83] D. Schriver, P. Atkins, and C. Langford, *Inorganic Chemistry*, ch. 11, p. 460. Oxford University Press, second ed., 1994.

[84] J. Ballutaud, C. Bucher, C. Hollenstein, A. A. Howling, U. Kroll, M. Poppeler, and J. Schmitt. PCT/CH03/00685.

Acknowledgments

I would like first to express my deepest gratitude to my supervisor Dr. Alan A. Howling and to Dr. Christoph Hollenstein for giving me the opportunity, the resources and the freedom to carry out my doctorate in the Laboratory of Industrial Plasmas. I thank them, as well as Drs. Laurent Sansonnens and Jean-Luc Dorier, for being always there to help me in my work, for their helpful advice and their patience. I thank also Prof. Tran for his trust in me and for having hired me at CRPP.
Lot of thanks also to all the members of the laboratory for their friendship and the good ambiance of the laboratory : Malko (my non-official Japanese "anime" dealer), Antoine, Alban, Hannes, Thierry Maire and Raffaello. A special thank to my sushi fellows, Edith and Thierry Delachaux.

This work would have not existed without the financial support of the Commission for Technology and Innovation (CTI). I am grateful to Dr. Perrin from Air Liquide, Drs. Buechel, Kroll and Poppeller from Unaxis Solar, Prof. Shah from the Institute of Microtechnology of Neuchâtel and Dr. Hollenstein for having initiated the project, for having followed it and having taken part in this project. I would like to thank them for the discussions we had, their advice and their support.
I would like to express my gratitude to Dr. Buechel, Dr. Perrin and Prof. Shah for giving me the privilege and the honour to be part of my thesis jury.
A big thankyou to all the technical services of the CRPP, the electricians, the mechanics and Pierre Etienne for their accessibility, their miracles and their friendship.
I thank M. François Jomard from the CNRS laboratory L.P.S.C. for the large number of SIMS analyses he did for me.

Last, but not least, infinite thanks to my family : my parents (and their invitation to the Train Bleu ;-), Mamica, all my aunts. I would like also to thank all my friends for their support and their great friendship particularly the Cobra^{TM} team and Cannelle who had the kindness to feed me when I was too lazy for cooking.
Kiss to Gilles for his support, his patience, his cooking and lots more.

Curriculum Vitae

I was born on December 2nd 1975 in Paris, France. I did my primary and secondary school in the Lycée Claude Monet in Paris where I obtained the Baccalauréat, scientific section, in 1993.

Then I attended during three years a high level class of mathematics, physics and chemistry at Lycée Saint-Louis, Paris, as a preparation for Grandes Ecoles examinations. In 1996, I passed the examination for the integration in Ecole Supérieure d'Electricité (Supélec).

From 1996 to 1999, I studied electronics, electrotechnics, signal treatment and the physic of electronic components. During the last year at Supélec, I followed an electronic course at the Université Pierre et Marie Curie Paris VI in Paris. In 1999, I obtained a Supélec Engineer diploma and a Masters thesis of electronics (Diplôme d'Etude Approfondies) from university.

Since November 1999, I work as an assistant in the Laboratory of Industrial Plasmas, CRPP (Centre de Recherche de Physique des Plasmas) group, at the Ecole Polytechnique Fédérale de Lausanne, where I carry out a doctorate since December 2000.